Powder-fed Laser Directed Energy Deposition of Near-*β* Titanium Alloy: A Comprehensive Analytical and Experimental Analysis

by

Mazyar Ansari

A thesis

presented to the University of Waterloo

in fulfillment of the

thesis requirement for the degree of

Doctor of Philosophy

in

Mechanical and Mechatronics Engineering

Waterloo, Ontario, Canada, 2021

Examining Committee Membership

The following served on the Examining Committee for this thesis. The decision of the Examining Committee is made by a majority vote.

External Examiner: Andrew Pinkerton, Ph.D.

                            Senior Lecturer, Lancaster University

Supervisor: Ehsan Toyserkani, Ph.D.

                            Professor, University of Waterloo

Internal Member: Amir Khajepour, Ph.D.

                            Professor, University of Waterloo

Internal Member: Adrian Gerlich, Ph.D.

                            Associate Professor, University of Waterloo

Internal/External Member: Eric Croiset, Ph.D.

                            Professor, University of Waterloo

Author's Declaration

This thesis consists of material all of which I authored or co-authored: see Statement of Contributions included in this thesis. This is a true copy of the thesis, including any required final revisions, as accepted by the examiners.

I understand that my thesis may be made electronically available to the public.

Statement of Contributions

I would like to acknowledge my co-authors who contributed to the research described in this thesis:

- Prof. Ehsan Toyserkani: Supervision of the research, providing the framework of the research, editing and reviewing the individual studies presented in all chapters, providing experimental facilities and funding.

- Dr. Yuze Huang: Providing support in MATLAB programming, modeling methodology, and editorial feedback in the individual studies presented in chapters 3 and 4.

- Mr. Alexander Martinez-Marchese: Providing support in MATLAB programming, modeling methodology, and editorial feedback in the individual studies presented in chapters 3, and 5.

- Mr. Mobin Khamooshi: Providing support in MATLAB programming and modeling methodology in the individual studies presented in chapters 4 and 6.

- Dr. Ali Keshavarzkermani: Providing support in EBSD analysis and editorial feedback in the individual study presented in chapter 5.

- Dr. Reza Esmaeilizadeh: Providing support in sample preparation of EBSD analysis and editorial feedback in the individual study presented in chapter 5.

Abstract

Laser directed energy deposition through powder feeding (LDED-PF), a class of metal additive manufacturing (AM), is a promising technique that enables the repair and refurbishment of metallic components with a variety of materials as well as the complete near-net-shape manufacturing of metallic parts with moderately complex geometries. The localized solidification and complex thermal cycles in LDED-PF have a significant effect on the deposition characteristics. The continuous change in the deposition rate occurs due to the thermal-based complexities and alters the deposition geometry and microstructure. There are still major knowledge gaps and challenges in achieving desirable dimensional and microstructural features of as-built components. A clear understanding of the process and its effects on the temperature field and the resulting dimensional and microstructural characteristics are of tremendous importance. Developing methodologies to predict the thermal-based complexities during the multi-track deposition and minimize the adverse effects is essential to enhancing LDED-PF. This thesis aims to develop a time-efficient predictive physics-based model that improves dimensional accuracy and process stability. The model also provides an effective tool for process optimization and microstructural engineering through process-microstructure linkages.

To this end, this research first tries to analytically couple the moving laser beam, powder stream, and semi-infinite substrate. A process map is developed for the single-track deposition, which draws the physical barriers to a stable process. To develop an effective heat source model that is more in harmony with the physics of the process, analytical solutions to three heat source models are introduced and compared to describe the transient temperature field in the single-track deposition. To improve the model fidelity, the enhanced thermal diffusivity and heat source radius are calibrated in terms of linear functions. To include the effect of scanning strategies in multi-track LDED-PF, the model is adapted for multi-track deposition of different scanning strategies. The temperature fields of cuboid-geometry depositions are simulated under four scanning strategies, namely, bidirectional, unidirectional, inward spiral, and S-pattern. The effect of heat accumulation is considered, and 2D thermal models are time-efficiently computed to obtain the melt pool shape. A new universal algorithm, based on parabolic functions, is developed to predict the geometrical profile of the overlapping beads, which applies to all scanning strategies. The model obtains the local heat flow direction at the longitudinal center-plane of each track. The solidification parameters of thermal gradient and solidification rate are then extracted from the local heat flow to reveal the linkages between the process and solidification microstructure.

The solidification maps are established, and the microstructural transition of columnar-to-equiaxed is predicted. The developed model is validated for multi-track deposition of Ti-5Al-5V-5Mo-3Cr alloy at different laser powers, scanning speeds, and step-over distances under different scanning strategies. The developed knowledge of solidification characteristics and microstructural evolution can greatly contribute to the development of the Ti-5Al-5V-5Mo-3Cr alloy processed by LDED-PF.

Lastly, an adaptive prediction protocol is developed based on physics-based mathematical modeling to control the temperature and deposition dimensions. A simulation-based algorithm is designed for multi-track deposition of direction-parallel scanning strategies. The algorithm simulates the transient temperature field and geometry of subsequent tracks to adaptively predict the required laser power as the main processing parameter, such that each track arrives at the desired dimensions. The performance of the developed adaptive modeling is experimentally evaluated and validated. The adaptive protocol of modeling, as a cost-effective approach, only requires the thermophysical properties of the material and some basic information of the LDED-PF setup to successfully improve the dimensional accuracy and flatness of the deposited layers by neutralizing the adverse effect of heat accumulation and overlapping beads. This unique adaptive protocol can also ensure the uniformity of the deposition and the stability of the process by maintaining the standoff-distance constancy.

Acknowledgments

I would like to express my sincere gratitude to my supervisor, Prof. Ehsan Toyserkani for his support, patience and guidance through the years of my Ph.D. study.

I am much obliged for the comments and suggestions of the committee members, Prof. Andrew Pinkerton, Prof. Amir Khajepour, Prof. Adrian Gerlich, and Prof. Eric Croiset.

I would like to acknowledge the encouragement and support from my friends and colleagues at the University of Waterloo, especially Dr. Shahriar Imani Shahabad, and Dr. Osezua Ibhadode, Dr. Zhidong (Brian) Zhang, Dr. Ehsan Marzbanrad, and Dr. Hamed Asgari.

Finally and most importantly, I would like to thank my family members and my parents for their support and encouragement in the past years.

Table of Contents

List of Figures

List of Tables

Chapter 1: Introduction

1.1 Overview and Research Motivations

Although metal additive manufacturing (AM) by laser directed energy deposition through powder feeding (LDED-PF) has been explored for manufacturing metallic parts, the integrity of fabricated parts in terms of dimensional accuracy, microstructure, and mechanical properties are quite unsteady and they are very dependent on processing parameters. To provide a practical framework of printing with LDED-PF and to maximize the process performance, a key and cost-effective solution is modeling. A model is needed to provide the rapid and precise process prediction required for designing/optimization of the adaptive tool-path. The complex heat transfer and transport phenomena make it difficult to understand the effect of processing parameters on the overall process. A process model is required to consider major physical phenomena during the process, taking into consideration the transient temperature field, heating/cooling cycles, and solidification characteristics. In return, these provide important information about solidification microstructure and resulting mechanical properties.

On the other hand, the use of Ti-5Al-5V-5Mo-3Cr alloy in aerospace applications has been increasing in the past decade. Not only is there little research on AM of Ti-5Al-5V-5Mo-3Cr alloy, but also even fewer works on LDED-PF of this alloy. The understanding of the effects of processing parameters on deposition geometry, and microstructure is imperative for the further development of Ti-5Al-5V-5Mo-3Cr alloy by LDED-PF.

1.2 Challenges and Solutions

In the LDED-PF process modeling, the first challenge is to incorporate the interaction between heat and mass flux into the model. The melt pool dimensions are influenced by the interaction. The single-track deposition is the first step of the process when the key processing parameters for multi-track deposition are defined based on them. Hence, they should be defined appropriately; otherwise, the multi-track deposition would be problematic and defects may be induced by inappropriate processing parameters. Moreover, parameter selection for LDED-PF is still challenging for new material/equipment systems, and defining them usually needs time-consuming and costly preliminary screening phase experiments. To this end, analytical modeling can be a great assistance for process mapping and parameter selection such that the processing parameters can be predicted with good

accuracy. The time and cost of the preliminary screening phase experiments can be saved as the analytical model can be updated according to the material/equipment.

The second challenge of the LDED-PF process is the effect of overlapping beads and heat accumulation during multi-track deposition. Considering the nature of the process for applying overlapping tracks consecutively, the heat from the previous track affects the ones in the vicinity. The deposition rate keeps changing based on the scanning strategy, defects can happen more, and the build-up process may be sacrificed by a non-uniform deposition profile. Physics-based modeling can help to correlate the processing parameters with the geometrical profile of multi-track depositions. The temporal history of temperature for all tracks can be analytically integrated into the model to account for the effect of heat accumulation. It can also be used for the development of closed-loop and intermittent controllers. Moreover, the determination of solidification behavior during LDED-PF is challenging, although it directly influences final microstructures and resultant mechanical properties. A physics-based model can predict solidification characteristics and help to understand the solidification dynamic behavior.

1.3 Objectives and Scope of Study

This research first tries to take a problem-solving approach to overcome the above-mentioned challenges by developing a physics-based model, which takes into consideration the major interactions and physics of the process. The main objective is to have better control/prediction of the LDED-PF process. To achieve this goal, the following core objectives are pursued. The interconnections of core objectives are set out in Figure 1-1.

- ➢ Develop a process map for parameter selection in the single-track deposition.

- ➢ Introduce different heat source models and compare their performance.

- ➢ Calibrate the heat source model for improved model fidelity.

- ➢ Develop a time-efficient physics-based model for LDED-PF.

- ➢ Expand the physics-based model for multi-track deposition.

- ➢ Develop a universal algorithm for the rapid prediction of deposition geometry.

- ➢ Use the physics-based model to predict the thermal cycles and solidification parameters.

➢ Correlate the process with the microstructure using the solidification parameters.

➢ Predict and study the microstructure morphology/size.

➢ Develop an adaptive modeling protocol for multi-track LDED-PF.

➢ Thermal and dimensional control of the deposition by predicting the laser power.
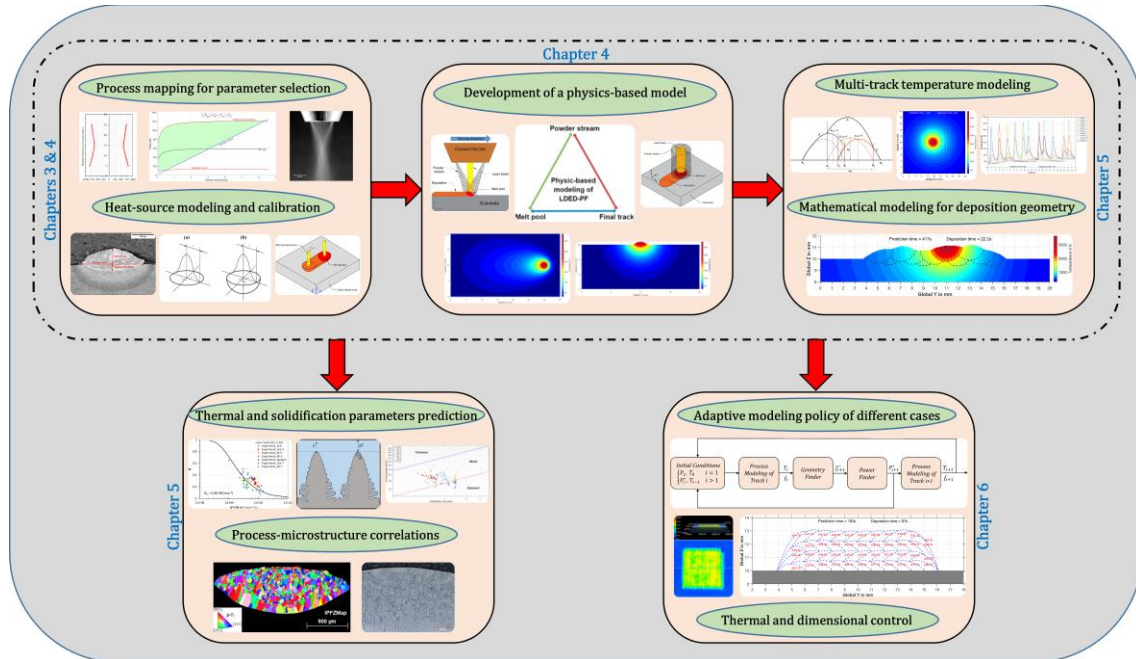
Figure 1-1. Thesis graphical abstract, setting out core objectives and their interconnections.

1.4 Organization of Thesis

The thesis includes seven chapters which are organized as follows. Chapter 1 presents the overview, research motivations, challenges, and objectives of the research. Chapter 2 presents a general literature review and background of metal AM and LDED-PF followed by the introduction of physics-based modeling and its importance in the enhancement of LDED-PF. Chapter 3 presents an analytical module for the coupling powder stream and laser beam in the LDED-PF process and provides a time-efficient model for process mapping and definition of the processing parameters for single-track deposition. Chapter 4 presents analytical solutions for the rapid prediction of transient temperature fields in LDED-PF based on three different heat source models. Chapter 5 presents a physics-based model of multi-track LDED-PF under four different scanning strategies: bidirectional, unidirectional, inward spiral,

and S-pattern. A new universal algorithm, based on parabolic functions, is developed to predict the geometrical profile of the overlapping beads. The solidification parameters of thermal gradient and solidification rate are extracted from the local heat flow to reveal the linkages between the process and solidification microstructure. Chapter 6 presents adaptive physics-based modeling for thermal and dimensional control. A simulation-based algorithm is designed to adaptively predict the required laser power, as the main processing parameter, such that a uniform deposition profile is achieved. Chapter 7 presents the major conclusions of the research. Based on the conclusions, possible future work is briefly introduced.

Chapters are adapted from the published or to-be-submitted works as following:

Chapter 3:

M. Ansari, A. Martinez-Marchese, Y. Huang, E. Toyserkani, A mathematical model of laser directed energy deposition for process mapping and geometry prediction of Ti-5553 single-tracks, Materialia. 12 (2020) 100710. doi:10.1016/j.mtla.2020.100710.

Chapter 4:

M. Ansari, M. Khamooshi, Y. Huang, E. Toyserkani, Analytical solutions for rapid prediction of transient temperature field in powder-fed laser directed energy deposition based on different heat source models, Appl. Phys. A. 127 (2021) 445. doi:10.1007/s00339-021-04591-w.

Chapter 5:

M. Ansari, A. Martinez-Marchese, M. Khamooshi, A. Keshavarzkermani, R. Esmaeilizadeh, E. Toyserkani, A comprehensive physics-based model for multi-track powder-fed laser directed energy deposition under different scanning strategies: On the correlation of process, deposition dimensions, and solidification microstructure in additively manufactured near-β titanium alloy (Ready for submission).

Chapter 6:

M. Ansari, A. Martinez-Marchese, M. Khamooshi, E. Toyserkani, Adaptive physics-based modeling for powder-fed directed energy deposition (Being ready for submission).

Similar versions of these works have been modified to fit the content of this thesis. The corresponding license agreements are provided in the section of Letter of Copyright Permission.

Chapter 2: Background and Literature Review

In this chapter, a general background of the LDED-PF process and physics-based modeling is reviewed. The chapter begins with an introduction of metal AM followed by an overview of modeling efforts and their importance in the enhancement of LDED-PF.

2.1 Metal Additive Manufacturing

Metal additive manufacturing (AM) processes build three-dimensional (3D) parts by progressively adding layers of metallic materials guided by a digital model. This unique feature allows the production of complex or customized metallic parts directly from the design with minimum need for expensive tooling. In addition, a significant reduction in the part count can be realized by eliminating or reducing the need to assemble multiple components. Furthermore, parts can be produced on-demand, reducing the inventory of spares and decreasing lead time for critical or obsolete replacement components. For these reasons, metal AM is now widely accepted as a new paradigm shift for the design and production of high-performance metallic components for aerospace, medical, energy, and automotive applications. Significant advances over the past twenty years in the constituent technologies of metal AM, including lower cost reliable industrial lasers, inexpensive high-performance computing hardware, and software, and metal powder feedstock technology have enabled it to become a state-of-the-art processing method. It has now reached a critical acceptance level, as evidenced by the rapid growth in sales of commercial systems. However, there are still challenges that need to be addressed and a thorough understanding of material-process-structure-property-performance is desirable to fully unleash the potential of metal AM in producing defect-free, structurally sound, and reliable parts [1].

2.1.1 Metal AM Processes

The metal AM processes consolidate feedstock materials such as powder, wire into a dense metallic part by melting and solidification with the aid of an energy source such as laser, electron beam, or electric arc in a layer-by-layer manner. Two major and mature metal AM processes are defined by ASTM standard F2792 [2] as Powder Bed Fusion (PBF) and Directed Energy Deposition (DED). PBF begins with a solid or surface CAD model, orienting it within a build volume to include support structures, slicing into planar layers, defining a scan path, and build-file based upon a pre-specified set

of material-specific parameters and the specific machine configuration. The part forms by fusing thin layers of powder pass-by-pass and layer-by-layer [3].

As defined by ASTM F2792-12a [2], DED is categorized as one of the metal AM processes in which a focused heat source is used to directly deposit materials as they are being fed into the heat source. A further classification is provided as a function of the heat source (laser beam, electron beam, plasma, and electric arc), feedstock material (powder and wire), and feeding methods (off-axial and coaxial). Although there are various types of DED systems, this research focuses on the laser-aided powder-based DED, which is the most commonly used DED technology. Here, we use the nomenclature for laser (L), and powder-fed (PF). The schema is shown in Figure 2-1.
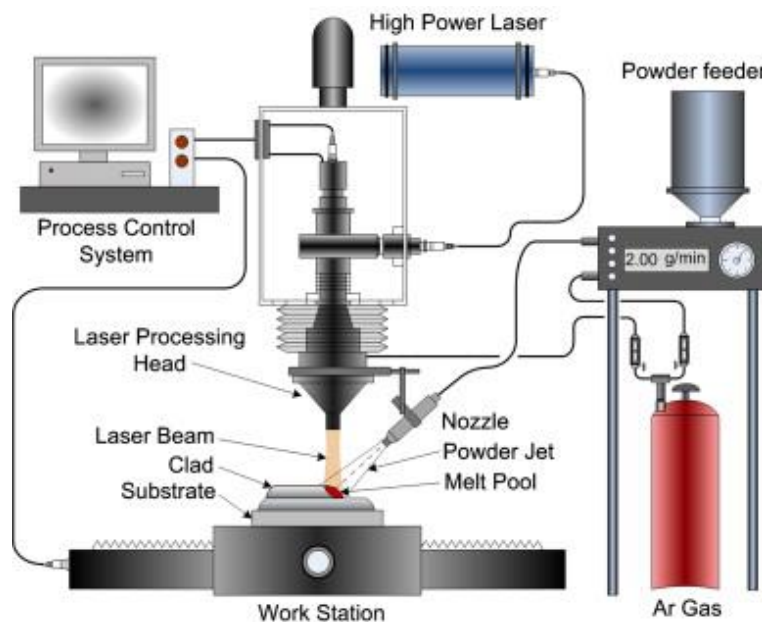
Figure 2-1. Schematic representation of a lateral LDED-PF system (Reproduced with permission from Ref. [4]).

Both metal AM processes of PBF and DED have their advantages/disadvantages which are summarized in Table 2-1 based on the benchmark study by OPTOMEC [5]. The study was to determine the relative print speed and price to build a mid-size metal part with simple geometry. The study results show that DED is more than 10 times faster and five times less expensive than PBF for this benchmark study part. While PBF technologies are suitable for smaller, complex geometries, with hollow unsupported passages/structures, DED is better suited for larger parts with coarser features requiring higher deposition rates. Usage of thinner layer thickness, finer powder, and smaller beam energy source

6

size leads to a superior surface finish on the as-built parts from the PBF process as compared to the DED process. On the other hand, the powder-fed DED process is ideally favorable for manufacturing multi-material structures and functionally graded materials due to the ease of introducing different powders into the melt pool, while it isn't easy to use different powders in the PBF process [6]. The ability of the DED technology to add metal on existing parts allows it to apply surface protective coatings, remanufacture and repair damaged parts and reconfigure or add features to existing parts, besides building new parts. Some examples are shown in Figure 2-2.

Table 2-1. Feature comparison of two main metal AM processes (Courtesy of OPTOMEC [5])

Feature	DED	PBF
Part complexity/resolution	Relatively simple geometry with less resolution (R_a 20-50 µm)	Complex geometry with high resolution (R_a 6-12 µm)
Part size	Unlimited	Limited
Dimensional tolerance	+/-1 mm	Less than 0.1 mm
Average layer thickness	500 µm	30 µm @ 400 W
Powder cost	Ti-64 ~ $160/kg IN-718 ~ $80/kg SS316L ~ $30/kg	Ti-64 ~ $600/kg IN718 ~ $200/kg SS316L ~ $100/kg
Repair/coat & add features	Capable – add material onto 3D surfaces	Limited – requires horizontal build plane
Multi-material	Programmatically grade or blend	Limited
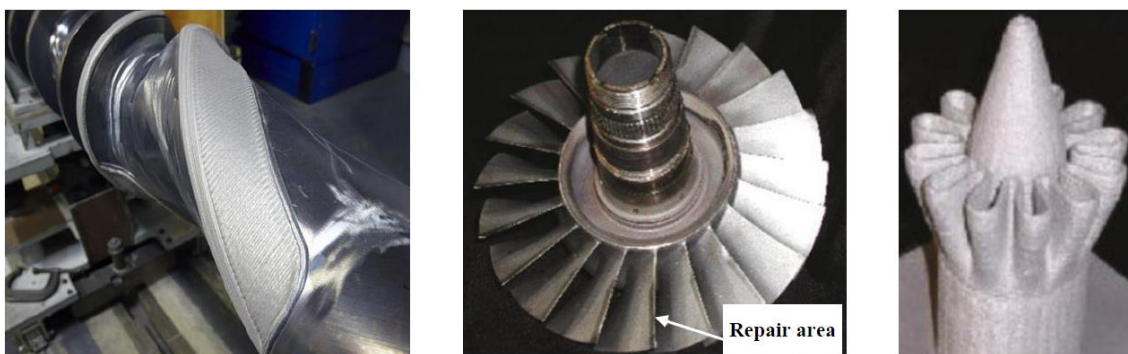
Figure 2-2. Examples of using DED technology for (a) coating, (b) blisk repair, (c) manufacturing nozzle for gas turbine exhaust (Courtesy of OPTOMEC [7]).

2.2 Overview of Modeling Efforts in LDED-PF

In LDED-PF, the laser-powder interaction happens within the attenuation distance. The laser beam is attenuated by directly injected powder particles and interacts with the underlying layer or substrate to form a melt pool. Meanwhile, the heated powder particles reach the melt pool and become a part of the melt pool. Figure 2-3 shows the schematic of the laser-powder-substrate interaction in the LDED-PF process. The melt pool experiences rapid solidification while solidifying from liquid to form a track. Several physical phenomena contribute to the thermal characteristics, and deposition geometry. The melt pool experiences rapid heating/cooling cycles and high-temperature gradients, which cause thermal-based complexities. Therefore, high-fidelity and time-efficient tools for measuring/predicting the temperature field and thermal history during LDED-PF are of vital importance.
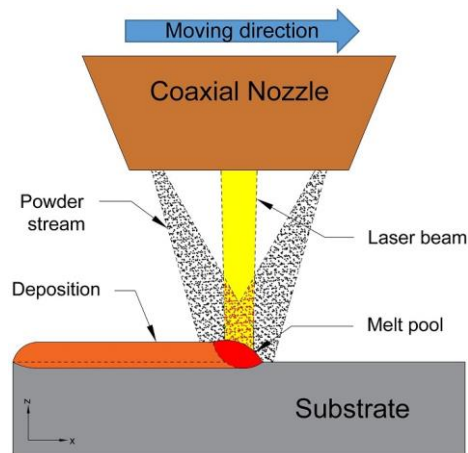
Figure 2-3. Scheme for LDED-PF along longitudinal cross-section, showing the interaction of powder, laser beam, and substrate.

A clear understanding of laser-material interaction and thermal characteristics is required for further development and full industrial adaption of the LDED-PF process. However, the complex multi-physics nature of the LDED-PF process makes the understanding of the underlying physical aspects difficult [8]. The single-track deposition process, as the first step of the process, should be optimized, and controlled for a stable deposition since an unstable deposition can undermine the quality and dimensional accuracy of the multi-track deposition process. Choosing optimum processing parameters would be challenging due to machine dependencies of many parameters such as the laser beam quality, powder stream profile, and velocity of particles. The first step is to predict the processing parameters,

the resultant deposit's dimensions, and thermal history based on the basic aspects of the laser beam, powder stream, and thermophysical properties of the materials. Several attempts have been made toward process modeling and optimization of the LDED-PF process, and to this end, different predictive tools have been used, including experimental approaches and physics-based models. Different process models have been built to simulate melt pool characteristics, including physics-based, and empirical/statistical models. Empirical/statistical models, which are developed based on the experimental data, have been extensively used for the optimization of single-track LDED-PF, in general [9–15]. However, the empirical/statistical approach is mainly equipment/material specific and it only considers a few variables as laser power, beam diameter, moving velocity, and powder feed rate. Each LDED-PF equipment has a different design for the nozzle, powder profile, and laser beam and consequently, major physical phenomena would be affected by them.

2.2.1 Physics-based Models

Physics-based modeling, including numerical and analytical modeling, is another approach in this context. Physics-based models introduce intermediate variables from one stage of the process to the other. The complete deposition process can be broken down into several physical stages and each physical stage can have different variables [16]. The thermal history can be simulated, melt pool forms as a result of the powder-laser-substrate interaction, and the thermal characteristics define the final track properties. Figure 2-4 illustrates the physical stages and intermediate variables in LDED-PF.
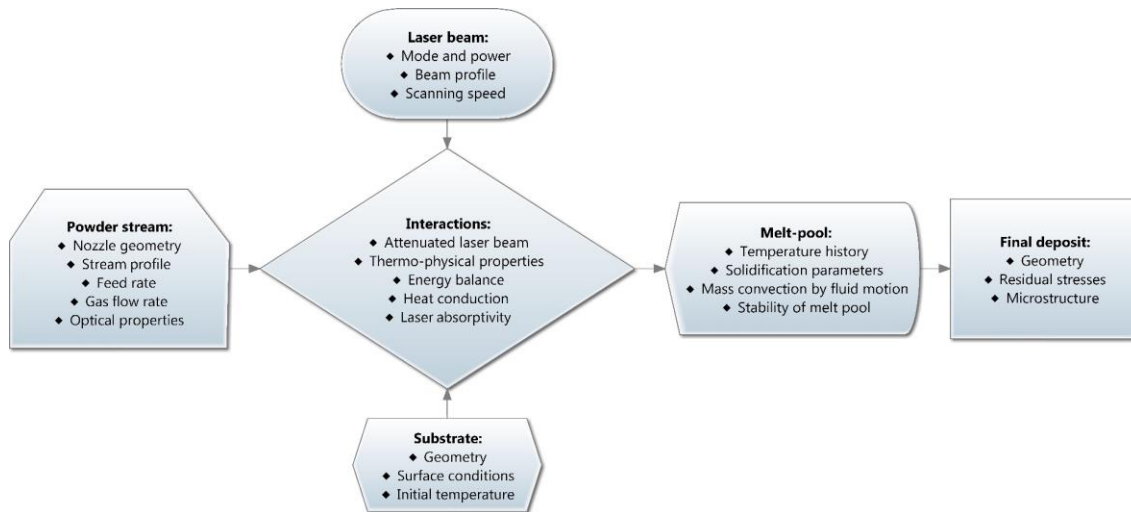
Figure 2-4. Physical stages and corresponding process variables in LDED-PF (Redrawn from Ref. [16]).

An effective temperature simulation needs certain assumptions. A quantitative description of the heat source energy distribution is needed. Various heat source models have been mathematically described in the literature, which are broadly classified as point (1D), surface (2D), and volumetric (3D) sources. Eight different heat source models (shown in Figure 2-5) were discussed and compared for the simulation of the PBF process by Zhang et al. [17]. Each heat source model can have its advantages and disadvantages. The consideration of different heat source geometry can be specific to the individual processes/material. Although the eight heat source models by Zhang et al. [17] are adopted for the PBF process, some of them can be used for the LDED-PF process. Some research studies [18] used a point heat source model to solve the heat conduction equation and simulate the temperature field. A point heat source simplifies the complexity of energy distribution. For a heat source like a laser beam, the power intensity has a radial variation, which can be quantitated as a 2D Gaussian distribution. This surface-distributed energy can be considered for LDED-PF [19]. The assumption of 3D heat sources such as semi-spherical and semi-double elliptical has been taken into consideration, mostly in welding literature, as a virtual proxy to mimic the laser-material interaction behavior [20]. Some research studies considered these volumetric heat sources in their simulation for the LDED-PF process [21]. These mathematical descriptions of heat sources are usually used to reduce the computational time in numerical models. However, these assumptions may not be perfectly in line with the underlying physics of the process.
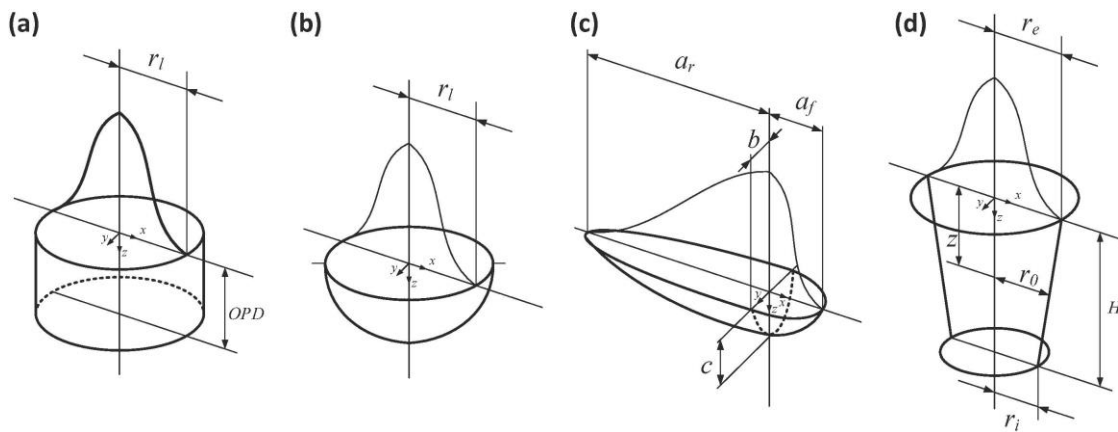
Figure 2-5. Schema for heat source models, (a) cylindrical shape; (b) semi-spherical shape; (c) semi-ellipsoidal shape; (d) conical shape (Reproduced with permission from Ref. [17]).

Numerical modeling has been verified as an accurate simulator for different aspects of the LDED-PF process such as powder flux distribution [22,23], laser-powder interaction [24], geometrical features of the deposit [25–28], temperature, fluid velocity fields [29,30]. Major advances in the modeling of LDED-PF are reviewed by Pinkerton [16] and the features, strengths, and weaknesses of predictive modeling are discussed. Haley et al. [31] investigated the effect of standoff (working) distance through a physics-based model and experimental observations. The results of their study are shown in Figure 2-6, emphasizing the importance of standoff distance constancy. In LDED-PF, the constancy of standoff distance is an important factor. The standoff distance is the distance between the tip of the deposition nozzle and the substrate/underlying layer. The laser beam/powder stream profile has a spatially different energy/particle distribution in different distance from the nozzle tip. The change of the standoff distance can make the process instable or change the mass capture efficiency, hence the standoff distance must be kept constant during the build-up process to maintain the process stability.
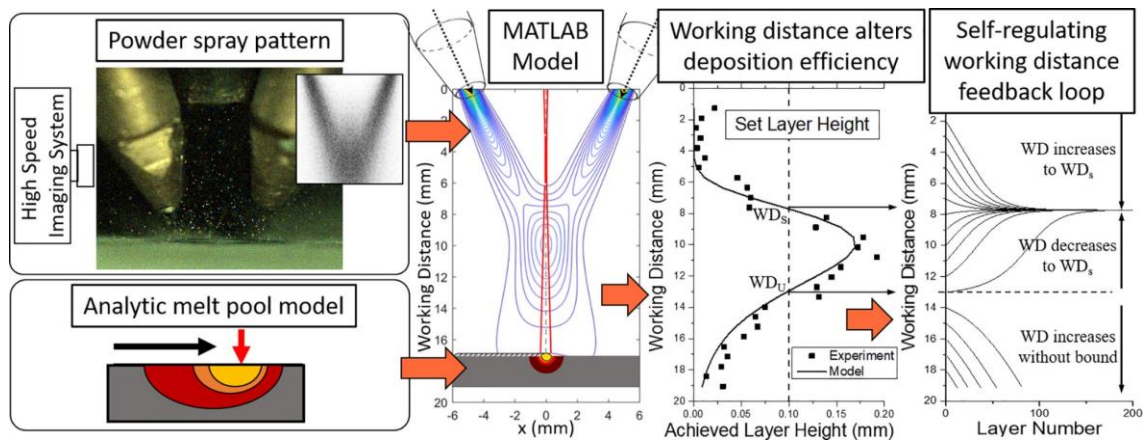
Figure 2-6. Demonstration of the effect of standoff distance on the process efficiency (Reproduced with permission from Ref. [31]).

In the most recent published works, Bayat et al. [32] and Wei et al. [33] developed multi-physics numerical models to simulate temperature, fluid dynamics, and geometry of the tracks in single-track and multi-track LDED-PF. Figure 2-7 shows the results of some of their simulations. Different physical phenomena were considered and the experimental validation tests showed the high accuracy of the predictions.
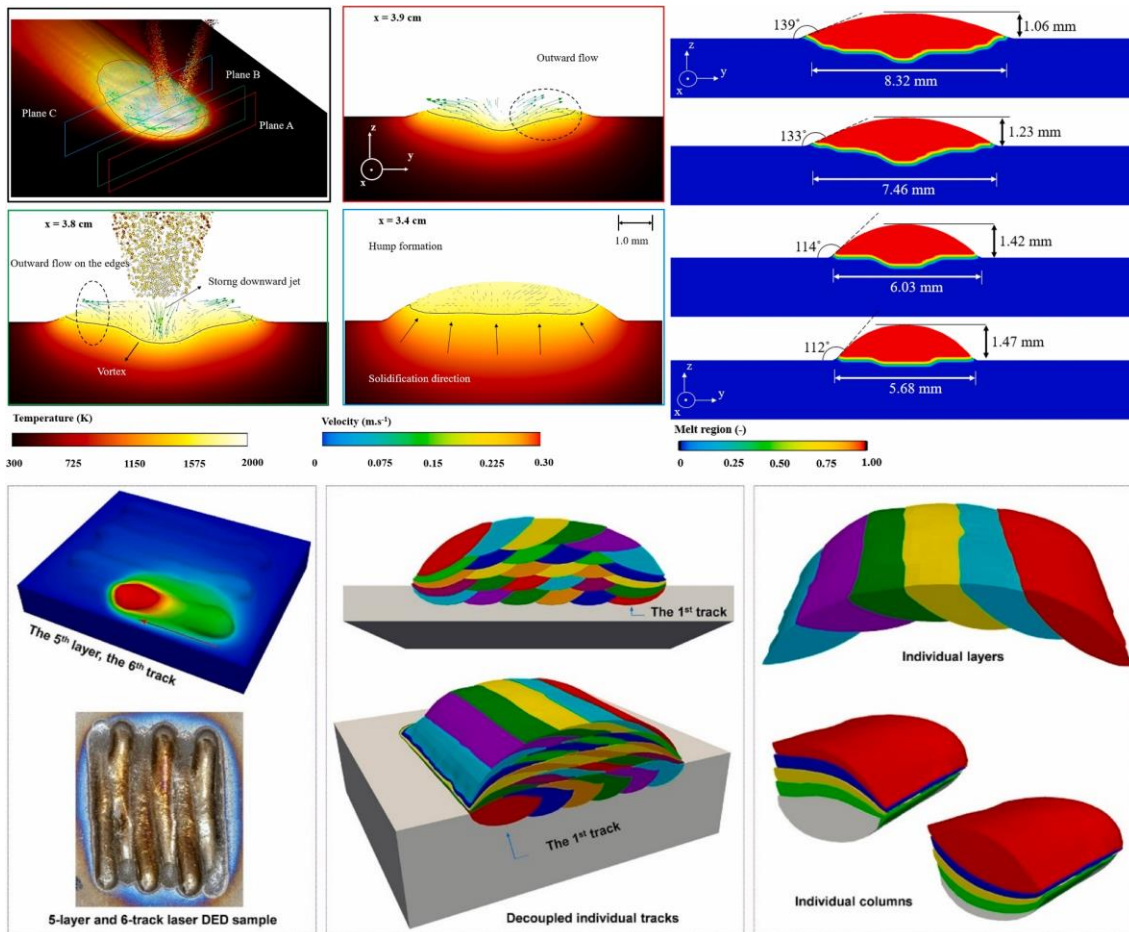
Figure 2-7. Examples of numerical simulations in LDED-PF (Reproduced with permission from Refs. [32,33]).

Although numerical modeling has proven as an accurate tool for the description of the temperature field, the accuracy is mainly governed by the discretization and meshing techniques, which significantly adds to the computational time and complexity of the model. In contrast, analytical modeling, as a classic approach, offers a time-efficient tool for process modeling and understanding the physical aspects of the process. Although the accuracy of the analytical prediction models is generally lower than numerical models, their predictions seem adequate for LDED-PF, considering the printing resolution and large melt pool size in LDED-PF. Picasso et al. [34] developed a fundamental analytical model for off-axial LDED-PF to predict the laser moving velocity and powder feed rate for a given set of parameters such as laser power, beam width, and powder stream geometry. Frenk et al. [35] proposed a quantitative analytical model for off-axial LDED-PF based on the energy balance and overall mass

to estimate the dimensions of the melt pool and deposit, as well as the catchment efficiency and global absorptivity. Lalas et al. [36] took an analytical approach for the off-axial LDED-PF process to estimate the deposit dimensions based on surface tension and taking into account the laser moving velocity and powder feed rate. Pinkerton et al. [37] integrated the powder stream and substrate thermal conduction and mass flow into an analytical model for coaxial LDED-PF. Zhu et al. [21] established an alternative analytical model to estimate the geometric characteristics of the deposit based on the curve equation of the deposit, which takes into account the laser powder, laser-powder interaction. In the latest published study by Huang et al. [18], an analytical model was developed for the LDED-PF process. The study tried to couple the heat flux and mass flow by considering the associated spatial distribution. Furthermore, the analytical models can be a perfect fit for process mapping and parameter selection as they do not need a high accuracy prediction. There are a limited number of studies concerning an analytical approach for process mapping of the LDED-PF process. As a preliminary model constructed on the basis of the attenuation of the laser beam by powder cloud, Jouvard et al. [38] adopted a very simple approach, taking into consideration Beer-Lambert law for the laser beam attenuation and a one-dimensional solution of the heat conduction, to define two thresholds for substrate and powder fusion. de Oliveira et al. [39] used the same approach to plot a brief process map showing the laser power required to melt the substrate and powder.

Varieties of these analytical models are reported in the literature; however, most of them are limited to single-track modeling in which major complexities of the LDED-PF process such as the effects of heat accumulation and scanning strategy are ignored. There are few works on the analytical modeling of multi-track deposition. Li et al. [40,41] presented an analytical computation of temperature field in thin-walled samples. A transient solution to a point heat source in a semi-infinite body is used together with a pair of positive and negative heat inputs to compute the temperature field including the effect of heat accumulation. Huang et al. [19] developed a physics-based model of LDED-PF by analytically coupling the laser heat flux powder and powder mass flow, in which both are expressed as a surface heat source. Their model is only adopted for multi-track deposition under the bidirectional strategy.

13

2.2.2 Process-microstructure Correlation in LDED-PF

The localized solidification and complex thermal cycles in LDED-PF have a major effect on the microstructure and related properties [42]. Currently, there is significant academic and industry interest in controlling the location-specific microstructure and properties of LDED-PF manufactured components through mechanistic modeling. In this context, physics-based models of temperature prediction are essential to calculate the parameters needed for the mechanistic models. Figure 2-8 shows the important role of temperature prediction models in the overall understanding of the physical processes in AM. Experimental characterization without considering the attendant thermal complexities cannot reveal the origins of the location-specific variations. However, characterization studies supported by physics-based modeling not only reveal the location-specific variations of microstructure/properties but also justify the reason for the variations [43]. The variations can be related to the evolution of the temperature field in the spatial-temporal domain.
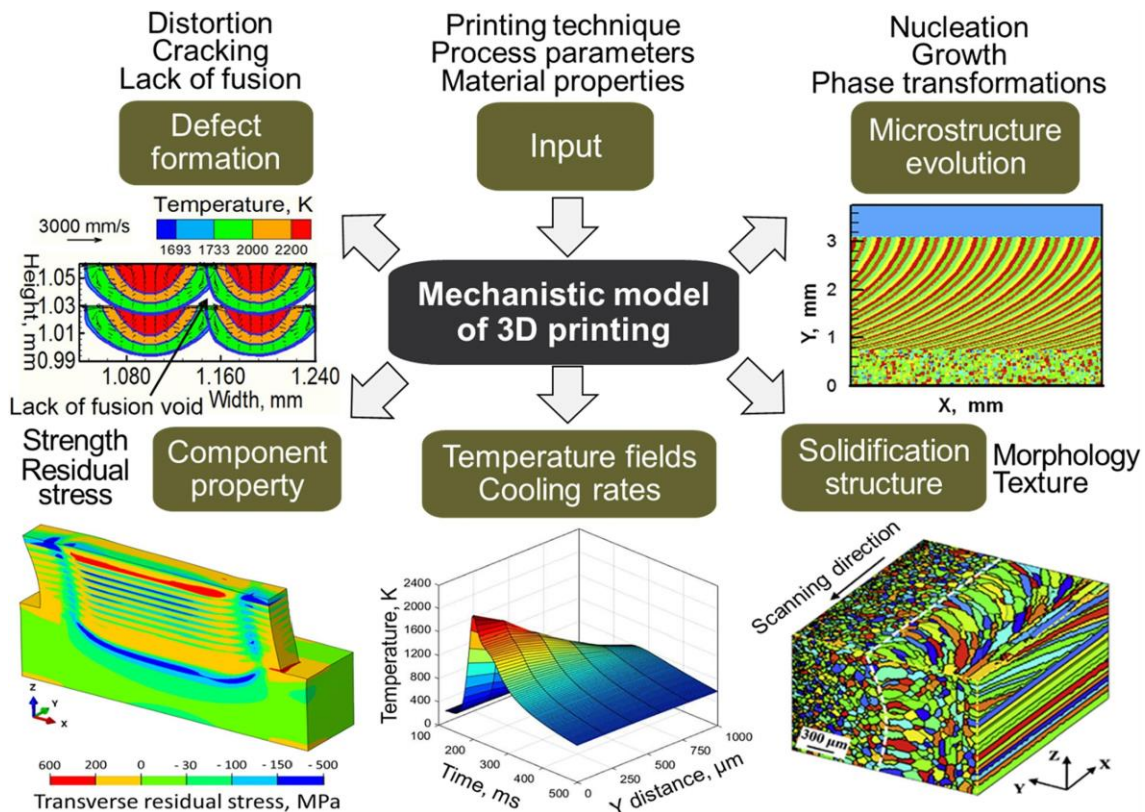
Figure 2-8. Schema of a mechanistic model in metal AM, showing the importance of physics-based modeling in understanding process-structure-property (Reproduced with permission from Ref. [44]).

14

Prediction of solidification microstructures requires the modeling of the nucleation and growth of all possible phases. In a more general approach, both nucleation and growth have to be simultaneously considered as is necessary for the columnar to equiaxed transition (CET). During solidification of the melt pool, the solid acts as a heat sink, and solidification is locally directional. The heat flux is opposite to the growth direction and the rate of advance of the isotherms constrains the solid-liquid interface to grow at an imposed velocity. If the depositing material is similar to the substrate, initial solidification shows an epitaxial growth when the substrate is slightly molten. If nucleation and growth of equiaxed grains in the liquid ahead of the columnar front are avoided, an epitaxial, columnar structure is achieved. The CET occurs when nucleation of sufficiently numerous equiaxed grains takes place in the constitutionally undercooled liquid adjacent to the columnar dendritic front. Once nucleated, a certain volume fraction of equiaxed grains forms, depending on the thermal gradient in the liquid on the solidification rate of the columnar front on the nuclei density of the alloy. This eventually leads to the CET. Therefore, close control of the CET is essential for successful microstructural engineering [45].

To understand the microstructural variations based on the temperature field, one strategy is the use of solidification parameters, namely the thermal gradient (G) and solidification rate (R) [46]. The linkage may be derived from classic theories of solidification. As presented in Figure 2-9, the solidification map can be constructed by G and R, where the G/R ratio governs the solidification mode and CET while their product (GR) controls the scale of the solidification microstructure. The solidification mode transforms from planar → cellular → columnar dendritic → equiaxed dendritic as the G/R ratio decreases. In addition, a higher value of GR induces a finer substructure and a lower value of GR induces a coarser substructure [47]. The solidification parameters depend to a large extent on the processing parameters. The real-time experimental measurement/monitoring can be performed to control the solidification parameters and resultant microstructural features. Different experimental setups can be used to monitor the process and measure the thermal characteristics, such as thermocouples, thermal imagers, infrared (IR) cameras, and pyrometers [48,49]. Akbari and Kovacevic [50] employed real-time melt pool monitoring to control the microstructure scale of thin-walled samples by maintaining the melt pool size. Farshidianfar et al. [51,52] implemented a closed-loop control system for real-time controlling of the microstructure scale in single-track and thin-walled samples. Lia et al. [53] employed embedded thermocouples for real-time temperature measurements during LDED-PF to enable the identification of solidification substructure mode/size based on critical

processing parameters and the corresponding G and R values. Their results concluded that the processing parameters are related to the solidification parameters that dictate the final microstructure.
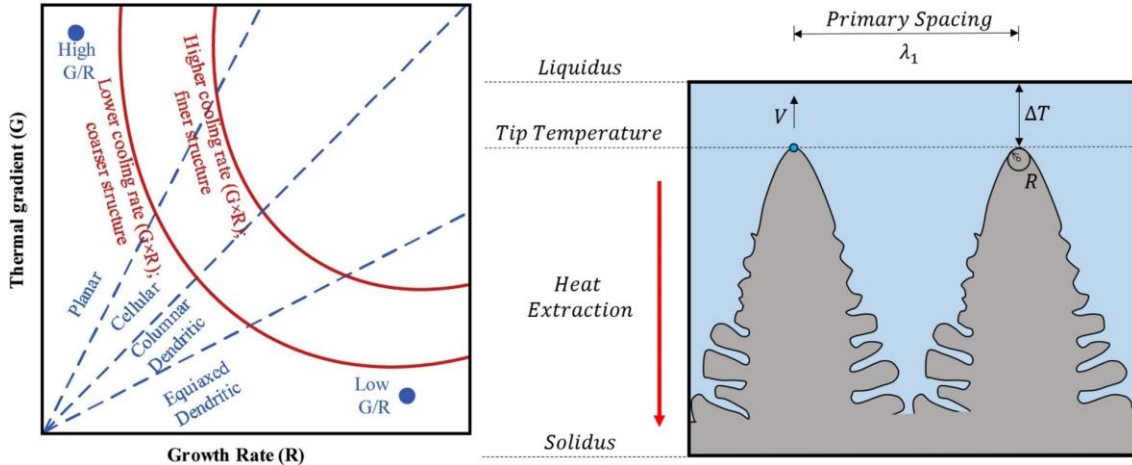
Figure 2-9. Schema of the effect of G and R on the solidification mode and scale according to the related theories (Reproduced with permission from Refs. [54,55])**.**

Despite all advantages associated with in-situ monitoring technologies, they have some shortcomings and a reliable temperature measurement remains challenging. For example, thermocouples can only measure interior temperature profiles in the substrate rather than the melt pool. In addition, the conversion of IR intensities into temperatures is still challenging because of the interference of plasma plume and the temperature-dependent emissivity. Lastly, IR cameras and pyrometers can only obtain surface temperatures rather than interior temperatures [43]. It should be noted that different in-situ monitoring devices can be integrated in order to compensate for the technical shortcomings of each other. However, this approach is mainly costly. Physics-based analytical/numerical modeling, on the other hand, is a promising alternative to the experimental measurement of the temperature field, melt pool shape/size, and solidification parameters. Knapp et al. [56] developed a digital twin of LDED-PF which utilizes a 3D numerical model. Their predicted thermal and microstructural results were shown to be accurate. Sun et al. [57] built a numerical model based on the mass/heat transfer in LDED-PF. The volume of fluid and enthalpy-porosity methods were employed for more accurate prediction. The single-track geometry was well-predicted and solidification parameters were extracted.

2.3 LDED-PF of Ti-5553 Alloy

Having introduced the concept of metal AM and LDED-PF, this section briefly reviews metal AM of near-β titanium (Ti-5Al-5Mo-5V-3Cr) alloy. Ti-5Al-5Mo-5V-3Cr (Ti-5553), initially developed based on a Russian alloy system termed VT22 to substitute Ti-1023 and steel components, has an excellent combination of high strength and good ductility at room temperature, and strong aging response [58]. Ti-5553 has applications in the field of aerospace, such as landing gear components [59]. For example, the Boeing 787 utilizes Ti-5553 to fabricate the inner cylinders for the landing gear, as shown in Figure 2-10. Other significant applications are helicopter rotors, wings, and load-bearing fuselage components on civil (B787 Dreamliner, Airbus A350) and military aircraft (Airbus A400M) [60].
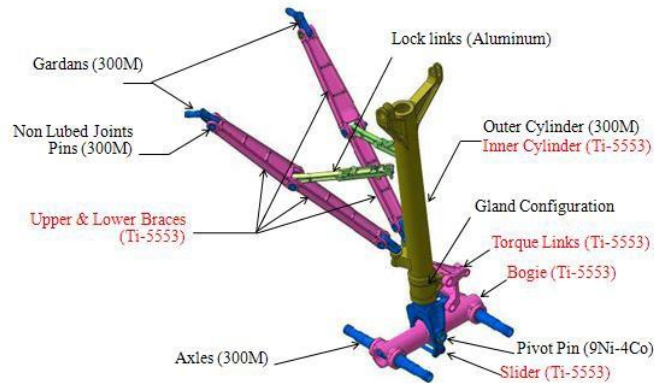
Figure 2-10. Schema of Boeing 787 landing gear, utilizing Ti-5553 for the wing and nacelle application (Reproduced with permission from Refs. [61,62])**.**

While Ti-5553 alloy possesses superior properties for use in the field, it presents formidable machining challenges. The difficulties in machining arise from the inherent properties of the alloy. Because of high chemical reactivity, the metal tends to weld to the machining tool leading to cratering, and premature tool failure. The low thermal conductivity increases the temperature at the tool-workpiece interface, affecting the tool lifespan negatively. The low elastic modulus causes part deflection. The high heat capacity and low conductivity cause heat concentrated at the cutting edge, leading to deformation, wear, cratering, and poor chip control. Lastly, the alloy is work-hardenable which causes notching during the machining [63]. On the other hand, the traditional ingot production route for Ti-5553 alloy parts usually included double- or even triple-vacuum re-melting, this made the

production technology complex and expensive. The high cost of fabrication for titanium alloys, in general, affects their widespread use. Therefore, it is requisite to reduce the cost of fabrication by using near-net-shape processes, minimizing the machining and waste of material, and here is when metal AM enters into the equation.

A limited number of research studies in the existing literature have been reported metal AM processing of metastable and near-β Ti alloys. Several recent studies have been reported on metal AM processing of Ti-24Nb-4Zr-8Sn alloy using PBF [64–71], focusing on optimizing processing conditions or evaluating processing-structure-property relationships. Ti-24Nb-4Zr-8Sn alloy also known as Ti-2448 alloy was developed for use in biomedical implants owing to its low modulus of elasticity and lack of elements with known toxicity in the human body. Few studies have focused on the LDED of Ti-5Al-5Mo-5V-1Cr-1Fe (wt. %) alloy also known as TC18 titanium alloy owing to its good fatigue properties [72–74]. In the case of Ti-5553 alloy, there are few studies reported on the PBF processing [75–80]. To the best knowledge of the author, there are only three research studies on LDED-PF of Ti-5553 alloy [81–83], which are mainly focused on preliminary experimental characterization and/or heat treatment with no effort for process-structure correlation through mechanistic modeling.

2.4 Summary

LDED-PF is still hampered in different degrees by poor quality and uncertainty of the final deposition geometry and properties. Tool-path generation and control of the process need a physics-based modeling approach that is computationally fast and reliable. The mechanistic modeling and ability to tune the process to the microstructure and properties are significantly dependent on the physics-based modeling of temperature. Therefore, the time-consuming numerical modeling is not suitable for this purpose while analytical modeling can be computationally efficient. Although the analytical modeling of multi-track deposition is limited to a few works, its use to obtain solidification parameters is even scarcer in the literature. On the other hand, considering the main advantage of LDED-PF for a reduced need for machining, this method of manufacturing would be beneficial in the case of Ti-5553 alloy that has poor machinability. This research aims to improve the process stability through analytical modeling and gain an increased understanding of the process-structure relationships in LDED-PF of near-β Ti-5553 alloy.

18

Chapter 3: Mathematical Modeling for Rapid Process Mapping in Single-track LDED-PF

3.1 Introduction

This research tries to analytically couple the heat and mass transfer during the process by considering some simplified assumptions. A process map for single-track LDED-PF is developed which draws the physical barriers to a stable process. Besides, an alternative method is established to estimate the deposition profile based on the melt pool projection on the substrate. The model only needs some simple characteristics of the powder stream and laser beam, and thermo-physical properties of the materials, which make it easy to apply the model to any materials/equipment of the same technology. The developed process map can be used to define preliminary processing parameters and it saves time and cost of doing screening-phase experiments. On the other hand, the model is able to perform the dimensions prediction for single tracks with acceptable accuracy. Experiments are designed for assessing the prediction accuracy and finding the shortcomings of the model.

3.2 Mathematical Model

3.2.1 Laser-powder-substrate Interaction

To achieve a high-fidelity model, the interaction among the laser beam, powder stream, and substrate should be considered. As the laser beam heats the fast-moving particles and the substrate, it has to be quantified how much the beam is attenuated while passing through the powder cloud.

3.2.1.1 Velocity of Particles

To find the velocity of the particles, the first assumption is that there is a steady-state powder flow with constant velocity. The particles' pathway from the hopper to the nozzle is long enough such that the velocity of the particles can be assumed equal to the gas flow speed. Then, the effects of drag force and gravity can be ignored. Having a nozzle tip with an annular outlet, and a fully coupled powder and gas flow, the average velocity of particles (v_p) can be given by:

$$v_p = \frac{\dot{V}}{\pi[r_o^2 - r_i^2]}$$

Equation 3-1

where r_i and r_o are the inner and outer radius of the outlet, respectively. $\dot{V}$ is the nozzle volumetric gas flowrate.

3.2.1.2 Attenuation of Laser Beam Intensity by Powder Cloud

Quantifying the attenuated laser power needs the geometry of the powder stream and laser beam. Although the laser beam and powder stream both have a Gaussian intensity distribution in the transverse direction, it has been verified that a nearly uniform intensity distribution can be expected close to the focal position of the laser beam [84] and coaxial powder stream [24,85]. Then, it is well-accepted to consider an effective radius as it leads to the same effective area of the Gaussian and rectangular profiles. The effective radius is the radius where the intensity criterion of $1/e^3$, $1/e^2$ or $1/e$ is applicable depending on the Gaussian mode. In this study, the intensity criterion of $1/e$ is considered to determine the effective radius of the powder stream and laser beam. Please note that the deposition should ideally happen where the focal position of the laser beam and coaxial powder stream locate close to each other on the substrate. Thus, for simplification of the modeling, the powder stream and laser beam close to their focal position are assumed as cylindrical columns with effective radii, and the depiction in Figure 3-1 would be acceptable, showing the powder stream and laser beam as cylindrical columns travelling coaxially along the x-axis. Other assumptions are as follows. The particle size distribution is uniform and particles have a spherical morphology. The effect of diffraction, reflection, and scattering of particles is assumed to be negligible. The particles do not overlap the others. The origin of the coordinate system is assumed at the center of the laser beam spot at the highest point of the deposition.

Since the cylindrical columns do not have the same size, the first ratio to define is the powder efficiency of the nozzle.

$$\xi = \frac{A_l}{A_{ps}}$$

Equation 3-2

where A_l and A_{ps} is the cross-section of laser beam and powder stream cylinders, respectively.
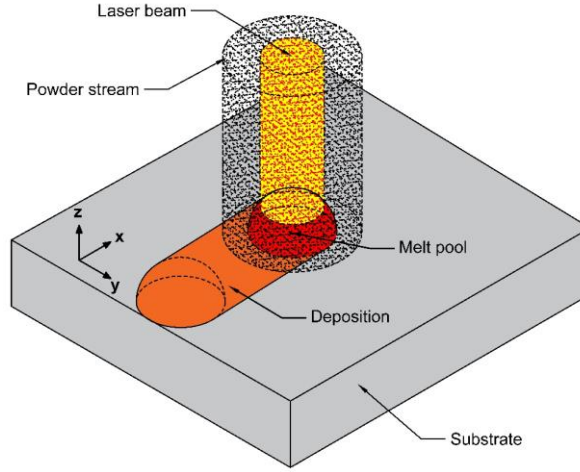
Figure 3-1. Geometric features of the powder stream and laser beam in the LDED-PF process based on the simplified assumptions.

It has been proved that the Beer-Lambert law suffices to obtain the attenuation of a laser beam by a powder cloud [29,38,86,87]. The attenuation depends on the intensity of the incident beam, the concentration and nature of the powder cloud, and the attenuation length. Under the previously mentioned circumstances, the attenuated laser power intensity can be written as:

$$\frac{dI}{I(z)} = -\varepsilon \rho_v dz$$

Equation 3-3

where ρ_v is the mass concentration of powder per unit volume, and ε is an optical factor. Based on the theory of Mie [35], and the geometric optical law (considering scattering and absorption phenomena), the optical factor, as described by Jouvard et al. [38], is as follows:

$$\varepsilon = \frac{3R_p}{2r_p \rho_p}$$

Equation 3-4

where R_p is the reflectivity of powder $(1 - \beta_p)$, β_p is the absorption coefficient of powder, r_p is powder average radius, and ρ_p is powder density.

For a powder stream with a cylindrical shape, uniform mass concentration, spherical-shape powder, and a constant particle's velocity inside the powder stream column, the powder concentration is:

$$\rho_v = \frac{F}{A_{ps}v_p}$$

<center>**Equation 3-5**</center>

where F is powder feed rate (g/s), v_p is velocity of particles (mm/s) flying out of the nozzle, and A_{ps} is the cross-sectional area of the powder stream cylinder.

Finally, the laser beam power attenuation is given by:

$$\int_0^z \frac{dI}{I(z)} = \int_0^z \frac{-\varepsilon F}{A_{ps}v_p} dz$$

$$\ln I_t(z) - \ln I_0 = \ln \frac{I_t(z)}{I_0} = \frac{-\varepsilon F z}{A_{ps}v_p}$$

$$I_t(z) = I_0 \exp\left(\frac{-\varepsilon F z}{A_{ps}v_p}\right)$$

$$P_t(z) = P_0 \exp\left(\frac{-\varepsilon F z}{A_{ps}v_p}\right)$$

<center>**Equation 3-6**</center>

where $P_t(z)$ is transmitted power or attenuated power within the attenuation distance of z, and P_0 is the initial power before attenuation.

3.2.1.3 Energy Balance during Process

The laser energy absorbed by the substrate and powder during the attenuation time is added up and acts as one energy source unit. Assuming a quasi-steady state was achieved during the LDED-PF process, the following energy balance should be fulfilled while ignoring the effect of latent heat of fusion, radiation, and convection [8]:

$$P_{Total}^{Deposition} = P_{Absorbed}^{Substrate} + P_{Absorbed}^{Powder} + P_{Absorbed \, by \, powder}^{Reflected \, by \, substrate}$$

<center>**Equation 3-7**</center>

where the total power of deposition ($P_{Total}^{Deposition}$) is the sum of the power absorbed by the substrate ($P_{Absorbed}^{Substrate}$), power absorbed by the powder ($P_{Absorbed}^{Powder}$), and power reflected by the substrate and absorbed by powder ($P_{Absorbed\ by\ powder}^{Reflected\ by\ substrate}$).

The power released by the laser beam after its transmission through the powder cloud and getting absorbed by the substrate is:

$$P_{Absorbed}^{Substrate} = \beta_s P_t(z) = \beta_s P_0 exp\left(\frac{-\varepsilon F L_{att}}{A_{ps} v_p}\right)$$

Equation 3-8

where β_s is the absorptivity factor for the substrate.

As the nozzle injects the powder, particles interact with the laser beam within the attenuation distance and accumulate energy. The energy absorbed by one particle during the attenuation time is given by [38]:

$$dq_p = \frac{\beta_p A_p}{A_l} P_t(z) dt$$

Equation 3-9

where β_p is the absorptivity factor for the particles, and A_p is the cross-sectional area of the particle The attenuation time is a function of the attenuation length (L_{att}) and velocity of particles, so we can write the energy based on the attenuation distance.

$$dt = \frac{dz}{v_p}$$

Equation 3-10

Considering no convection and radiation losses, the energy absorbed by one particle is described below.

$$q_p = \frac{\beta_p A_p}{A_l v_p} \int_0^{L_{att}} P_t(z) dz$$

Equation 3-11

However, a number of particles are absorbing energy while they are flying. The number of particles per unit time is:

$$N = \frac{\xi F}{m_p}$$

<div align="center">Equation 3-12</div>

where m_p is the average mass of a particle. The total power released by these particles is:

$$P_{Absorbed}^{Powder} = \frac{N\beta_p A_p}{A_l v_p} P_0 \int_0^{L_{att}} exp\left(\frac{-\varepsilon F z}{A_{ps} v_p}\right) dz$$

<div align="center">Equation 3-13</div>

On the other hand, the reflected part of the energy by the substrate would be again absorbed by the particles. The particles absorb the energy and transfer it back to the melt pool. The reflected power by the substrate that is absorbed by particles is as follows:

$$P_{Absorbed\ by\ powder}^{Reflected\ by\ substrate} = \frac{N\beta_p A_p}{A_l v_p}(1 - \beta_s)P_0 \int_0^{L_{att}} exp\left(\frac{-\varepsilon F z}{A_{ps} v_p}\right) dz$$

<div align="center">Equation 3-14</div>

3.2.1.4 Heat Conduction during Process

Assume that a stationary point heat source travels with a constant velocity along the x-axis. Then Rosenthal's solution for the quasi-steady-state temperature distribution on the surface of a semi-infinite plate is given as follows:

$$T_{ss}(x, y, z) = T_0 + \frac{P_{Total}^{Deposition}}{2\pi k R} e^{\frac{-v(x+R)}{2\alpha}}$$

<div align="center">Equation 3-15</div>

where $R = \sqrt{x^2 + y^2 + z^2}$, T_0 denotes the ambient temperature, $P_{Total}^{Deposition}$ denotes the total deposition power, v is the laser moving velocity, k and α denote the average thermal conductivity and diffusivity of powder and substrate material. The parameter R denotes the distance from the point of interest to the laser heat source.

To cover more physical phenomena and make the model more realistic, some modified factors are taken into account. To take the remelted zone of the substrate or dilution ratio (D) into consideration, it is assumed that the average contribution of the remelted zone to the melt pool is 25 % ($D = 0.25$).

The dilution ratio is usually between 0-50 percent, depending on the processing parameters, hence the average of 25 % would be reasonable.

$$\begin{cases} k = k_{powder}(1-D) + k_{substrate}(D) \\ c_p = c_{powder}(1-D) + c_{substrate}(D) \\ \rho = \rho_{powder}(1-D) + \rho_{substrate}(D) \\ T_m = T_m^{powder}(1-D) + T_m^{substrate}(D) \end{cases}$$

Equation 3-16

The effect of fluid motion (Marangoni effect) can be taken into consideration by a modified thermal conductivity [26,88].

$$k_t^* = \mu k_t, \quad T > T_m$$

Equation 3-17

where μ is a correction factor for enhanced thermal conductivity. The correction factor has been reported to be between 1-5 depending on the material [88–90].

The absorptivity is related to the angle of incidence. The absorptivity of an inclined surface in the polarization plane is given as [91]:

$$\beta(\varphi) = \frac{4n_r cos\varphi}{(n_r cos\varphi + 1)^2 + k_e^{\,2} cos^2\varphi}$$

Equation 3-18

where φ is the inclination angle, n_r is refraction index, and k_e is the extinction index of the material. If the cross-section of the deposit is assumed to be a segment of a circle, the inclination angle is approximated as:

$$\varphi = \tan^{-1}\left(\frac{2H}{W}\right)$$

Equation 3-19

where H is the deposit height and W is the deposit width. To make this simple, if the deposit forms a semicircle ($H = W/2$), then the inclination angle would be almost $45°$. This can be also applied to the absorption coefficient of powder to compensate for the inclined plane because of the sphericity of

particles, assuming that the laser beam gets reflected under the average angle of 45° due to the rounded shape of particles.

3.2.2 Melt-pool/deposit Dimensions

To get the dimensions, the projection of the melt pool on the substrate (x-y plane) is firstly needed. It can be approximately represented by the liquid-solid isotherm (Γ) on the top surface of the substrate.

$$T(x, y, z) - T_0 = \Gamma(x, y, z)$$

Equation 3-20

Figure 3-2 shows the boundary of the melt pool projection on different planes, as suggested by Huang et al. [18], and the following conditions denote the liquid-solid isotherms for coordinate points as A, B, C, and D.

$$\begin{cases} \Gamma(0, y_A, 0) = T_m - T_0, y_A > 0 \\ \Gamma(0, y_B, 0) = T_m - T_0, y_B < 0 \\ \Gamma(x_C, 0, 0) = T_m - T_0, x_C > 0 \\ \Gamma(x_D, 0, 0) = T_m - T_0, x_D < 0 \end{cases}$$

Equation 3-21
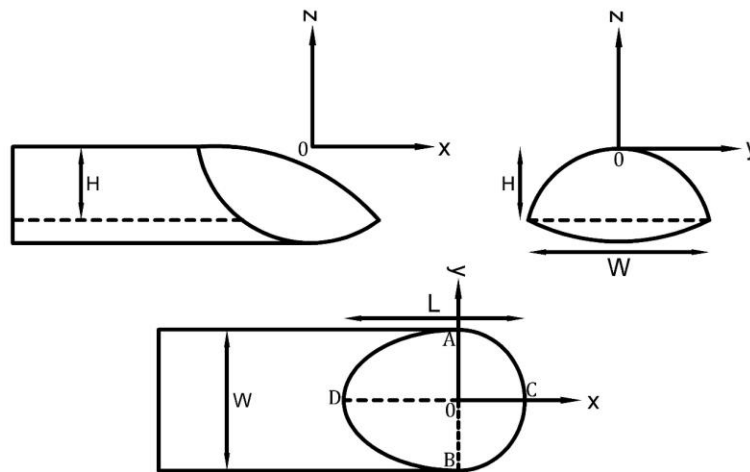
Figure 3-2. Schematic depiction of melt pool projection on x-y, y-z, and x-z and planes (Redrawn from Ref. [18]).

The length (L) and width (W) of the melt pool on the x-y plane according to the boundary are defined as:

$$L = x_C - x_D, W = 2|y_A| = 2|y_B|$$

Equation 3-22

To find the deposit maximum height, the catchment efficiency needs to be defined. It can be defined as the area of the melt pool projection on the x-y plane over the cross-sectional area of the powder stream column.

$$\eta = \frac{A_m}{A_{ps}} = \frac{\pi WL}{4\pi r_{ps}^2}$$

Equation 3-23

where A_m can be found based on the boundary of the melt pool projection on the x-y plane, and r_{ps} is the effective radius of the powder stream. Then, the deposit height can be found based on the conservation of mass (continuity). The mass flow rate through the melt pool cross-sectional volume is constant. Assuming the cross-section of deposit on the y-z plane is a parabolic segment, the cross-sectional area would be:

$$A_d = \frac{2}{3} WH$$

Equation 3-24

The powder mass flow rate injected into the melt pool volume defines the height.

$$\eta F = \rho v A_d$$

$$\frac{\pi WL}{4\pi r_{ps}^2} F = \frac{2}{3} \rho v WH$$

$$H = \frac{3LF}{8\rho v r_{ps}^2}$$

Equation 3-25

3.2.3 Determination of Threshold Limits for Process Mapping

3.2.3.1 Laser Power of Deposition

The power required to form a deposit with a specific width can be derived from Equation 3-15. The equation can give the initial power given by the laser beam (P_{dep}) to form a deposit with a specific width. The boundary condition is that the temperature on the top surface at the coordinate of $(0, y, 0)$ is equal to the melting temperature of the deposit, where y can be the radius of the deposit with respect to the radius of the laser beam.

$$x = 0, z = 0, y = 2r_l; R = 2r_l$$

$$T_{dep} - T_0 = \frac{1}{2\pi kR} \left[P_{Total}^{Deposition} \right] e^{\frac{-v(R)}{2\alpha}}$$

$$2\pi kR(T_{dep} - T_0)e^{\frac{+v(R)}{2\alpha}}$$

$$= \beta_s P_{dep} exp\left(\frac{-\varepsilon F L_{att}}{A_{ps}v_p} \right) + \frac{N\beta_p A_p}{A_l v_p} P_{dep} \int_0^{L_{att}} exp\left(\frac{-\varepsilon F z}{A_{ps}v_p} \right) dz$$

$$+ \frac{N\beta_p A_p}{A_l v_p}(1 - \beta_s)P_{dep} \int_0^{L_{att}} exp\left(\frac{-\varepsilon F z}{A_{ps}v_p} \right) dz$$

Equation 3-26

3.2.3.2 Laser Power of Powder Fusion

The particles should be melted before reaching the melt pool; otherwise, the quality of the deposit is affected. Not only do non-melted and partially melted particles affect the stability of the deposition process but also they may help porosity formation. The accumulated energy by the particle by the time they reach the substrate is consumed to heat the particles. Here, to define this threshold for the initial laser power for powder fusion (P_{pf}), it is assumed that the energy absorbed by particles is completely consumed for particles' fusion.

$$\frac{N\beta_p A_p}{A_l v_p} P_{pf} \int_0^{L_{att}} exp\left(\frac{-\varepsilon F z}{A_{ps}v_p} \right) dz + \frac{N\beta_p A_p}{A_l v_p}(1 - \beta_s)P_{pf} \int_0^{L_{att}} exp\left(\frac{-\varepsilon F z}{A_{ps}v_p} \right) dz$$

$$= Nm_p c_p\left(T_{pf} - T_0\right) + Nm_p L_f$$

28

Equation 3-27

where c_p is the specific heat capacity of powder, and L_f is the latent heat of fusion.

3.2.3.3 Laser Power of Stable Melt Pool

When the power density is too low or high, the material can be not melted or vaporized from the melt pool. In the case of high power density, the generated heat can penetrate to a deeper depth, causing high dilution that is not desirable. On the other hand, the possible formation of a plasma in this condition can complicate the situation. This may deteriorate the process efficiency and quality of the deposits. Thus, it is important to define the threshold for material vaporization [92,93].

An analytical approach of utilizing normalized enthalpy has been effectively used to relate the vaporization threshold to the parameters of the laser processing. This method has been used by Hann et al. [94] and Fabbro [95] for laser welding, and King et al. [96] and Rubenchik et al. [97] expanded this method to laser-aided additive manufacturing. The linear dependence of the normalized melt pool depth to the normalized enthalpy has been shown in previous studies, where the enthalpy or energy density (ΔH) can be represented as the energy absorbed during the interaction time over the heat diffusion volume.

The heat diffusion volume for one-dimensional heat flow can be assumed as the volume of a cylinder. The section of the cylinder is assumed as a circle.

$$Diffusion\ volume = \pi r_l^2 \delta$$

Equation 3-28

where $\delta = \sqrt{\alpha t_i}$, $t_i = 2r_l/v$, r_l is the radius of the cylinder equals the effective laser beam radius and δ is the height of the cylinder equals the heat diffusion depth during the interaction time (t_i) for one-dimensional heat flow.

With these assumptions, the energy density can be found as:

$$\Delta H = \frac{P_{Total}^{Deposition} t_i}{Diffusion\ volume} = \frac{\sqrt{2} P_{Total}^{Deposition}}{\pi \sqrt{\alpha v r_l^3}}$$

Equation 3-29

29

The normalized enthalpy is $\Delta H / h_s$, where ΔH is the specific enthalpy calculated above, h_s is the enthalpy at melting equals to $\rho c_p (T_m - T_0)$. The normalized enthalpy can be used to identify the thresholds where instabilities in melt pool formation happen. The melt pool instabilities, as defined by Hann et al. [94], happen when the enthalpy is smaller than enthalpy at melting and greater than enthalpy at vaporization. Hann et al. [94] showed that enthalpy at vaporization over enthalpy at melting is roughly equal to 10 for most metallic alloys. The assumption of $\Delta H / h_s = 10$ can define a threshold when the material vaporization starts to happen (P_{mv}). The assumption of $\Delta H / h_s = 1$ can similarly define another threshold when material fusion happens (P_{mf}).

3.3 Experimental Procedures

Spherical plasma-atomized Ti-5Al-5V-5Mo-3Cr (Ti-5553) alloy powder (AP&C, GE Additive) with particle size ranged from 45 to 106 µm (shown in Figure 3-3) was deposited on the plates made of Ti-6Al-4V (Ti-64) alloy (McMaster-Carr) by an LDED-PF setup (DMD®-IC106, DM3D Technology). The LDED-PF system (shown in Figure 3-4) is equipped with an ABB robotic control system, a disk laser (TruDisk 2000, TRUMPF) with the maximum power of 2 KW and wavelength 1030 nm, and a dual powder feeder that is used to feed the metallic powder through a coaxial nozzle.
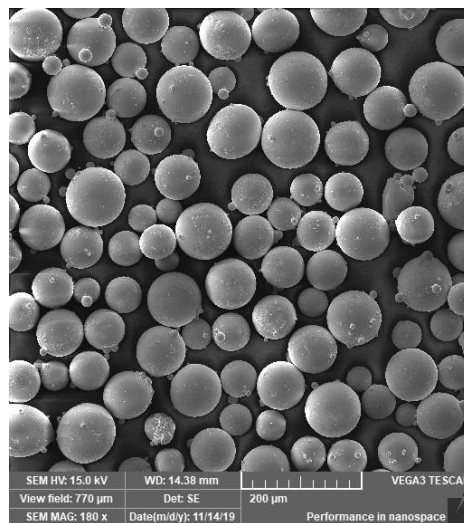
Figure 3-3. SEM image of the feedstock Ti-5553 powder.
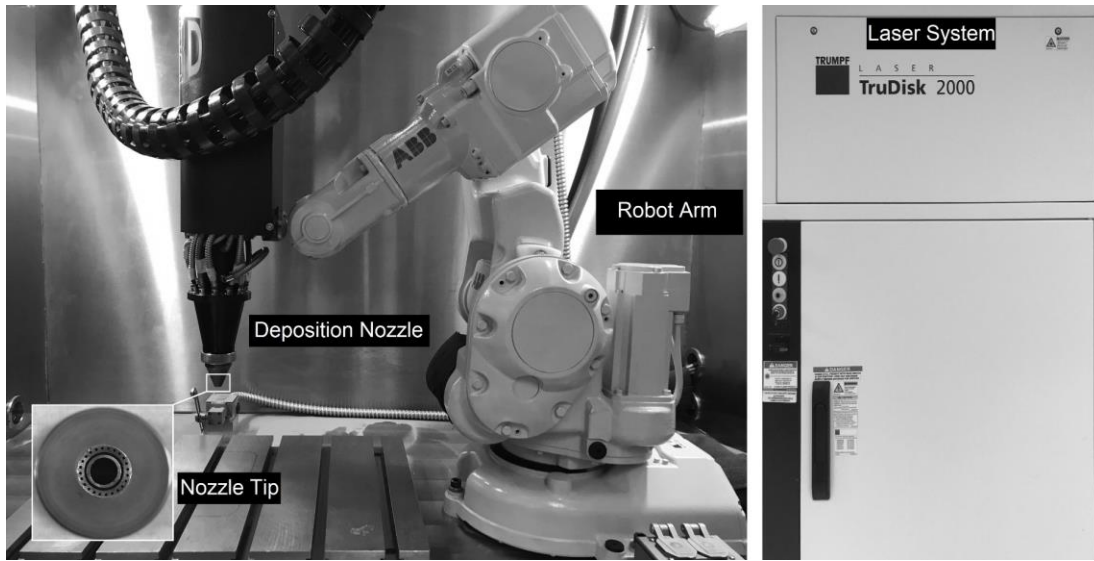
Figure 3-4. Robotic LDED-PF equipment used in this study.

The thermal parameters of both substrate and feedstock powder (Table 3-1) are averaged out over the range of room to melting temperature as the thermophysical properties of materials are temperature-dependent. Single-track depositions were conducted at different laser power and carrier gas to validate the model. Each experiment group was repeated three times and the process parameters are listed in Table 3-2.

Table 3-1. Thermophysical properties of the materials

Material	Melting Temperature [K]	Density [g/cm^3]	Thermal conductivity [W/m·K]	Specific heat [J/(g·K)]
Ti-5553	1923	4.3 (298 K)-3.4 (1923 K)	5 (298 K)-29 (1923 K)	0.53 (298 K)-0.75 (1923 K)
Ti-64	1928	4.4 (298 K)-3.9 (1928 K)	17 (298 K)-34 (1928 K)	0.57 (298 K)-0.85 (1928 K)

Table 3-2. Technical and processing parameters of LDED-PF

Parameter	Value
Laser moving velocity	11 mm/s

Powder feed rate	14.5 g/min
Nozzle standoff distance	10 mm
Laser power	250, 500, 1000, 1500, 1750 W
Carrier gas flow rate (Argon)	1.1, 1.7, 4.7, 7.8, 9.3 L/min
Cover gas flow rate (Argon)	8 L/min
Nozzle gas flow rate (Argon+Helium)	6 and 4 L/min
Shaping gas flow rate (Argon)	6 L/min

The powder stream videos were taken by a high-speed camera (VEO 710, Phantom) equipped with a Canon EF 180mm F/3.5L Macro USM Lens. The average particle's velocity was experimentally measured by the available tool of Phantom CineViewer (CV) software. In this study, the effective radius is considered as the distribution reaching $1/e$ of the peak concentration value. Thus, in a simple way, the powder stream is a cylinder with an effective radius of 2.5 mm and a height of 4 mm. Kapton films with a thickness of 100 µm were used to determine the laser spot size. One pulsation of laser with the power of 60 W and a duration of 1 ms was used at different standoff distances to find the laser spot size at different distances from the nozzle tip. The burnt spots on the Kapton films were then measured by optical microscopy. Each beam condition was repeated four times for the calculation of a mean and standard deviation. A portable power meter (PMT 05p, PRIMES GmbH) is used to measure the laser power. The attenuation of the laser beam by the powder cloud at different gas and powder parameters is investigated by the power meter. The power meter was placed at the standoff distance, as the substrate, and the laser fired at a low laser power of 60 W for 20 seconds while the powder feeder was on.

To examine the dimensions of the single-tracks, a laser scanning confocal microscope (VK-X250, Keyence) is used. All the single-track deposits were cross-sectioned at the mid-track length and then mounted, ground, polished, and etched to investigate the microstructure by optical and scanning electron microscopy (VEGA3, TESCAN). The mathematical model is implemented in Matlab® R2019a by a DELL® computer with Intel® CoreTM i7-7700 CPU 3.6GHz.

3.4 Results and Discussion

3.4.1 Velocity of Particles

Figure 3-5 shows the comparison of the average velocity of particles for the model-predicted values and experimental values based on different volumetric gas flow rates. The volumetric gas flow rates are obtained by adding up the cover gas flow rate and carrier gas flow rate that is divided into 4 pipelines. The graph implies that the assumption of assuming the velocity of the particles equal to the gas flow rate speed is more or less valid. The difference can lie behind the effect of the drag force and the error of the measurements.
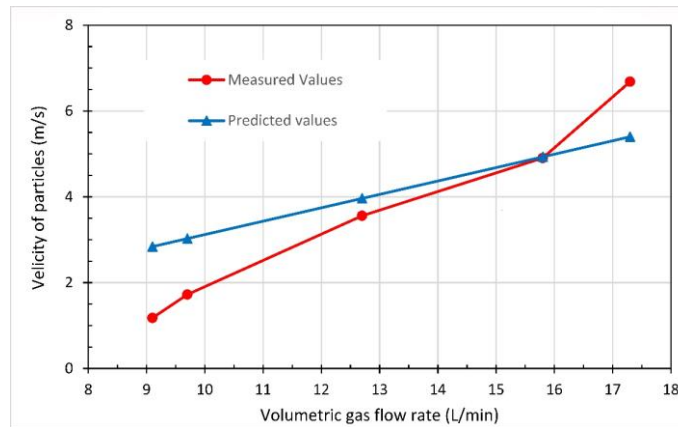
Figure 3-5. Experimental and model predicted values for velocity of particles.

3.4.2 Laser Beam Profile

The laser beam spot size on the focal position is a critical parameter in laser materials processing. Indirect measurement of the burnt contour on Kapton films is an easy and inexpensive method to determine the approximate laser beam spot size [98]. Depending on laser beam power intensity, the Kapton undergoes pyrolytic decomposition or vaporization, forming a distinct burnt contour that can be easily measured as an effective laser beam diameter. Figure 3-6 shows an example of this method expresses the laser spot size at different standoff distances.
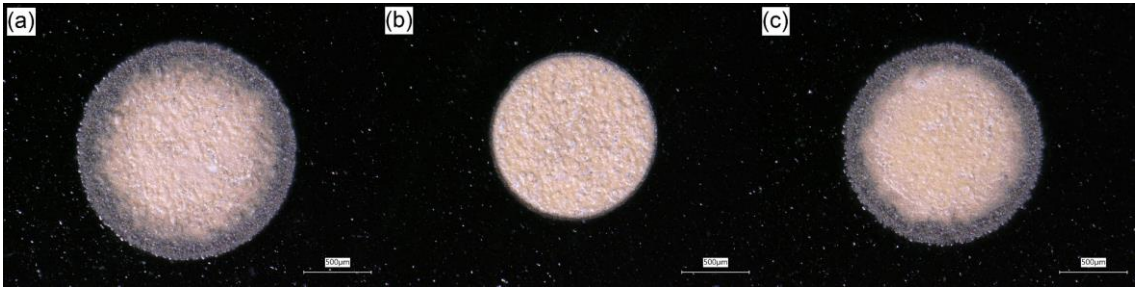
Figure 3-6. Burnt spot formed on the Kapton film at different distances from the nozzle tip; (a) 5 mm, (b) 15 mm, and (c) 25 mm.

Figure 3-7 shows the laser beam profile based on the measurements of burnt spots formed on the Kapton film at different distances from the nozzle tip. The waist of the beam is at a standoff distance of 15 mm, the beam radius at the waist is 0.6 mm, and the far-field divergence angle is 4.6°.
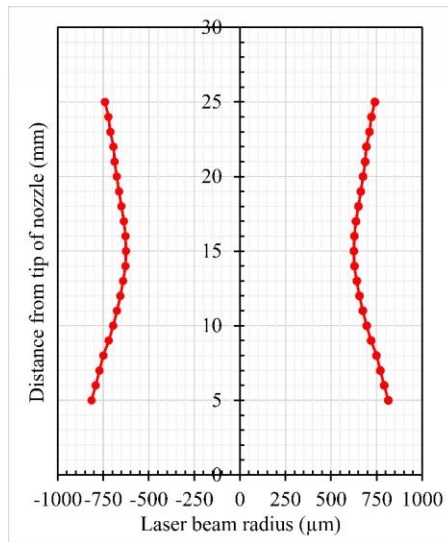
Figure 3-7. The laser beam profile according to the measurements on Kapton films.

3.4.3 Attenuation of Laser Beam Intensity by Powder Cloud

Figure 3-8 shows the comparison of predicted and measured values of the attenuated laser power as a function of the particles' velocity and powder feed rate. The maximum laser beam attenuation percentage is predicted at around 8% at the highest powder feed rate (14.5 g/min) and lowest velocity of particles (1.4 m/s). However, the graphs show some contradictory results between the measured and predicted values.

34
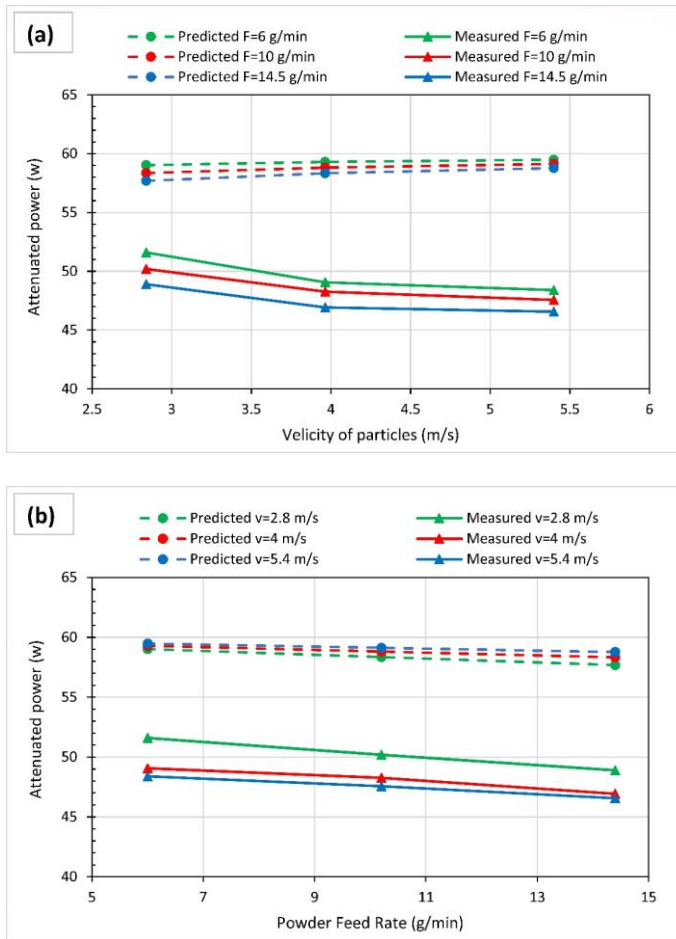
Figure 3-8. Attenuated laser power as a function of velocity of particles (a) and powder feed rate (b).

The source of error could be attributed to the method of measurement. One of the main assumptions of the model is that the powder particles, interacting with the laser beam, are effectively attached to the liquid flow and become part of the melt pool. However, at the low power used for the measurement, no melt pool forms, and particles hit the surface of the power meter and bounce back into the laser-beam column, double attenuating the laser power and cause the mismatch between predicted and measured values. Especially as the velocity of the particles increased, the mismatch becomes higher as particles with high velocity can bounce back a higher distance and attenuate the laser beam more.

3.4.4 Melt-pool/deposit Temperature Distribution

Figure 3-9 shows the melt pool temperature distribution based on the model implemented in Matlab. The melt pool boundary is identified by the liquid-solid isotherm. The deposit bead curvature is defined based on the polynomial curve fitting to the data points of the width and maximum height. The only drawback is the temperature prediction at the points close to $(0,0,0)$ position. Rosenthal's solution is based on a point heat source and it results in the prediction of very high temperatures for those points. To deal with this, the maximum temperature threshold should be defined and the area close to $(0,0,0)$ position ends up with the same temperature distribution; however, the temperature prediction at the points far from the $(0,0,0)$ position would be accurate enough for the prediction of the liquid-solid isotherms.
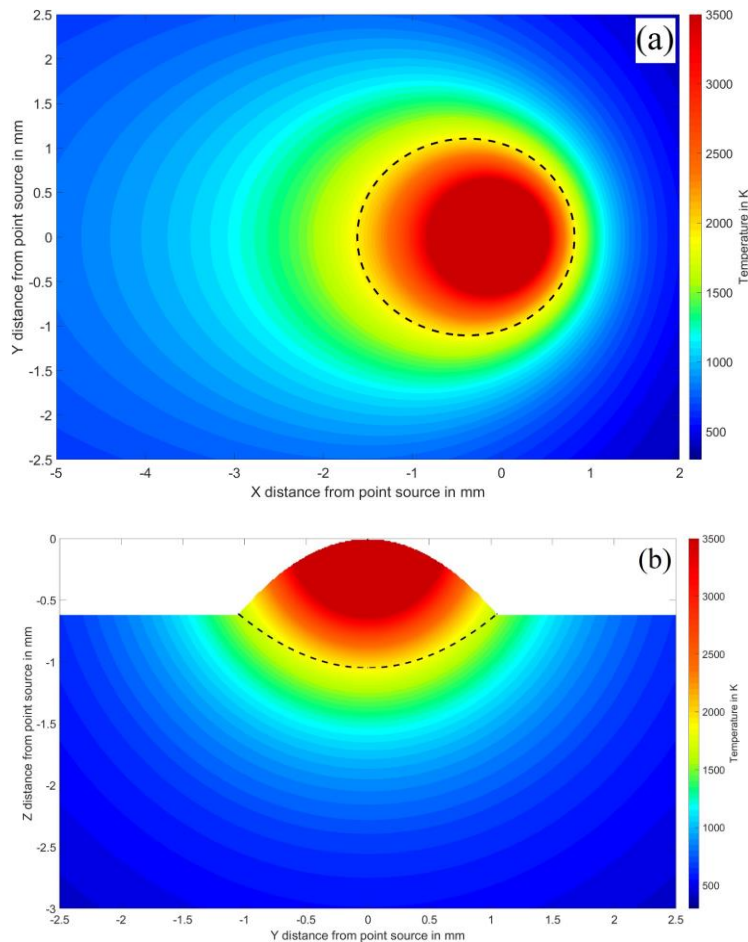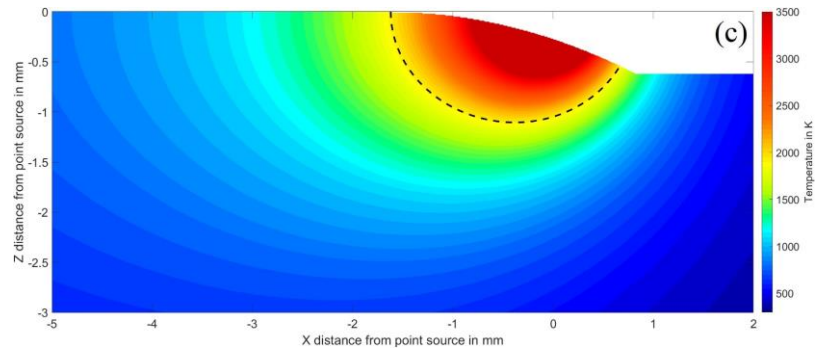
Figure 3-9. Melt pool temperature field in different planes. (a) xy plane (substrate surface), (b) yz plane (transverse cross-section), (c) xz plane (longitudinal cross-section) (P=1000 W, $\dot{V}$=9.7 L/min, F=14.5 g/min and v=11 mm/s). The melt pool boundary is indicated by the black dashed line (T=1931 K).

3.4.5 Melt-pool/deposit Dimensions

The geometrical features such as height and width are measured by a KEYENCE laser confocal microscope based on the transverse cross-section and 3D contour of the deposits. Figure 3-10 and Figure 3-11 show the transverse cross-section and 3D contour of the deposits at different laser powers.
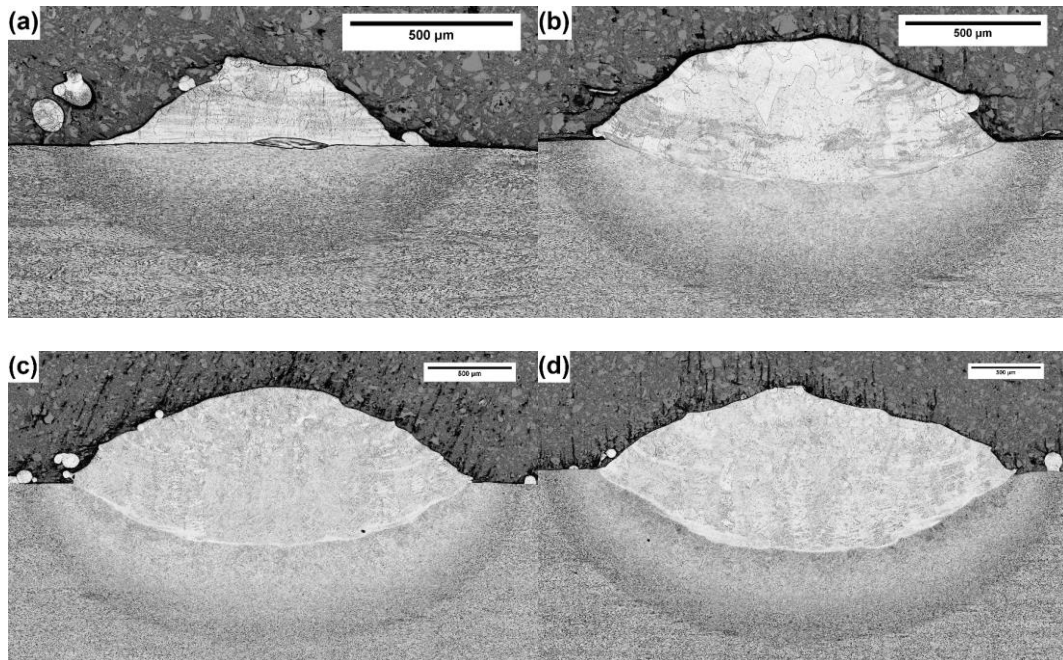
Figure 3-10. Transverse cross-section of deposits at different laser powers of (a) 250 W, (b) 500 W, (c) 1000 W, and (d) 1500 W ($\dot{V}$=9.7 L/min, F=14.5 g/min and v=11 mm/s).
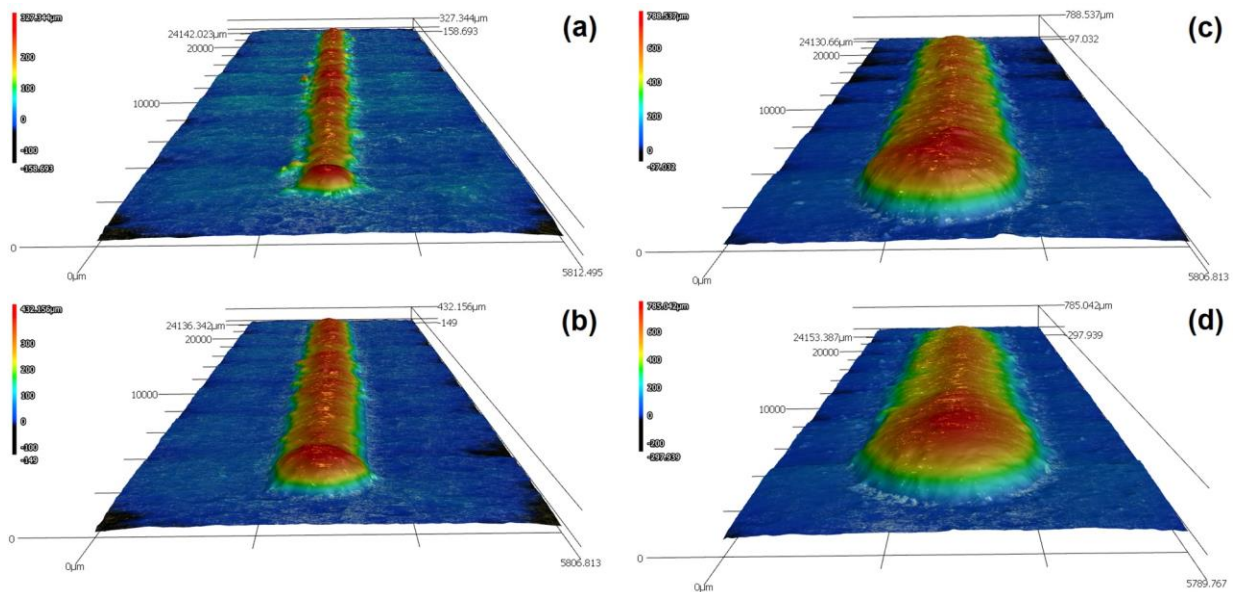
Figure 3-11. 3D contour of single deposits at different laser powers of (a) 250, (b) 500, (c) 1000, and (d) 1500 W ($\dot{V}$=9.7 L/min, F=14.5 g/min and v=11 mm/s).

Figure 3-12 compares the predicted and measured deposit dimensions with varying laser power and carrier gas flow rate. The measured results have low standard deviation values and only average values are plotted. The predicted values more or less match with the measured ones. With increasing laser power, the deposit width, dilution, and height increase; however, the effect of carrier gas flow rate or velocity of particles is negligible. It should be mentioned that the correction factor for the enhanced thermal conductivity is anisotropic and it may be different in different directions, usually greater in the depth direction than the in-plane direction [88–90]. In this work, the correction factor of thermal conductivity is assumed to be 2 to find the width of the melt pool and 2.5 for finding the depth of the melt pool. As the Marangoni effect is more pronounced in the z-axis, a larger correction factor should be considered for the melt pool depth.
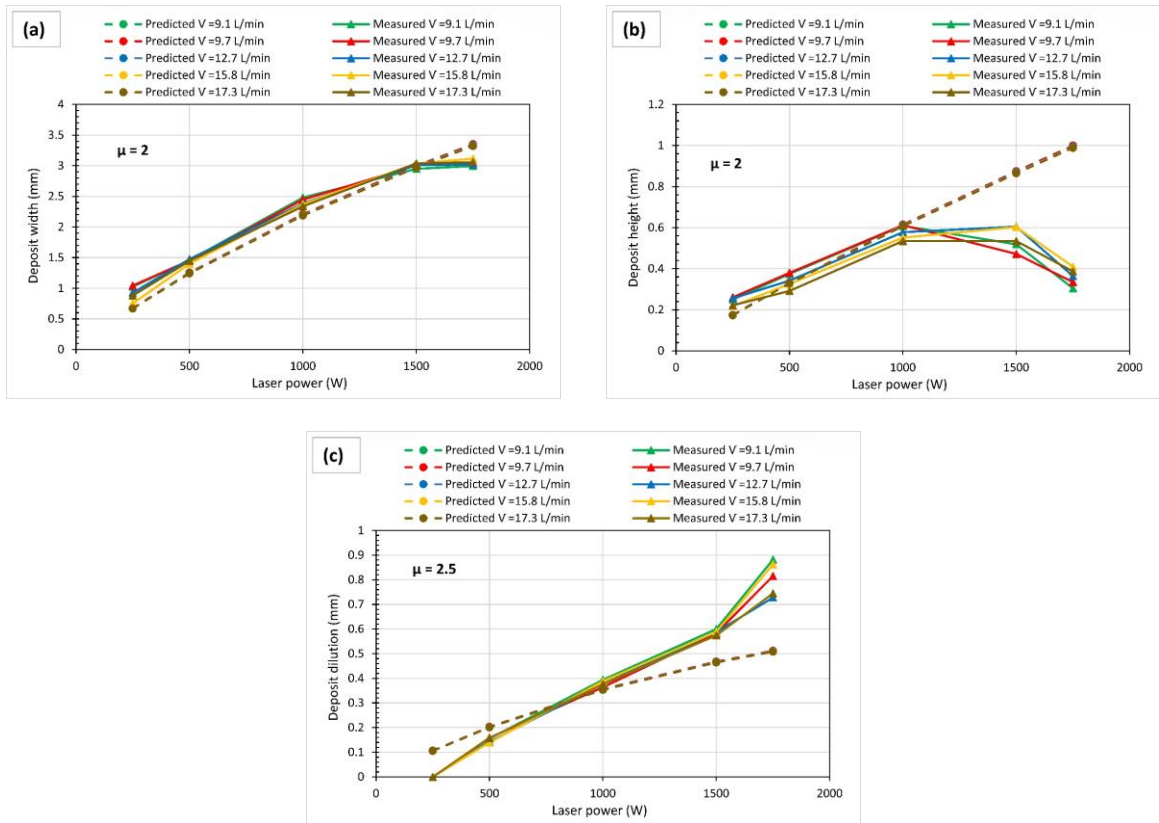
Figure 3-12. Measured and predicted values for the deposit dimensions in different laser powers and carrier gas flow rates using two correction factors (μ) for the enhanced thermal conductivity (F=14.5 g/min and v=11 mm/s); (a) width (μ=2), (b) height (μ=2), and (c) dilution (μ=2.5).

The particles' velocity has a minor effect since the attenuation time is very short. There is a small discrepancy between predicted and measured values, which is normal for an analytical model that entails several simplifications. The source of errors may attribute to the simplifications for considering the average thermophysical properties over the temperature range, ignoring the effect of gravity and drag force on velocity of particles, and disregarding convection and radiation losses. Based on the measured values, there are major discrepancies in the deposit dimensions depending on the laser power. At laser power of 250 W, the relative error of predicted and measured values is high. The relative error is high in the case of laser powers of 1500 and 1750 W, too. At laser powers of 500 and 1000 W, the relative error for the height, dilution, and width is 5-20 %, which is acceptable for an analytical model. The source of errors may attribute to the governing physics that are not considered in the model and change the heat transfer situation. The first simplifying assumption is that the injected powder from the

nozzle must completely be melted and attracted by the melt pool. If this condition is not satisfied, the deposition process would be unstable, leading to a high discrepancy between the predicted and measured values. The second assumption is that the power density must be in range in order to ensure that stable melt pool forms and the material is not vaporized. If this condition is not satisfied, a lack of fusion and vaporization would lead to a high discrepancy between predicted and measured values. The procedure for the determination of these threshold limits is presented in the previous section and results are presented in the following section.

3.4.6 Developed Process Map

By implementing the model in Matlab, the different thresholds can be drawn for the LDED-PF process. In Figure 3-13, the laser power is plotted as a function of velocity of particles in the case of single-track depositing of Ti-5553 powder on Ti-64 plates. The black solid line shows the deposition power (P_{dep}) of forming a deposit with a specific width ($W = 2r_l$). The blue solid line show the required power of particles' fusion (P_{pf}) before they reach the melt pool. The two red solid lines are the thresholds of forming a stable melt pool. The first one is the required power for material fusion (P_{mf}) and the second one is power at which material vaporization starts to happen (P_{mv}). The intersections of these lines form different zones indicating different regimes for the LDED-PF process. The zone below P_{pf} is not preferred as the particles have a temperature below the melting point and they may cause instability in the process. However, the deposition can be still done in the zones below P_{pf}, the results would not be desirable. Similarly, the zones below P_{mf} and above P_{mv} is not desirable since no stable melt pool forms beyond them. The zone highlighted in green would be the optimal processing zone for LDED-PF of Ti-5553 (75 µm average size) on the Ti-64 substrate at the given powder feed rate and laser moving velocity and the dimensions prediction of the model is valid with good accuracy. This figure clearly shows the crucial role of laser power and velocity of particles in defining the processing zone. The particles' velocity has a minor effect on P_{dep}. However, it has a major effect on P_{pf}. In fact, P_{pf} increases linearly as the velocity of particles increases.
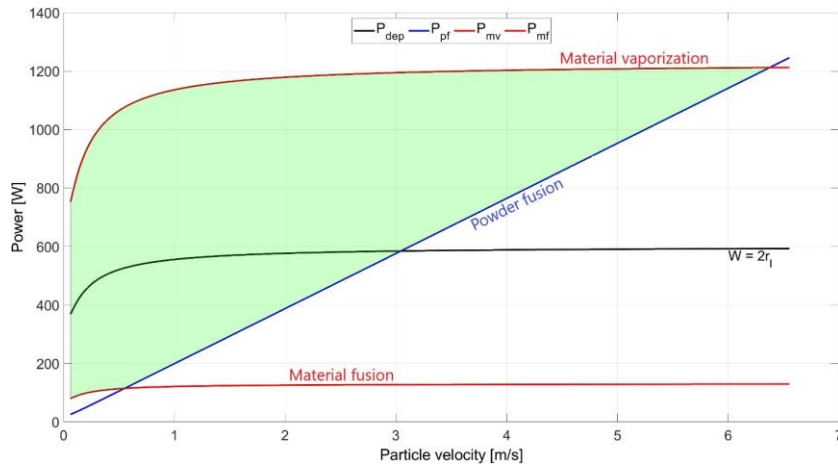
Figure 3-13. The modeled process map representing laser power versus velocity of particles for LDED-PF of Ti-5553 on the Ti-64 substrate (F=14.5 g/min and v=11 mm/s).

3.4.7 Microstructure of Deposits

Figure 3-14 shows the microstructure of single deposits that were fabricated at different laser powers when other processing conditions were kept constant. The single deposit printed at 250 W showed a dendritic structure of the β-Ti phase (Figure 3-14a). However, increasing laser power tends to generate a martensitic α/β structure (Figure 3-14b-d).
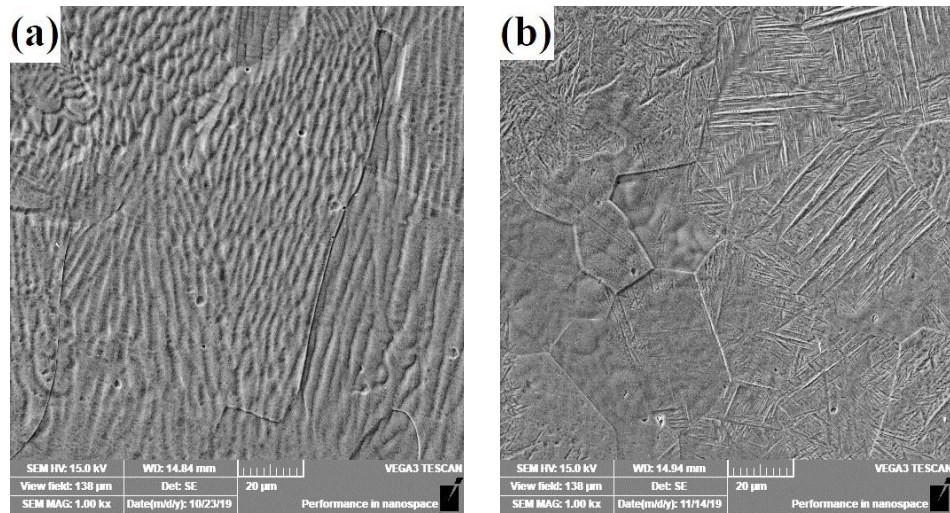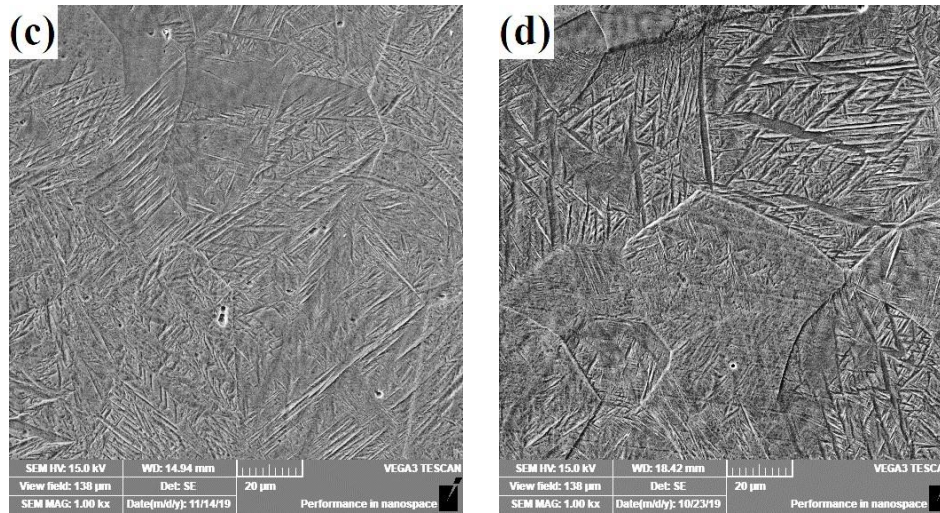
Figure 3-14. SEM micrographs for the typical microstructure in the Ti-5553 single deposits on Ti-64 substrate at different laser powers; (a) 250, (b) 500, (c) 1000, and (d) 1500 W ($\dot{V}$=9.7 L/min, F=14.5 g/min and v=11 mm/s).

The reason for this microstructural change lies behind the chemical composition change caused by dilution. As the laser power increases, the dilution level of the deposit and substrate increases. The substrate is the Ti-64 alloy with less amount of β-stabilizing elements. The dilution decrease the molybdenum and chromium content of the deposits and leads to the martensitic α/β structure. The EDS results from the transverse cross-sectional area of the deposits (Table 3-3) confirm that the increased laser power and following dilution decreases the molybdenum and chromium content. This finding can benefit the process. The first layers can be printed by the parameters that lead to less dilution such that the chemical composition remains untouched, especially in the case of using a substrate of different chemical composition, and the process can be continued by other processing parameters.

Table 3-3. Normalized mass concentration [%] of the deposits at different laser power obtained by EDS

	Titanium	Aluminum	Vanadium	Molybdenum	Chromium
Deposit at 250 W	81.18	5.26	5.86	5.99	1.70
Deposit at 500 W	83.81	5.81	5.64	3.51	1.23
Deposit at 1000 W	84.82	5.49	5.28	3.26	1.14
Deposit at 1500 W	85.85	5.67	5.41	2.25	0.82

3.5 Summary

A mathematical model of LDED-PF was developed to couple the heat and mass transfer by the attenuated laser power and heated powder particles. The energy balance was considered with Rosenthal's solution for a moving heat source to obtain the temperature field and melt pool dimensions. The experimental validation was performed using the single-track deposition of Ti-5553 and it showed the accuracy of the model depends on the processing parameters. The non-optimized processing parameters led to the vaporization or lack of fusion, resulting in a high discrepancy in the results. A process map was developed to complete the model based on a few important physical phenomena to avoid problematic processing parameters. Those non-optimum processing parameters can be avoided by the process map. By identifying the optimal processing region on the process map, the model is able to predict the dimensions of the single-track deposits with more than 80% accuracy. This model gives general insights into the LDED-PF process and can act as a guideline on the processing parameter selection that governs the major aspects of the process.

Chapter 4: Analytical Solutions for Transient Temperature Field in LDED-PF Based on Different Heat Source Models

4.1 Introduction

The first and important step in modeling the LDED-PF process is the establishment of an appropriate heat source model since not only does the heat source influence the dimensions prediction of the melt pool, but also it has a strong impact on the accuracy of temperature field prediction. An assessment of the roles of different heat source models is important to understand the simulated results that provide insights into the thermal cycles. In this chapter, approximate analytical solutions for 1D, 2D, and 3D heat sources in semi-infinite homogeneous solid are proposed. The temperature field and melt pool dimensions prediction for single-track deposition are compared based on different heat source models. The validity and accuracy of the proposed solutions are discussed, and the best solution is calibrated for Ti-5553 single-tracks by linear functions for enhanced thermal diffusivity and heat source size. The sensitivity analysis is also carried out to evaluate the influence of main thermophysical properties and processing parameters on the model outputs.

4.2 Model Formulation

4.2.1 Temperature Field

In the LDED-PF process, there is a heat flux and each point has a transient temperature field. The governing diffusion equation for heat conduction of a heat source Q_t is as follows:

$$k \left(\frac{\partial^2 T}{\partial x^2} + \frac{\partial^2 T}{\partial y^2} + \frac{\partial^2 T}{\partial z^2} \right) + Q_t = \rho c \frac{\partial T}{\partial t}$$

Equation 4-1

where ρ denotes the material density, c denotes the specific heat, and k denotes the thermal conductivity. As shown in Figure 4-1, suppose that a heat quantity δQ_t acts instantaneously at the time t' in a semi-infinite body, and it can move with a constant linear speed of v_x and v_y along the x-axis and y-axis, respectively. To mathematically quantify the heat flux, the above-mentioned equation can be solved by the use of Green's function.

$$dT = \frac{dQ_t dt'}{4\rho c\left(\pi\alpha(t-t')\right)^{3/2}} exp\left(-\left(\frac{(x-v_x t')^2}{4\alpha(t-t')} + \frac{(y-v_y t')^2}{4\alpha(t-t')} + \frac{z^2}{4\alpha(t-t')}\right)\right)$$

<div align="center">**Equation 4-2**</div>

The first step of finding the temperature field is the establishment of a heat source model. In the LDED-PF process, there are two different sources of energy. One is the coming energy from the laser beam dQ_l and the other one is the heated powder flux dQ_p. It should be mentioned that the attenuation of the laser beam by the powder stream can be assumed negligible [18]. These two sources of energy are added and treated as a bulk heat source to satisfy the total energy balance of the process [8,99].

$$dQ_t = dQ_l + dQ_p$$

<div align="center">**Equation 4-3**</div>

Assuming that the interaction of these two heat sources is small and negligible, then the two temperature contributions caused by the laser-beam and heated powder flux can be added up, and the total process temperature field is composed of the temperature fields caused by two of them. Considering two separate sources of energy in the lumped model, the temperature contribution of the laser beam and heated powder flux can calculated separately and the solution to the differential equation of heat conduction is as follows.

$$dT = \frac{(dQ_l + dQ_p)dt'}{4\rho c\left(\pi\alpha(t-t')\right)^{3/2}} exp\left(-\left(\frac{(x-v_x t')^2}{4\alpha(t-t')} + \frac{(y-v_y t')^2}{4\alpha(t-t')} + \frac{z^2}{4\alpha(t-t')}\right)\right)$$

$$= \frac{dQ_l dt'}{4\rho c\left(\pi\alpha(t-t')\right)^{3/2}} exp\left(-\left(\frac{(x-v_x t')^2}{4\alpha(t-t')} + \frac{(y-v_y t')^2}{4\alpha(t-t')} + \frac{z^2}{4\alpha(t-t')}\right)\right)$$

$$+ \frac{dQ_p dt'}{4\rho c\left(\pi\alpha(t-t')\right)^{3/2}} exp\left(-\left(\frac{(x-v_x t')^2}{4\alpha(t-t')} + \frac{(y-v_y t')^2}{4\alpha(t-t')} + \frac{z^2}{4\alpha(t-t')}\right)\right)$$

$$= dT_l + dT_p$$

<div align="center">**Equation 4-4**</div>
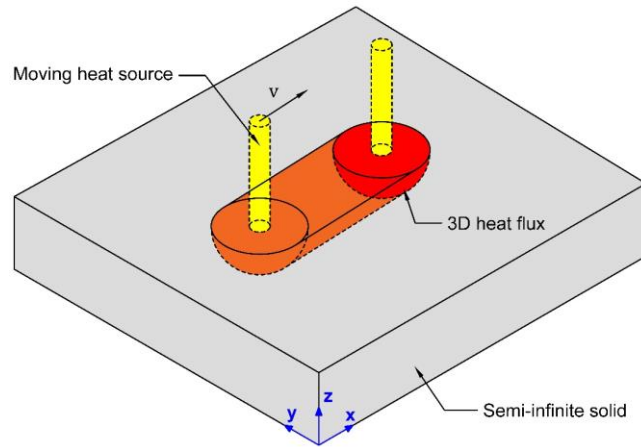
Figure 4-1. Schema for a heat source moving on a semi-infinite solid in the global coordinate system.

For the laser beam heat source Q_l, three different models are considered in this work known as point heat source (1D), circular surface heat source (2D), and semi-spherical volumetric heat source (3D). The schematic representation of the geometrical laser-beam heat sources used in this study is shown in Figure 4-2.
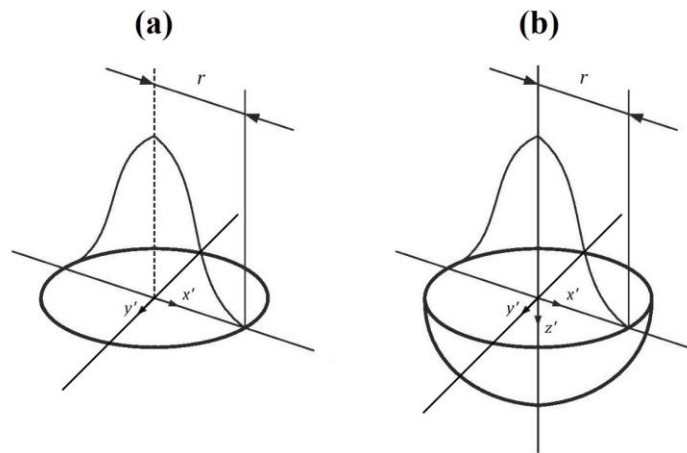
Figure 4-2. Schema for laser-beam heat source models; (a) circular 2D Gaussian; (b) semi-spherical 3D Gaussian.

For a point heat source, the power P of the heat source in Watt can be related to the point heat source δQ_l. The temperature field caused by this heat source $T_l(x, y, z, t)$ at time t at the point of interest (x, y, z) has been well established as [100]:

$$T_l(x,y,z,t) - T_0 = \int_0^t \frac{\beta P}{4\rho c\left(\pi\alpha(t-t')\right)^{3/2}} exp\left(-\left(\frac{(x-v_xt')^2}{4\alpha(t-t')} + \frac{\left(y-v_yt'\right)^2}{4\alpha(t-t')} + \frac{z^2}{4\alpha(t-t')}\right)\right) dt'$$

<div align="center">Equation 4-5</div>

where β denotes the laser-material absorptivity, α denotes the thermal diffusivity. It should be mentioned that the convective and radiative heat losses are absent in the above-mentioned solution since the heat transfer by conduction can be assumed dominant [101].

Based on the above-mentioned solution, the temperature field for other geometrical heat sources can be obtained by carrying out the corresponding surface or volume integration of the heat source in a superposition moving coordinate system (x',y',z'). For a surface heat source with heat density $Q_l(x',y')$, the temperature field in the semi-infinite body would be adopted as:

$$T_l(x,y,z,t) - T_0$$

$$= \int_0^t \left\{ \int_{-\infty}^\infty \int_{-\infty}^\infty \frac{Q_l(x',y')}{4\rho c\left(\pi\alpha(t-t')\right)^{3/2}} exp\left(-\left(\frac{(x-v_xt'-x')^2}{4\alpha(t-t')} + \frac{\left(y-v_yt'-y'\right)^2}{4\alpha(t-t')}\right.\right.\right.$$

$$\left.\left.\left. + \frac{z^2}{4\alpha(t-t')}\right)\right) dx'dy' \right\} dt'$$

<div align="center">Equation 4-6</div>

For a laser beam with TEM$_{00}$ mode in which heat density has a Gaussian distribution throughout the surface, the 2D heat density $Q_l(x',y')$ within the circular area with radius r is given as [17]:

$$Q_l(x',y') = \frac{2\beta P}{\pi r^2} exp\left(-\frac{2(x'^2+y'^2)}{r^2}\right)$$

<div align="center">Equation 4-7</div>

The further simplification was derived by Huang et al. [19] as:

$$T_l(x, y, z, t) - T_0$$

$$= \int_0^t \frac{2\beta P}{\rho c \pi \sqrt{\pi \alpha(t - t')}(r^2 + 8\alpha(t - t'))} exp\left(-\left(\frac{2(x - v_x t')^2}{r^2 + 8\alpha(t - t')}\right.\right.$$

$$\left.\left.+ \frac{2(y - v_y t')^2}{r^2 + 8\alpha(t - t')} + \frac{z^2}{4\alpha(t - t')}\right)\right) dt'$$

Equation 4-8

For a volumetric heat source with heat density $Q_l(x', y', z')$, the temperature field in a semi-infinite body would be adopted as:

$$T_l(x, y, z, t) - T_0$$

$$= \int_0^t \left\{ \int_0^\infty \int_{-\infty}^\infty \int_{-\infty}^\infty \frac{Q_l(x', y', z')}{4\rho c (\pi \alpha(t - t'))^{3/2}} exp\left(-\left(\frac{(x - v_x t' - x')^2}{4\alpha(t - t')} + \frac{(y - v_y t' - y')^2}{4\alpha(t - t')}\right.\right.\right.$$

$$\left.\left.\left.+ \frac{(z - z')^2}{4\alpha(t - t')}\right)\right) dx' dy' dz' \right\} dt'$$

Equation 4-9

For a laser-beam heat source with a Gaussian distribution throughout the volume, the 3D heat density $Q_l(x', y', z')$ at point (x', y', z') within the semi-sphere with radius r is given as [17]:

$$Q_l(x', y', z') = \frac{2^{5/2}\beta P}{\pi^{3/2} r^3} exp\left(-\frac{2(x'^2 + y'^2 + z'^2)}{r^2}\right)$$

Equation 4-10

The above equations can be further simplified, as shown below.

$$T_l(x, y, z, t) - T_0$$

$$= \int_0^t \frac{2^{5/2}\beta P}{\rho c \pi^{3/2}(r^2 + 8\alpha(t - t'))^{3/2}} exp\left(-\left(\frac{2(x - v_x t')^2}{r^2 + 8\alpha(t - t')} + \frac{2(y - v_y t')^2}{r^2 + 8\alpha(t - t')}\right.\right.$$

$$\left.\left.+ \frac{2z^2}{r^2 + 8\alpha(t - t')}\right)\right) dt'$$

48

Equation 4-11

For the heated powder flux Q_p, a flux of 2D distributed powder in a circular area is considered. As powder particles fall onto the melt pool, they draw energy to increase their enthalpy. The enthalpy exchange of the particles is assumed as a local surface process [37], and it can be expressed as follows as proposed by Huang et al. [18,19]:

$$Q_p = c_p v_p \gamma (T_m - T_0)$$

Equation 4-12

where c_p denotes the specific heat capacity of a particle, v_p denotes the particle velocity, γ denotes the powder spatial mass concentration, T_m denotes the melting temperature, and T_0 denotes the room temperature. For the heated powder flux with a 2D Gaussian distribution, previous literature suggests that an exponential distribution can describe the powder stream Gauss concentration under a coaxial nozzle [102]. The powder concentration $\gamma(x', y')$ caused by powder feed rate F within a circular area with radius r is given by the following equation [102]:

$$\gamma(x', y') = \frac{F}{v_p \pi r^2} exp\left(-\frac{(x'^2 + y'^2)}{r^2}\right)$$

Equation 4-13

The temperature field caused by this heated powder flux $T_p(x, y, z, t)$ at time t at the point of interest (x, y, z) in the semi-infinite body would be adopted as follows based on the derivation method proposed by Huang et al. [19]:

$$
\begin{aligned}
T_p(x, y, z, t) - T_0 \\
= \int_0^t \frac{Fc_p(T_m - T_0)}{\rho c \pi \sqrt{\pi \alpha(t - t')}(r^2 + 4\alpha(t - t'))} exp\left(-\left(\frac{(x - v_x t')^2}{r^2 + 4\alpha(t - t')}\right.\right. \\
\left.\left. + \frac{(y - v_y t')^2}{r^2 + 4\alpha(t - t')} + \frac{z^2}{4\alpha(t - t')}\right)\right) dt'
\end{aligned}
$$

Equation 4-14

4.2.2 Melt-pool/deposit Dimensions

For single-track deposition, the melt pool/deposit dimensions can be estimated according to the liquid-solid isotherms defined by the transient temperature field. Accordingly, the track width/length is assumed to be equal to the melt pool width/length. The track bead height can be derived based on the uniformity of powder flow density over the melt pool projection area on the x-y plane [18]. The maximum height of the track bead H can be estimated as:

$$H = \frac{WF}{\pi \rho_p v r_{ps}^2}$$

Equation 4-15

where W is melt pool width, F is powder feed rate, ρ_p is the density of powder material, r_{ps} is the effective radius of the powder-stream column on the substrate. The bead height curvature can be defined based on the polynomial curve fitting to the data points of the width and maximum height.

4.2.3 Material Properties

To improve the model fidelity, some simplified factors are considered for the material properties. The thermophysical properties of the materials are assumed to be temperature-independent and they are averaged out over the range of room temperature to melting temperature. The effect of mixing the track bead and substrate or dilution ratio to the thermophysical properties of the melt pool takes into consideration by assuming an average dilution of 25%. The effect of melt pool convection is compensated by an enhanced thermal diffusivity, which can typically be taken as 1 to 4 times greater than that of the solid-state, depending on the processing parameters [88–90].

$$\alpha^* = \mu \alpha, \quad T > T_m$$

Equation 4-16

where μ is a correction factor for enhanced thermal diffusivity. The effect of the latent heat L_f in melting/solidification cycles is also considered with increasing the specific heat as:

$$c_p{}^* = \frac{L_f}{T_m - T_0} + c_p$$

Equation 4-17

50

The effect of an inclined surface caused by the deposition bead on the laser-material absorption is presented by the enhanced absorptivity related to the angle of incidence. The absorptivity of an inclined surface in the polarization plane is given as [91]:

$$\beta(\varphi) = \frac{4n_r cos\varphi}{(n_r cos\varphi + 1)^2 + k_e^2 cos^2\varphi}$$

Equation 4-18

where φ is the inclination angle in radians, n_r is refraction index, and k_e is the extinction index of the material. If the cross-section of the deposit is assumed to be a segment of a circle, the inclination angle is approximated as:

$$\varphi = \tan^{-1}\left(\frac{2H}{W}\right) = \tan^{-1}\left(\frac{2F}{\pi\rho_p v r_{ps}^2}\right)$$

Equation 4-19

In order to improve the model fidelity, some complicated material-dependent factors must be calibrated to minimize the error between the experimental and predicted data. An analytical approach of utilizing normalized enthalpy has been previously used to relate melt pool dimensions to the processing parameters in laser welding [94,95] and laser additive manufacturing [96,97]. Zhang et al. [17] showed that there is a linear dependency between the normalized enthalpy and normalized melt pool depth, where the enthalpy ΔH is the energy absorbed during the dwell time ($\tau = 2r/v$) over the heat diffusion volume. The heat diffusion volume for 1D heat flow is expressed as $\pi r^2 \sqrt{\alpha\tau}$. Therefore, the absorbed energy density is derived as follows to be proportional to the ratio of the laser power to the root of scanning speed:

$$\Delta H = \frac{\beta P\tau}{\pi r^2 \sqrt{\alpha\tau}} = C\frac{P}{\sqrt{v}}$$

Equation 4-20

For improving the model accuracy and based on the above-mentioned rationale, two of the material-dependent factors, including the correction factor for enhanced thermal diffusivity, and heat source radius, are assumed to be proportional to $P/\sqrt{v}$ as simple linear algebraic equation as $a\,(P/\sqrt{v}) + b$.

51

4.3 Experimental Procedures

Feedstock powder and substrate materials were plasma-atomized Ti-5Al-5V-5Mo-3Cr (Ti-5553) powder (AP&C, GE Additive) and plates of Ti-6Al-4V (Ti-64) alloy, respectively. The powder has a spherical shape with particle sizes ranged from 45 to 106 μm. Experiments were carried out by an LDED-PF machine (IC106, DM3D Technology) equipped with a disk laser (TruDisk 2000, TRUMPF) in an atmosphere-controlled chamber. The oxygen level was kept below 10 ppm during the depositions. The thermophysical properties of the materials at room/melting temperature are presented in Table 4-1.

Table 4-1. Thermophysical properties of the materials

Material	Melting Temperature [K]	Density [g/cm^3]	Thermal conductivity [W/m·K]	Specific heat [J/(g·K)]	Ref.
Ti-5553	1923	4.65 (@298 K)-4.2 (@1923 K)	5 (@298 K)-29 (@1923 K)	0.51 (@298 K)-0.8 (@1923 K)	[103]
Ti-64	1928	4.42 (@298 K)-3.92 (@1928 K)	4.4 (@298 K)-33.4 (@1928 K)	0.546 (@298 K)-0.83 (@1928 K)	[104]

For validation tests, single-track depositions at different laser powers, scanning speeds, and powder feed rates were experimentally designed based on a central composite design. Each group experiment was repeated three times. In total, 45 tracks were deposited. Some of the processing parameters are listed in Table 4-2. The nozzle standoff distance was set to 10 mm. The laser beam spot size was measured as 1.4 mm at the standoff distance. The powder carrier gas flow rate (Argon) was set to 4 L/min. The powder hopper cover gas flow rate (Argon) was set to 8 L/min. The Nozzle gas flow rate was set to 6 and 4 L/min for Argon and Helium, respectively. The nozzle shaping gas flow rate (Argon) was set to 6 L/min. Figure 4-3 shows the depositions layout. All the single-tracks were metallographically prepared for microscopic examination. The geometrical features of the melt pool were experimentally measured from the microscopic images. Laser scanning confocal microscopy (VK-X250, Keyence) was used to examine the single-track dimensions. The microscopy of the transverse cross-section was used to measure the height, width, and dilution of the melt pool. An example of such measurements is presented in Figure 4-7. The length of the melt pool was measured from the top-view images. The melt pool shape at the end of each track is evident from the banding effect. An example of such measurement is presented in Figure 4-5a. The laser was shut off 1 sec before

the endpoint of the scanning path in order to avoid the effect of robot arm deceleration on the length of the melt pool.

Table 4-2. Technical and processing parameters of LDED-PF

Processing parameter set	Laser power (W)	Scanning speed (mm/s)	Powder feed rate (g/min)
1	800	8	8
2	400	14	8
3	600	16	6
4	600	6	6
5	800	14	4
6	800	8	4
7	400	8	4
8	600	11	6
9	600	11	2.6
10	800	14	8
11	400	8	8
12	264	11	6
13	400	14	4
14	936	11	6
15	600	11	9.4
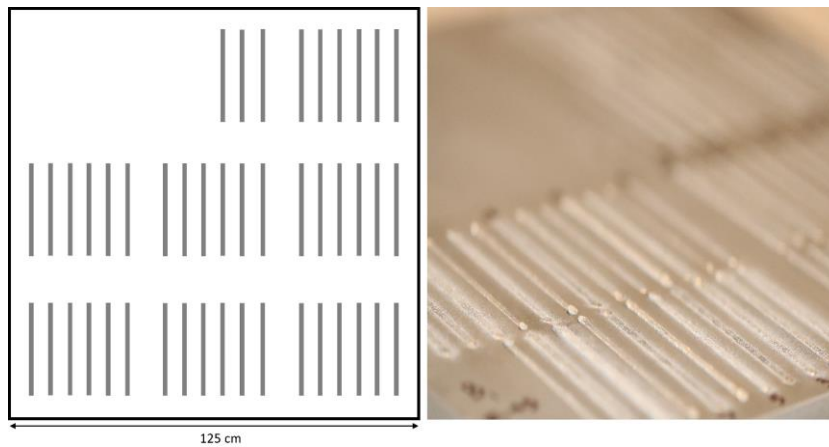
Figure 4-3. A layout of all single tracks on the substrate.

In order to capture the powder stream profile, a Canon EOS REBEL T7i60D camera equipped with a Canon EF 100 mm F/2.8 Macro USM Lens was used. Luminance analysis was used by the gray-value tool of ImageJ software. The simulations of the thermal field and deposition geometry were programmed in Matlab® R2019a, and a DELL® computer with Intel® CoreTM i7-7700 CPU 3.6 GHz was used to run the program. The integral calculation was programmed using trapezoidal numerical integration method.

4.4 Results and Discussion

4.4.1 Powder Concentration

Photo-optical luminance analysis was used for investigating the powder concentration. The capability of this method for this purpose has been proved by Pinkerton and Li [30]. Figure 4-4 shows the gray-value image of the powder stream profile together with the normalized gray-value intensity in the transverse direction, as representative of powder distribution at different standoff distances.
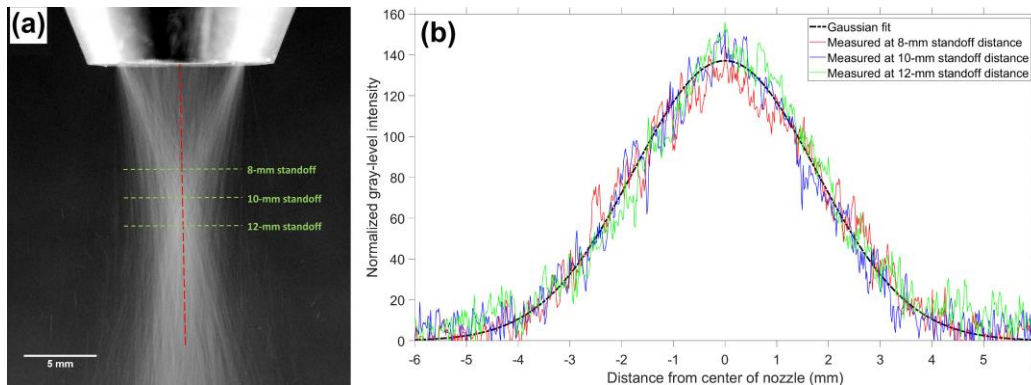
Figure 4-4. (a) Gray-value image of the powder stream profile of the coaxial nozzle. (b) Measured gray-value intensity at different standoff distances together with model-predicted Gaussian fit.

From the results, the powder stream has a Gaussian distribution pattern, and the intensity within the range from 8 to 12 mm is relatively similar. Thus, the focal position of the powder stream can be approximately in this range. The nozzle standoff distance from the substrate was set at 10 mm (in the middle of the focal position range) and hence the attenuation length would be 2 mm. The powder particles come out of the annular outlet at different angles and converge in the focal position range. The average converge angle is 70 degrees and the maximum powder concentration happens within the focal position range. The model-predicted Gaussian fit is also shown in Figure 4-4b as a black dashed line.

This verifies that the mathematical representation of the Gaussian distribution of the powder stream in Equation 4-13 perfectly matches the experimental data. The effective radius of the powder stream is found to be 2.5 mm.

4.4.2 Heat-source Model Comparisons

As the temperature field has a strong impact on the microstructure [54] and induced residual stresses [105], it is important for any model development to assure a realistic prediction of the temperature field. Two comparison criteria are used for source model comparisons. Temperature field modeling was performed, as the first comparison criterion, for the three heat sources (point, circular, and semi-spherical). The thermophysical properties and processing parameters were kept constant such that the heat source model is the only factor to reflect the difference in the prediction. The heat source radius and enhanced thermal diffusivity were also kept constant. Figure 4-5 shows the predictions of the transient thermal cycle of different interest points and peak temperature along the single-track based on different heat source models. The change in thermal cycle patterns along the single-track is clearly shown. The peak temperature along the single-track is converging to a value and reaches a peak level. For the 1D heat source, the temperature goes up to almost 6500 K, which induces a very high and unrealistic temperature gradient within the melt pool. For the 2D and 3D heat sources, the prediction is more or less the same. The temperature goes up to almost 3500 K, which is acceptable to the titanium material with a boiling point of around 3500 K. The temperature distribution/gradient in the melt pool based on the 2D and 3D heat sources seem to be more realistic in comparison to the 1D heat source.

The predicted melt pool/deposit dimensions are also compared to the experimental data as the second comparison criterion. Figure 4-6 compares the experimental and predicted results for the melt pool/deposit dimensions. All the thermophysical properties and processing parameters were kept constant for this comparison. For the melt pool length/width and deposit height, all the predicted results, based on the three heat source models, fall within the experimental variation range. The prediction error for the width, length, and height is 7, 4, and 4%, respectively. However, for the melt pool penetration in the substrate (dilution), only the predicted result from the 2D heat source model falls within the range, and both the 1D and 3D heat source models are out of the range with 35% error.
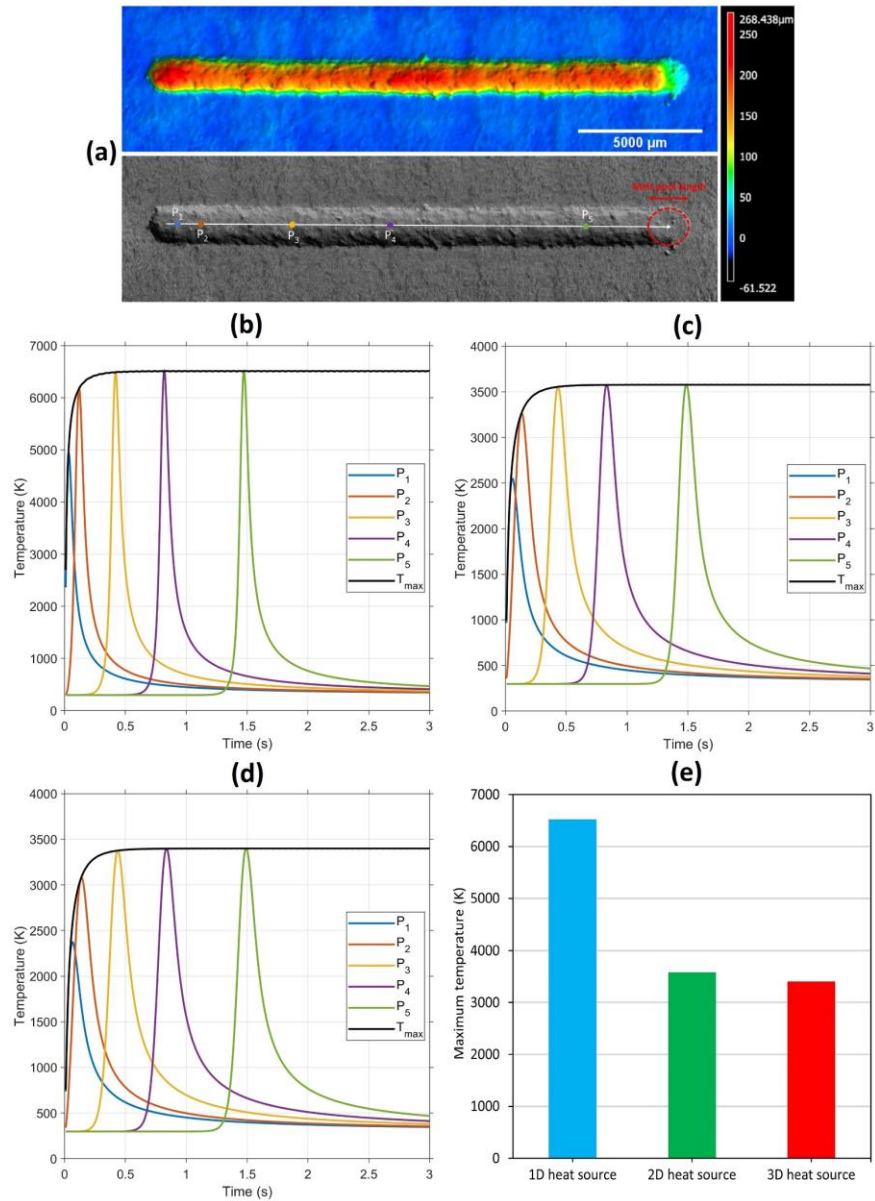
Figure 4-5. (a) Top view of the track (*P*=600 W, *F*=6 g/min and *v*=11 mm/s) showing schematic positions of interest points along the track. Transient thermal cycle of different interest points and peak temperature (black solid line) based on (b) 1D point heat source, (c) circular 2D Gaussian heat source, and (d) semi-spherical 3D Gaussian heat source. (e) Maximum predicted temperature by different heat sources when reaches a peak level.

The use of the 1D heat source model predicts a high penetration in the substrate since the heat conduction caused by a point heat source has the same magnitude in the x, y, and z-axis, resulting in a hemisphere-shape melt pool. The use of the 1D heat source model also leads to unrealistically high

56

temperatures and invalid temperature gradients. The 3D heat source model predicts a high penetration since the model considers a depth for the heat source itself, which is added up to the penetration depth caused by heat conduction. On contrary, the 2D heat source model provides the smallest depth owing to the fact that this model assumes the laser-material interaction as a local surface process and the melt pool penetration is only defined by heat conduction of a surface heat source. The choice of the heat source model depends on the dominant physics of the process which leads to two different modes of heat transfer in the melt pool i.e. conduction-mode and keyhole-mode. Heat transfer through conduction is dominant in conduction-mode melting; however, excessive laser beam penetration and strong heat convection majorly contribute to the heat transfer in keyhole-mode melting. The 3D models are more accurate for the processes with keyhole-mode melting. Considering the ability of the heat source models to predict both melt pool temperature field and dimensions, the 2D heat source model is adequate for LDED-PF. The LDED-PF process, owing to its underlying physics, falls within the conduction-mode processes and the keyhole barely happens in this process under extreme processing conditions. Hence, the 2D heat source is closer to the physics of the local surface laser-material interaction in the LDED-PF process. The assumption of volumetric heat sources seems to be adequate for an AM process such as powder bed fusion which is mainly in keyhole mode with excessive penetration of heat source into the material [17].
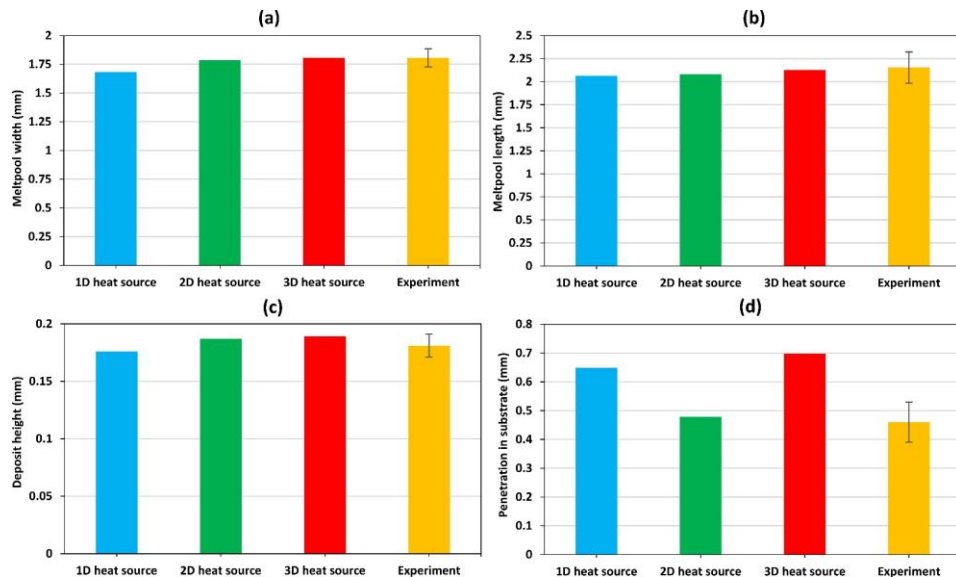
Figure 4-6. Comparison of the heat source models (P=600 W, F=6 g/min and v=11 mm/s); (a) melt pool width, (b) melt pool length, (c) deposit height, and (d) penetration in substrate (dilution).

57

4.4.3 Melt-pool/deposit Dimensions

For the model validation, the prediction of melt pool/deposit dimensions was performed for a wide range of processing parameters listed in Table 4-2 and compared with the experimental data. Figure 4-7 shows an example of the cross-sectional measurements for a single-track.
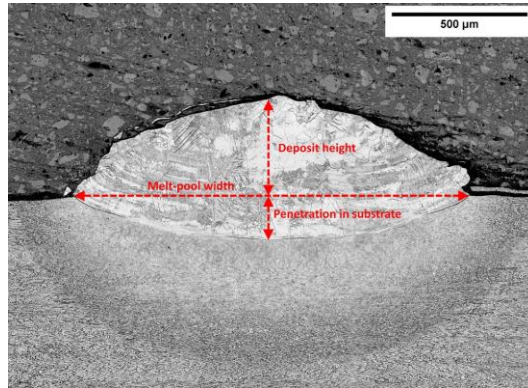
Figure 4-7. Transverse cross-section of the deposit (P=600 W, F=9.4 g/min and v_x=11 mm/s).

Experimental measurements of melt pool width were used to calibrate the 2D heat source model. The heat source size changes by the processing parameters. The assumption of a fixed heat source size results in the divergence of the predicted results from the experimental ones. In the model development, the effective heat source is assumed to have more or less the same area as the melt pool projection on the x-y plane. This means that the effective diameter of the heat source can be assumed to be equal to the melt pool width. Figure 4-8 shows the half-width of the melt pool (effective radius of the heat source) as a function of $P/\sqrt{v}$. The linear relation is obvious, which supports the assumption presented in Equation 4-20.
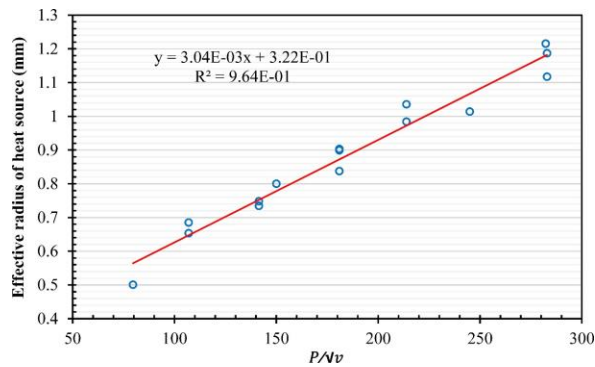
Figure 4-8. Effective radius of the heat source as a function of $P/\sqrt{v}$.

Another factor to be calibrated is the coefficient of enhanced thermal diffusivity. This has to be done to compensate for the effect of melt pool convection. The coefficient of enhanced thermal diffusivity for each set of processing parameters was obtained by matching the predicted results with the experimental results to minimize the error through iteration in Matlab® R2019a. The calibrated coefficient of enhanced thermal diffusivity is shown in Figure 4-9 as a function of $P/\sqrt{v}$. Instead of using fixed values for the heat source radius and the enhanced thermal diffusivity, they can be formulated in the form of linear equations of $a\,(P/\sqrt{v}) + b$ for all range of the processing parameters. The empirical coefficients for the obtained linear equations are presented in Table 4-3.
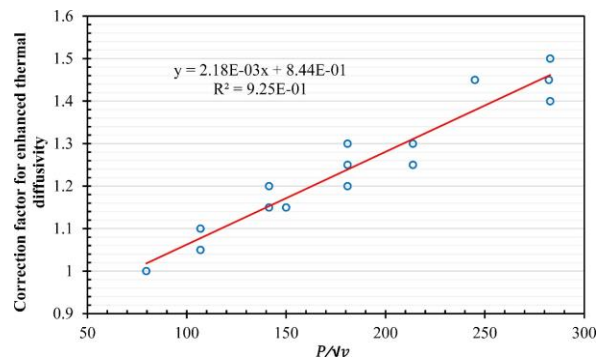
Figure 4-9. Coefficient of enhanced thermal diffusivity as a function of $P/\sqrt{v}$.

Table 4-3. Coefficients in the linear algebraic equation as $a\,(P/\sqrt{v}) + b$ for effective heat source radius and enhanced thermal diffusivity

Quantity	a	b	R
Heat source radius (mm)	3.04E-03	3.22E-01	0.96
Coefficient of enhanced thermal diffusivity	2.18E-03	8.44E-01	0.92

Figure 4-10 compares the predicted results of the calibrated model with the experimental data for all processing parameter sets. The results are in close agreement with each other. The errors for all the melt pool/deposit dimensions are below 8%. The existing error may come from the error in measurements or the minor physical phenomena that are absent in the model. For example, convective and radiative heat transfers are ignored, and heat conduction is considered the only mechanism of heat transfer in the melt pool. Additionally, the melt pool size/shape may be affected by the fluid dynamics of the melt pool. The role of such phenomena cannot be calculated by heat conduction models.

However, heat conduction calculations suffice the needful accuracy for prediction and qualitative assessment of LDED-PF.
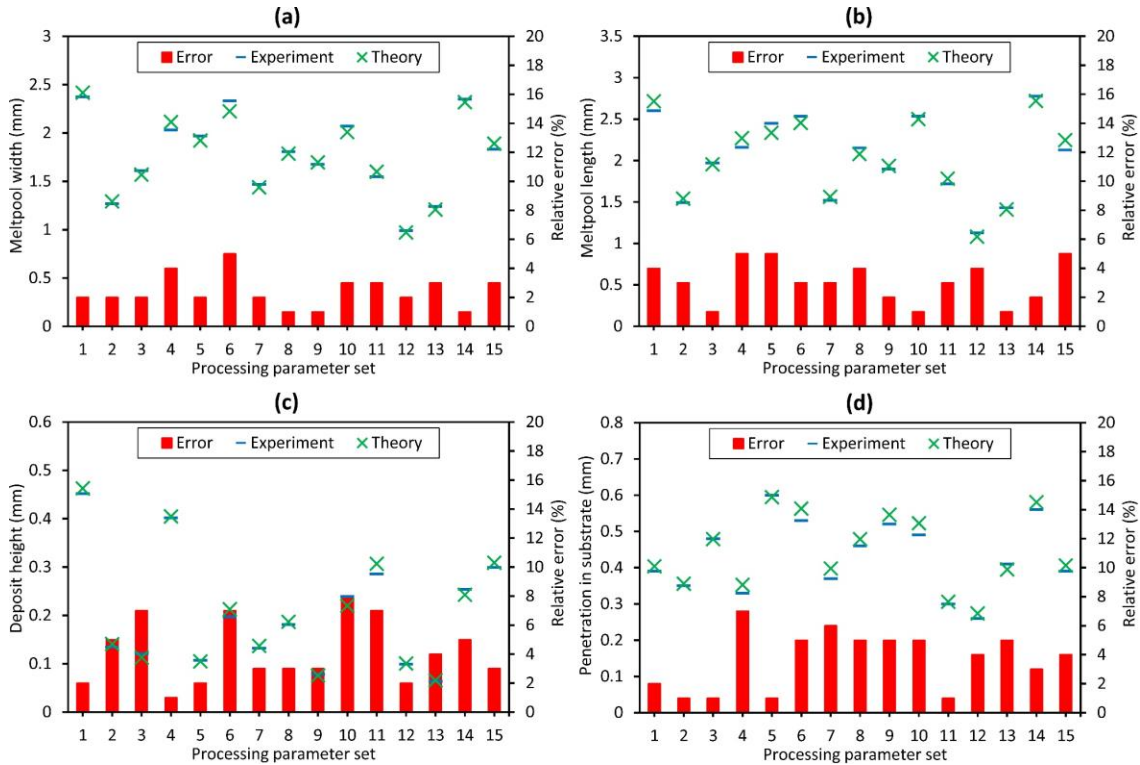
Figure 4-10. Comparison of the predicted and experimental results of melt pool/deposit dimensions for all processing parameter sets, (a) melt pool width, (b) melt pool length, (c) deposit height, and (d) penetration in the substrate (dilution).

4.4.4 Temperature Field Simulation

It is challenging to experimentally measure the precise temperature field due to the temperature measurement dependencies on nonlinear emissivity. The analytical model, as an efficient approach, can be used for simulating the temperature field in the LDED-PF process. The simulation of the melt pool temperature field based on the calibrated model is shown in Figure 4-11. The melt pool/deposit temperature and the temperature distribution within the substrate can be easily simulated with good accuracy. The average computational time of simulation for each processing parameter set was recorded as 20 sec with the x/y increment of 0.1 mm, the z increment of 0.01 mm, and the integration time interval of 0.005 sec.
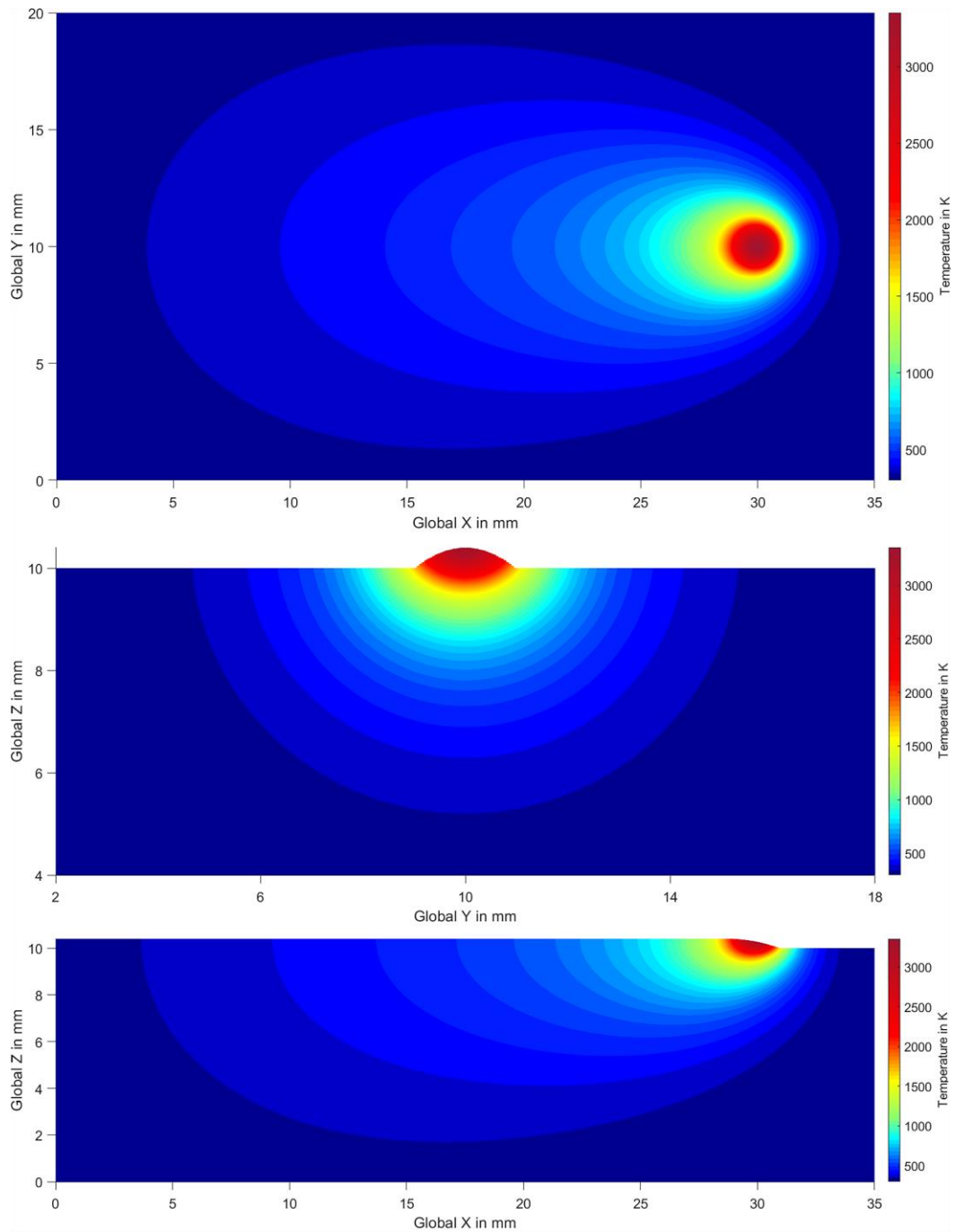
Figure 4-11. Temperature field in different planes implemented in Matlab® R2019a. From the top to the bottom, x-y plane (substrate surface), y-z plane (transverse cross-section), and x-z plane (longitudinal cross-section), respectively (P=600 W, F=6 g/min and v_x=6 mm/s).

Figure 4-12b shows the predictions of the transient thermal cycle of the different interest points based on the calibrated model where the heat source is located at the track bead top. The change in thermal cycle patterns is clearly observable. The temperature keeps decreasing as the interest point becomes farther and farther away from the heat source, which shows the heat dissipation during the process. Figure 4-12c shows the heating/cooling rates of the different interest points. At a constant processing parameter set, the heating/cooling rates increases as the interest point becomes closer and closer to the heat source at the track bead top. The average computational time of these predictions for each processing parameter set was recorded as 4.2 sec with the x/y increment of 0.1 mm, the z increment of 0.15 mm, and the integration time interval of 0.005 sec.
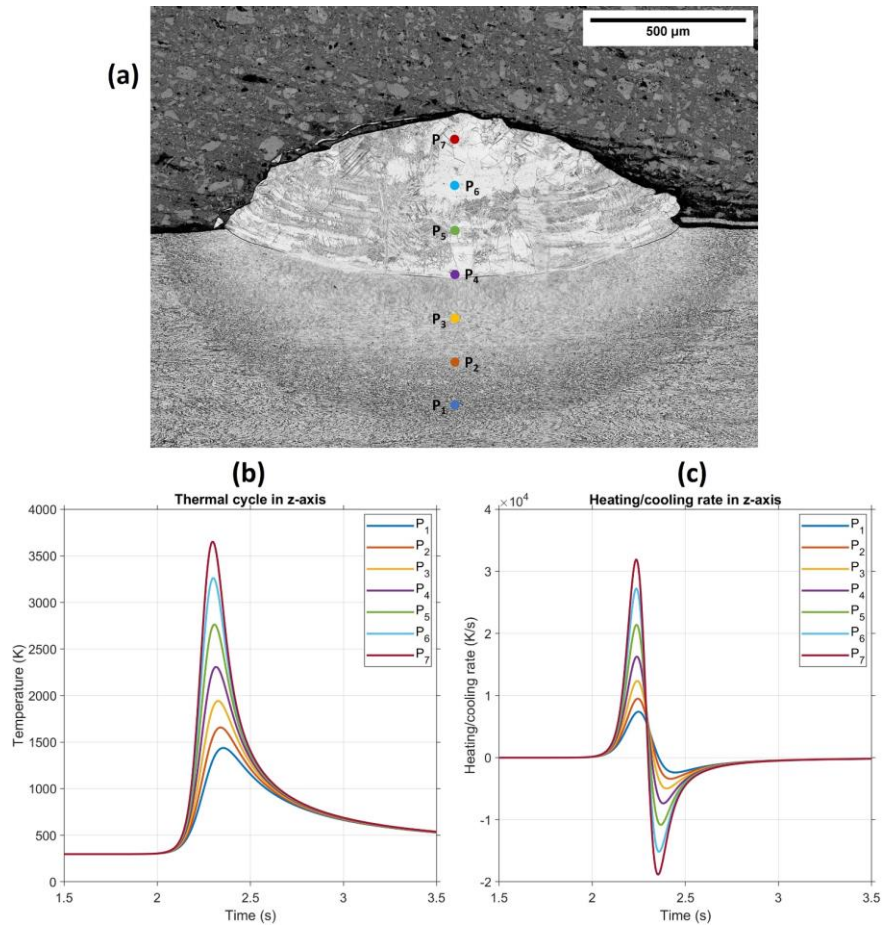
Figure 4-12. (a) Cross-sectional view of the deposit (P=600 W, F=9.4 g/min and v_x=11 mm/s) showing schematic positions of interest points. (b) Transient thermal cycle and (c) heating/cooling rate of different interest points based on the calibrated 2D heat source.

62

4.4.5 Model Sensitivity

The sensitivity of the model to input parameters such as processing parameters and thermophysical properties of material was investigated by varying input values and tracking their effect on the melt pool width prediction. Table 4-4 shows the mean values together with the values of ±50% variation for each parameter. First, all the mean values were used to predict the melt pool width. Second, in every single calculation, only one parameter alteration to ±50% value was performed, and the melt pool width was predicted at the half-track length. The difference between the melt pool width prediction using each parameter alteration and mean values was recorded in percentage and plotted in radar charts in Figure 4-13.

<p align="center">Table 4-4. Parameters and their values for sensitivity analysis</p>

Parameter	-50%	Mean	+50%
Laser power (W)	300	600	900
Scanning speed (mm/s)	5.5	11	16.5
Powder feed rate (g/min)	3	6	9
Heat source radius (mm)	0.436	0.872	1.308
Laser absorptivity	0.258	0.516	0.774
Density (g/mm^3)	0.0022	0.0043	0.0065
Specific heat capacity (J/gK)	0.423	0.847	1.27
Thermal conductivity (W/mmK)	0.009	0.018	0.027
Coefficient of enhanced thermal diffusivity	0.619	1.238	1.857

The effect of processing parameters was investigated separately since there is an interconnection between the processing parameters and two calibrated factors as the coefficient of enhanced thermal diffusivity and heat source radius. As shown in Figure 4-13, among the main processing parameters, laser power has a strong influence, scanning speed has a medium influence, and powder feed rate has a weak influence on the melt pool width prediction. Among the thermophysical properties of the material, heat source radius has a weak influence, density and specific heat capacity have a medium influence, and thermal conductivity and laser absorptivity have a strong influence on the melt pool width prediction.
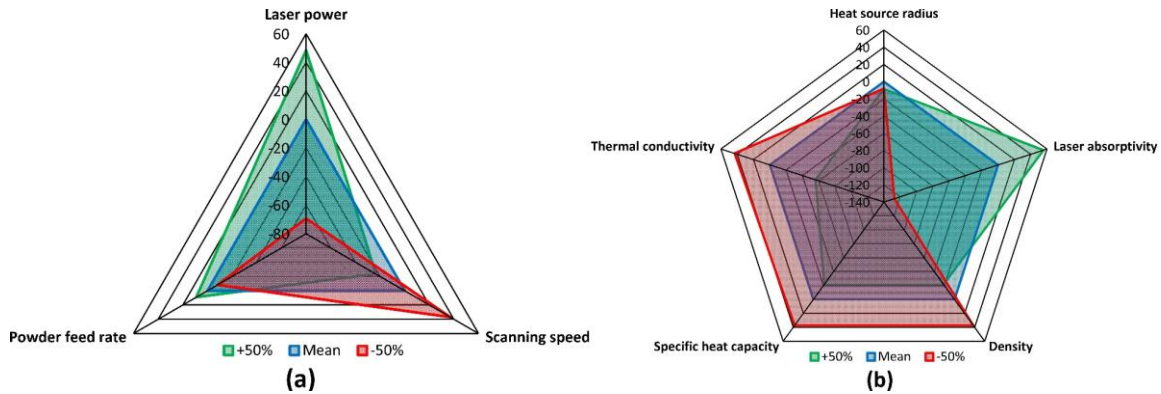
Figure 4-13. Sensitivity analysis for (a) processing parameters and (b) thermophysical properties of the material, showing their effect on the melt pool width prediction.

4.5 Summary

The energy distribution is a crucial factor in the LDED-PF process for modeling the laser-material interaction. In this chapter, analytical solutions were introduced for three different laser-beam heat source models known as a point (1D) heat source, circular (2D) heat source, and semi-spherical (3D) heat source in order to predict the transient temperature field in the LDED-PF process. To validate the heat source models, the temperature field in the single-track deposition of Ti-5553 was modeled. The melt pool dimensions were investigated and compared with the predicted ones. The prediction of the melt pool dimensions based on the surface (2D) heat source was in close agreement with the experimental data. However, the point (1D) heat source and semi-spherical (3D) heat source resulted in either wrong prediction of melt pool dimensions or unrealistic temperature distribution. The developed model was calibrated for Ti-5553 single-tracks at different processing parameter sets. The expressions of the coefficient of enhanced thermal diffusivity and heat source size were found to be linear algebraic equations as $a\left(P/\sqrt{v}\right) + b$. After the model calibration, good agreement between the predicted results and the experimental data was observed. The relative error was below 8%. Sensitivity analysis identified the most influential parameters in the model. Those parameters must be carefully selected and play an important role in the final prediction. In addition, the analytical solution showed high efficiency in terms of computational time. With the benefits of high prediction accuracy and time efficiency, the developed model can be effectively used for purposes such as controlling the deposition dimensions and microstructure in LDED-PF.

Chapter 5: Correlation of Process with Deposition Dimensions and Solidification Microstructure in Multi-track LDED-PF

5.1 Introduction

Besides the processing parameters, the scanning strategy has a major contribution to the transient temperature field and consequently the profile of overlapping tracks, deposition efficiency, and solidification characteristics. Components of the same geometry can be designed in CAD/CAM software with different scanning strategies. However, the deposition path of different strategies complicates the prediction of the temperature field and the profile of overlapping beads. The thermal cycles and solidification characteristics produced in multi-track deposition are complex and often spatially varied for each track. To understand the significance of the scanning strategy, it is necessary to understand the evolution of the temperature field and solidification characteristics in multi-track deposition. In the present study, four scanning strategies are investigated for LDED-PF of cuboidal geometries: bidirectional scan, unidirectional scan, inward spiral, and S-pattern. 2D thermal models of LDED-PF are developed to provide an improved understanding of the effect of the different scanning strategies on the transient temperature field, the geometrical profile of overlapping tracks, and the corresponding solidification characteristics during multi-track deposition. The model provides a time-efficient platform for rapid prediction of geometrical and microstructural features of the multi-tracks. As another contribution of this work, a new universal algorithm, based on parabolic functions, is developed to estimate the geometrical profile of the overlapping beads. The model applies to all scanning strategies and it can act as a rapid tool to predict the solidification characteristics.

5.2 Model Formulation

5.2.1 Transient Temperature Field

In LDED-PF, a solid component is built by depositing tracks, side by side and layer by layer according to the build-up strategy. The deposition nozzle moves with a linear speed of v_i along the x-axis or y-axis to apply adjacent tracks with an overlap ratio defined by a step-over distance h_s, then it moves according to a specific distance in the z-axis to apply the next layer on top of the previous layer. Different scanning strategies are possible for multi-track deposition such as unidirectional/bidirectional

scanning, and inward/outward spiral. The bidirectional and unidirectional strategies are direction-parallel, while inward and outward spirals are contour-parallel. The most common scanning strategy in LDED-PF is direction-parallel since the generation requires simple planning algorithms and it can be applied to print a wide range of solid structures [106]. The S-pattern is a novel strategy that has been recently reported to reduce residual stress and it is still at the primary stage [107]. The four scanning strategies, shown in Figure 5-1, are considered in this study. The solid arrows in the figure show the direction of the laser movement and the solid circles show the positions at which the laser turns on/off in each scanning strategy. In discontinuous strategies such as unidirectional, the definition of individual tracks is based on the laser turns on/off positions. In continuous strategies such as bidirectional, spiral, and S-pattern, individual tracks are defined based on the change in the direction of the laser movement.
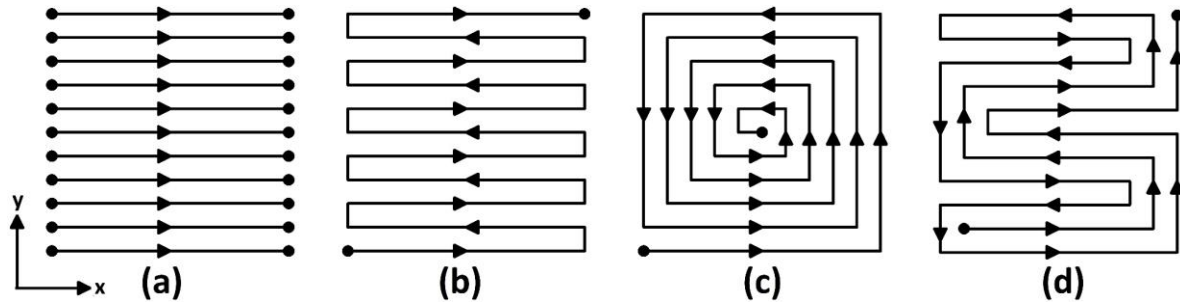
Figure 5-1. Schema of four scanning strategies; (a) unidirectional, (b) bidirectional, (c) inward spiral, and (d) S-pattern.

As for the first step of modeling, the temperature field $T(x, y, z, t)$ at time t at the point of interest (x, y, z) caused by a moving 2D Gaussian heat source acting instantaneously at the time t' in a semi-infinite body was developed by the authors for single-track LDED-PF. The details of derivation are available in Ref. [108].

$$T(x, y, z, t) - T_0$$

$$= \int_0^t \frac{2\beta P}{\rho c \pi \sqrt{\pi \alpha(t - t')}(r^2 + 8\alpha(t - t'))} exp\left(-\left(\frac{2(x - v_i t')^2}{r^2 + 8\alpha(t - t')}\right.\right.$$

$$\left.\left. + \frac{2(y - v_i t')^2}{r^2 + 8\alpha(t - t')} + \frac{z^2}{4\alpha(t - t')}\right)\right) dt'$$

$$+ \int_0^t \frac{F(T_m - T_0)}{\rho \pi \sqrt{\pi \alpha(t - t')}(r^2 + 4\alpha(t - t'))} exp\left(-\left(\frac{(x - v_i t')^2}{r^2 + 4\alpha(t - t')} + \frac{(y - v_i t')^2}{r^2 + 4\alpha(t - t')}\right.\right.$$

$$\left.\left. + \frac{z^2}{4\alpha(t - t')}\right)\right) dt'$$

Equation 5-1

where β denotes the laser-material absorptivity, P denotes the power of the heat source, F denotes the powder feed rate, ρ denotes the material density, c denotes the specific heat, α denotes the thermal diffusivity, r denotes the heat source radius, T_m denotes the melting temperature, and T_0 denotes the room temperature. To make the model more tractable, some simplifications/assumptions are considered including the enhanced thermal diffusivity, effective heat source radius, increased specific heat, and enhanced absorptivity. The details of the above-mentioned considerations are available in Ref. [108].

As opposed to single-track deposition in which the deposition happens on a substrate at room temperature, the multi-track deposition is the product of depositing subsequent tracks. To compute the temperature field in multi-track deposition, the temperature contribution of individual tracks must be considered. The temperature contributions of previous tracks act as an initial temperature for the subsequent tracks. When the first track is deposited, the initial temperature is the ambient temperature, and heat accumulation happens as the deposition continues. The initial temperature at the point of interest is the sum of the ambient temperature and the temperature contributions of previous tracks. Let i denotes the track index. The accumulated temperature T_n^{AC} for the deposition of n total tracks can be derived as:

$$T_n^{AC}(x, y, z, t^s, t) = T_0 + \sum_{i=1}^{i=n} T_i^{AC}(x, y, z, t_i^s, t)$$

Equation 5-2

The calculation of T_i^{AC} can be improved by simulating the cooling stage of each track, which has been implemented before [19,41,109,110]. Assume that, for the deposition of each track, the heat source is switched on at the beginning of the track at the time instant of t_i^s while moving with a constant speed of v_i in a direction for the length of L_i until it arrives at the endpoint of the track at the time instant of t_i^e ($t_i^e = t_i^s + L_i/v_i$). The cooling stage of each track happens, as shown in Figure 5-2. The cooling stage continues in the part for a certain cooling time and two factors with positive and negative heat inputs contribute to defining the cooling stage. The factor with positive heat input is assumed for the continuation of the heat transfer in the time domain. The factor with negative heat input is assumed to compensate for the heat sink when the heat source is off. Since the positive heat input starts earlier than the negative one, the summation of the temperature contributions is positive but it decreases over time, mimicking the cooling stage. After a certain time, the summation reaches zero, which implies a complete cooling stage when the temperature of the part equals the ambient temperature. Based on this model, the temperature contribution of each track is considered and the movement of the subsequent track is accounted for by the position/time of the start/endpoints of each track.

$$T_i^{AC}(x, y, z, t_i^s, t) = T_i(x, y, z, t_i^s, t) - T_i(x, y, z, t_i^e, t)$$

Equation 5-3
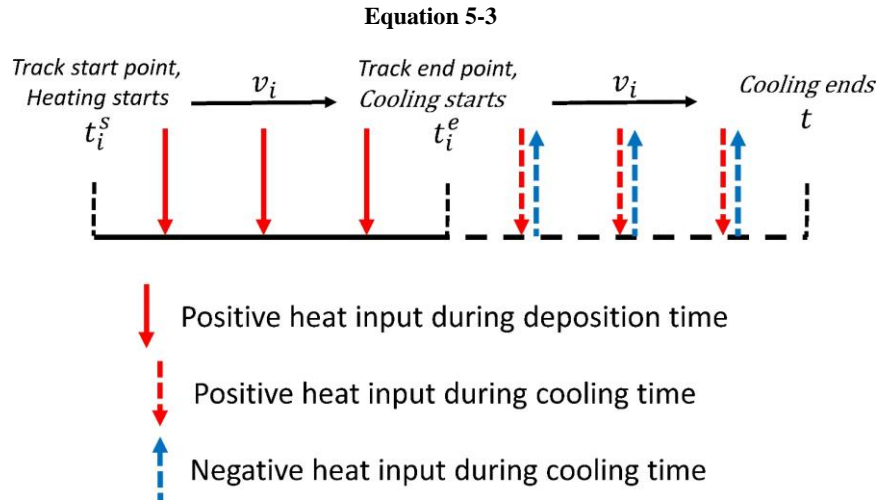
Figure 5-2. Schema of heat inputs for each track during deposition and cooling time.

5.2.2 Geometrical Profile of Overlapping Beads

The melt-pool geometry can be estimated based on the liquid-solid isotherms defined by the transient temperature field in different planes plane. Ignoring the effect of overlapping beads, the deposit bead

height can be derived assuming a uniform powder flow density over the projection of the melt pool on the x-y plane [18]. The maximum height of the bead H_i can be estimated as:

$$H_i = \frac{W_i F}{\pi \rho_p v_i r_{ps}^2}$$

Equation 5-4

where W_i denotes deposition width, ρ_p denotes the density of powder material, r_{ps} denotes the effective radius of the powder stream column on the substrate. To get the height profile of a single bead, a polynomial curve can be fitted to the data points of the width and maximum height. Please note that the geometry of each track bead is dynamic, changing over time/location based on the transient temperature field.

For a realistic prediction of the geometrical profile of multi-track deposition, the effect of overlapping beads should be considered. Mathematical models based on geometrical functions such as parabolas have shown high computational efficiency in geometrical prediction, as opposed to FEM numerical simulations in which all complex multi-physics of the heat flow and fluid motion have to be considered. Ocelík et al. [111] and Nenadl et al. [112] developed a mathematical model based on parabolic functions to predict the geometry of overlapping beads. However, their models only work for two intersecting beads in direction-parallel scanning strategies. Santos Paes et al. [113] developed a mathematical model for three intersecting beads which is applicable for contour-parallel and combined strategies. However, the model only considers the case when a third bead is in between two previously deposited beads and those two beads are not overlapping. Depending on the processing parameters and scanning strategies, there might be other cases of intersecting beads that need a universal algorithm to predict the geometrical profile.

Inspired by the previous works, we developed an algorithm for overlapping beads that can take into account the addition of extra material as a result of the heat accumulation effect and overlapping beads. The algorithm can work for any scanning strategies, multi-track/multi-layer deposition, and any number of intersecting beads. The geometry of each bead can be estimated with a parabolic function as $f_i = a_i y^2 + b_i y + c_i$, in which the coefficients of a_i, b_i, and c_i can be found by solving the following equations for the conservation of mass (using the cross-sectional area as a proxy).

$$\begin{cases} f_i(A_i) = f_j(A_i) \\ f_i(B_i) = f_k(B_i) \\ \int_{A_i}^{B_i} f_i dy = \frac{2W_i H_i}{3} + \sum_{\eta=1}^{\psi} \int_{l_\eta}^{l_{\eta+1}} f_{p_{n(\eta)}} dy \end{cases}$$

Equation 5-5

where f_i is the polynomial of track i on top of previous tracks, f_j is the polynomial for track j, intersecting the left side of track i, f_k is the polynomial for track k, intersecting the right side of track i. In the general case, the integrands in Equation 5-5 are all parabolas for tracks under track i and the integration limits l are a subset of all the locations of A and B points from tracks under track i. p_n stores the list of the parabolas that should be integrated between subsequent l limits. As an example of a specific case of three overlapping beads, a graphical summary of the algorithm used to find the parabolic function of the third bead, including how to find out the integration limits and the indices for the parabolas corresponding to the three beads, is shown in Figure 5-3. The dashed curves are the beads before considering the overlapping effect. The algorithm consists of three steps: first, finding the intersecting beads, second, finding the integration limits, and third, determining the tracks to integrate between those limits, by checking the height of the beads halfway between adjacent limits.
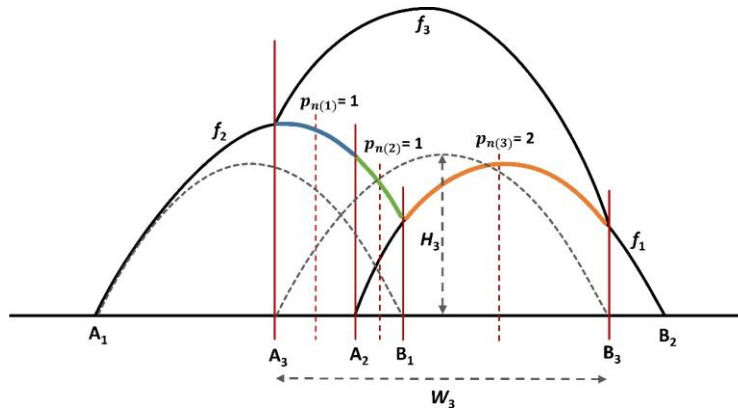
Figure 5-3. Schematic representation of using the universal algorithm for dynamic profile modeling of three beads.

5.2.3 Solidification Characteristics

Some microstructural features, including grain structure/substructure, can be directly estimated from the calculated solidification parameters which are derived from the transient temperature field [114].

In LDED-PF, the solidification front moves with the laser beam. The local heat flow direction at the longitudinal center-plane of each track can be used for rapid estimation of the solidification parameters as shown in Figure 5-4. The direction of heat flow at any location along the solid-liquid interface is normal to the solidification front. The thermal gradient along the solidification front (G) can be expressed as:

$$G = \sqrt{\left(\frac{\partial T}{\partial x}\right)^2 + \left(\frac{\partial T}{\partial y}\right)^2 + \left(\frac{\partial T}{\partial z}\right)^2}$$

Equation 5-6

The solidification rate (R) along the solidification front is:

$$R = v_i \cos \theta_s$$

Equation 5-7

The angle (θ_s) between the heat flow direction along the solidification front and laser scanning direction can be calculated as follows:

$$\cos \theta_s = \frac{\left(\frac{\partial T}{\partial x}\right)}{\sqrt{\left(\frac{\partial T}{\partial x}\right)^2 + \left(\frac{\partial T}{\partial y}\right)^2 + \left(\frac{\partial T}{\partial z}\right)^2}}$$

Equation 5-8
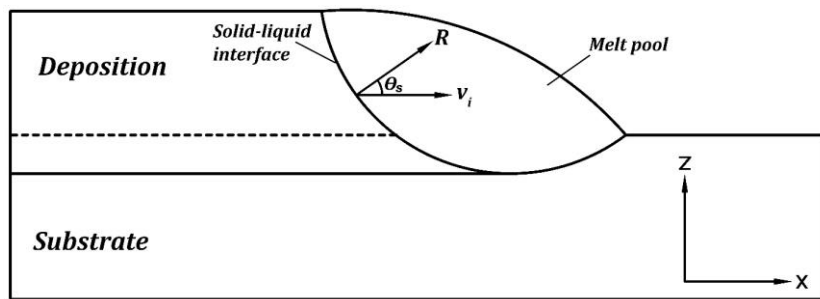
Figure 5-4. Schema of solidification front at longitudinal center-plane of the track.

The solidification cooling rate $\dot{T}$ at any point along the solidification front may be derived as:

$$\dot{T} = GR$$

71

Equation 5-9

The solidification substructure is dependent on G and R values. The substructure mode, depending on G and R values, can be planar, cellular, columnar dendritic, or equiaxed dendritic. The solidification substructure size (cellular and dendritic spacing) also depends on G and R values [47]. A solidification map can be developed to study the solidification substructure mode of the material produced by LDED-PF. Inspired by the original work of Hunt [115] on directional solidification, Gäumann et al. [45] proposed a relationship between G and R values, and volume fraction of equiaxed grains ($\emptyset$):

$$\frac{G^{n'}}{R} = a' \left(\sqrt[3]{\frac{-4\pi N_0}{3\ln(1-\emptyset)} \frac{1}{n+1}} \right)^{n'}$$

Equation 5-10

where n' and a' are constants, and N_0 is the density of nucleation sites. The mean value of any functional relationships for variables G and R over the melt pool z distance (z_{min} to z_{max}) can be calculated as follows:

$$\overline{\left(\frac{G^{n'}}{R}\right)_z} = \frac{1}{(z_{max} - z_{min})} \int_{z_{min}}^{z_{max}} \frac{G^{n'}}{R} dz$$

Equation 5-11

Another important factor for quantifying solidification substructure size is primary dendritic arm spacing (PDAS). Two theoretical models have been proposed by Hunt [116], and Kurz and Fisher [117] to predict PDAS.

$$PDAS = 2.83(k'\Delta T_0 D\Gamma)^{0.25} G^{-0.5} R^{-0.25}$$

Equation 5-12

$$PDAS = 4.3 \left(\frac{\Delta T_0 D\Gamma}{k'}\right)^{0.25} G^{-0.5} R^{-0.25}$$

Equation 5-13

where Γ denotes the Gibbs–Thomson coefficient, k' denotes the partition coefficient, D denotes the liquid diffusion coefficient, and ΔT_0 denotes the equilibrium freezing range (The difference between liquidus T_l and solidus T_s temperature).

The grain size λ has been also proposed to be related to solidification cooling rate $\dot{T}$ based on the classical theory of homogeneous nucleation and isotropic linear growth during rapid solidification by Boswell and Chadwick [118].

$$\lambda = A\dot{T}^m$$

Equation 5-14

where A and m are material-dependent parameters.

5.3 Experimental Procedures

Experiments were carried out using an LDED-PF system (IC106, DM3D Technology). The system is equipped with a disk laser (TruDisk 2000, TRUMPF), an ABB robotic arm, and a pneumatic powder feeder with a coaxial nozzle tip. The depositions were carried out in an atmosphere-controlled chamber and the oxygen level was about 10 ppm. The standoff distance (the distance between the nozzle tip and substrate) was set to 10 mm. The spot size of the laser beam at the standoff distance was measured as 1.4 mm. The powder carrier gas (Argon) flow rate was set to 4 L/min. The powder hopper cover gas (Argon) flow rate was set to 8 L/min. The Nozzle gas flow rate was set to 6 L/min Argon and 4 L/min Helium. The nozzle shaping gas (Argon) flow rate was set to 6 L/min. To avoid the change in the chemical composition of the depositions as a result of mixing with the substrate, the feedstock powder and substrate of the same Ti-5Al-5V-5Mo-3Cr (Ti-5553) alloy were used. The feedstock powder was spherical plasma-atomized Ti-5553 powder (AP&C, GE Additive) with particle size ranging from 45 to 106 μm. The plates of the same alloy were printed with powder bed fusion technique (EOS M290) as substrate material. Multi-track LDED-PF of square-geometry tool-paths (10×10 mm) was performed at different laser power (P), scanning speed (v_i), and step-overs (h_s). Each sample is assigned a code that shows its scanning strategy and processing parameter set (Table 5-1). Four scanning strategies of the unidirectional, bidirectional, inward spiral, and S-pattern are coded as Uni, Bi, Spiral, and SP, respectively. The processing parameter sets are coded as numbers. The combination of a numbered processing parameter set and scanning strategy's code makes the sample's label. For

example, the sample with processing parameter set 2 and bidirectional scanning strategy is labeled as Bi-2.

Table 5-1. Processing parameter sets of multi-track LDED-PF

Processing parameter set	Laser power (W)	Scanning speed (mm/s)	Powder feed rate (g/min)	Step-over (mm)
1	600	5	6	0.5
2	600	10	6	0.5
3	600	5	6	1
4	600	10	6	1
5	800	5	6	0.5
6	800	10	6	0.5
7	800	5	6	1
8	800	10	6	1
9	400	5	6	0.5

After the LDED-PF fabrication of the samples was finished, the samples were prepared for metallographic examination. Optical microscopy (OM) (VHX-7000, KEYENCE) was used to examine the multi-tracks and their sub-grain structure. For the OM examinations, the samples were cross-sectioned, mounted, ground, polished, and then etched with Keller's etchant. The PDAS was measured in different locations of the tracks using ImageJ software. The grain structure was investigated using the electron backscatter diffraction (EBSD) technique (QUANTAX, BRUKER). For the EBSD examinations, the samples were cross-sectioned, mounted, ground, and vibratory-polished. EBSD investigations were performed at an acceleration voltage of 20 kV and analyzed with ESPRIT2 software. The EBSD mappings of all the samples were obtained using a step size of ~4 μm. To measure the volume fraction of equiaxed grains, the aspect ratio of grains is evaluated. The grains are taken as equiaxed when their aspect ratio is bigger than 0.4 [119].

The model programming was performed in Matlab® R2019a using a DELL® computer with Intel® Core™ i7-7700 CPU @ 3.60 GHz RAM 16.0 GB. The thermophysical properties of Ti-5553 alloy are assumed to be temperature-independent. The thermophysical properties of the materials are assumed to be temperature-independent within the range of room temperature to the material's melting temperature. The average value of the thermophysical properties in the range from room temperature

to melting temperature was used for model calculation. The thermophysical/solidification properties of the material are presented in Table 5-2. For some of the properties, the properties of Ti-64 alloy are considered when the data for Ti-5553 alloy is not available in the literature.

Table 5-2. Thermophysical/solidification properties of Ti-5553 alloy

Properties	Value	Ref.
Melting Temperature [K]	1923	[108]
Density [g/cm^3]	4.65 (@298 K)-4.2 (@1923 K)	[108]
Thermal conductivity [W/m·K]	5 (@298 K)-29 (@1923 K)	[108]
Specific heat [J/(g·K)]	0.51 (@298 K)-0.8 (@1923 K)	[108]
Laser absorptivity	0.5	[108]
Coefficient of enhanced thermal diffusivity	1.4	[108]
Effective radius of the heat source [mm]	1	[108]
Liquidus temperature [K]	1928	[120]
Solidus temperature [K]	1878	[120]
Liquid diffusion coefficient [mm^2/s]	9.5×10^{-3}	[120]
Gibbs–Thomson coefficient [K·mm]	1.88×10^{-4}	[120]
Partition coefficient	0.5	[120]

5.4 Results and Discussion

5.4.1 Temperature Simulation in x-y Plane

To study the temperature distribution under different scanning strategies, the transient temperature fields were simulated in the x-y plane for the scanning strategies at different processing parameters. For these simulations, the model was a square-geometry deposition (10×10 mm) and a square substrate (20×20 mm). The temperature fields at the end of the depositions in the x-y plane for different scanning strategies at one processing parameter set are shown in Figure 5-5 as an example of these simulations. The computational time of these simulations was recorded as 111-205 sec with the x/y increment of 0.1 mm, and the integration time interval of 0.01 sec.
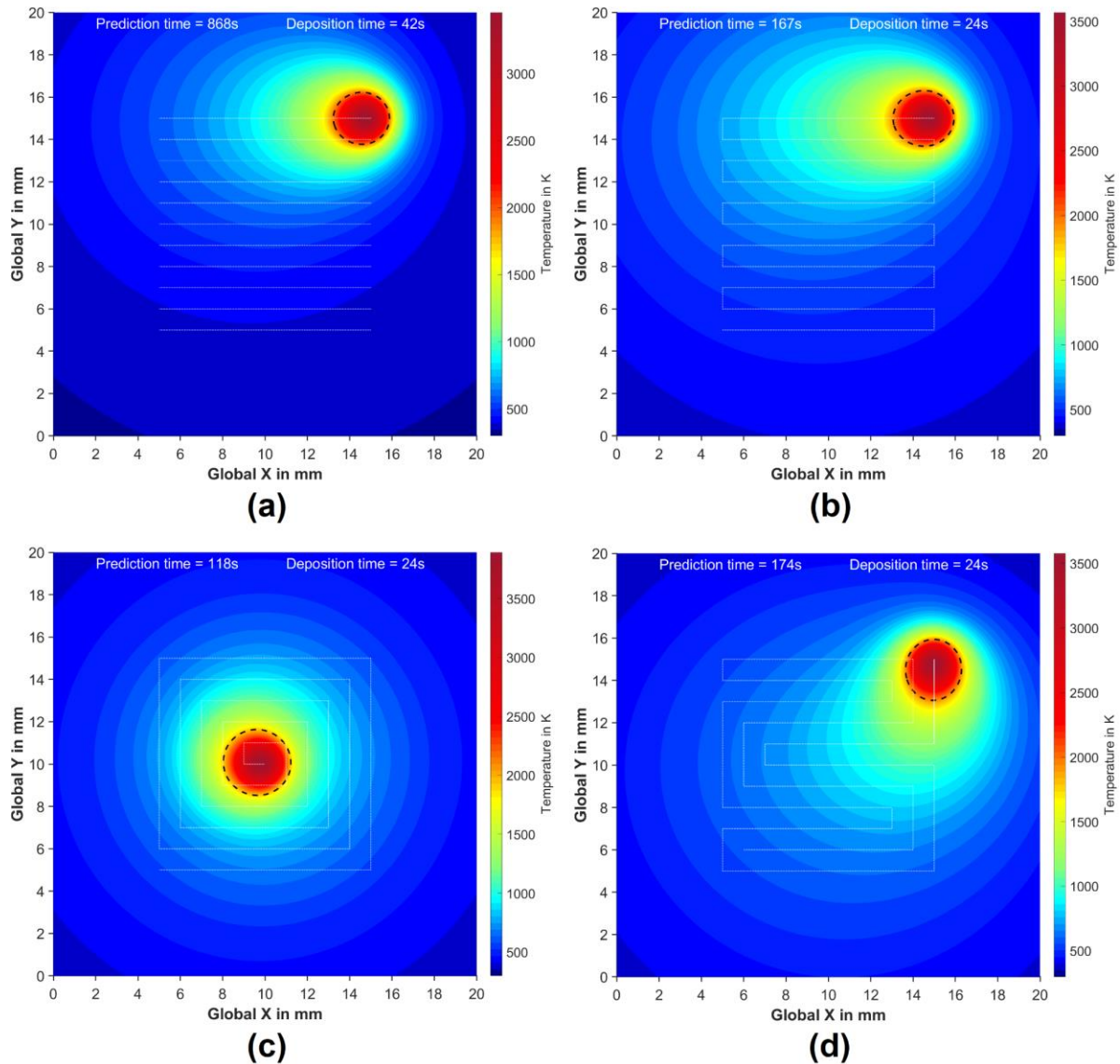
Figure 5-5. The transient temperature fields at the end of the depositions in the x-y plane under the same processing parameter set (*P*=600 W, *F*=6 g/min, v_i=5 mm/s and h_s=1 mm) and different scanning strategies; (a) unidirectional, (b) bidirectional, (c) inward spiral, and (d) S-pattern strategy.

The dashed black contour shows the projection of the melt pool on the x-y plane. It is observed that the scanning strategy affects the melt pool size. The effect is more evident in the case of the inward spiral strategy. The scanning strategy remarkably affects the temperature distribution. For the unidirectional and bidirectional strategies, the temperature distribution patterns are similar since these strategies are direction-parallel. The temperature is symmetrically distributed along the y-axis. The only

difference between them is their corresponding temperature values. The temperature values are higher within the distribution pattern in the bidirectional strategy because the laser source is continuously on; however, the laser source turns on and off in the unidirectional strategy, and there is a delay time between the scans. For the inward spiral strategy, the temperature is circularly distributed with its concentration in the center of the pattern. The maximum temperature is highest in this strategy and the final size of the melt pool is highest due to the concentration of temperature in the center. In the S-pattern strategy, the temperature distribution is more or less diagonal symmetric.

The residual stress and distortion are related to the temperature distribution. Sun et al. [107] proposed a qualitative evaluation method to compare the residual stress under different scanning strategies. According to this evaluation method, the residual stress distribution is correlated with the uniformity of the temperature field, which is determined by the peak temperature (T^p) at the four corners of the substrate. The equivalent residual stress, which is relevant to plastic yielding, is inversely correlated with the average peak temperature of the corners. The maximum principal residual stress, which is the main factor of fatigue and fracture performance, is inversely correlated with the minimum peak temperature of corners [107]. Figure 5-6 summarizes the results of the peak temperature calculation for the four corners under the same processing parameter set and four different scanning strategies. The peak temperatures in the bidirectional and unidirectional strategies show a larger difference. For S-pattern and inward spiral strategies, the difference among the peak temperatures is less because the temperature distribution in all directions is relatively uniform whereas the direction-parallel patterns (bidirectional and unidirectional) accumulate temperature on one side.
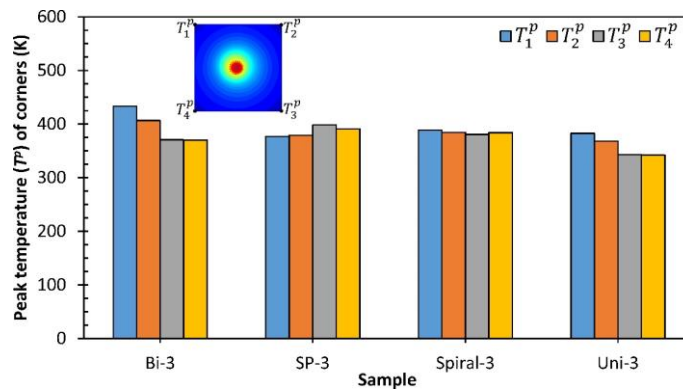

Figure 5-6. Peak temperatures of the corners under the same processing parameter set (P=600 W, F=6 g/min, v_i=5 mm/s and h_s=1 mm) and different scanning strategies.

77

To have an indication of the residual stress, the minimum peak temperatures and average peak temperatures under the different scanning strategies are plotted in Figure 5-7. According to Sun et al. [107], the scanning strategy with higher average peak temperature and higher minimum peak temperature will induce lower residual stress. Comparing the results in Figure 5-7, it can be expected that the S-pattern strategy produces lower residual stress, and the unidirectional strategy produces higher residual stress. It should be noted that the correlation between the peak temperatures of the corners and residual stress provides a simple but qualitative comparison of the residual stress.
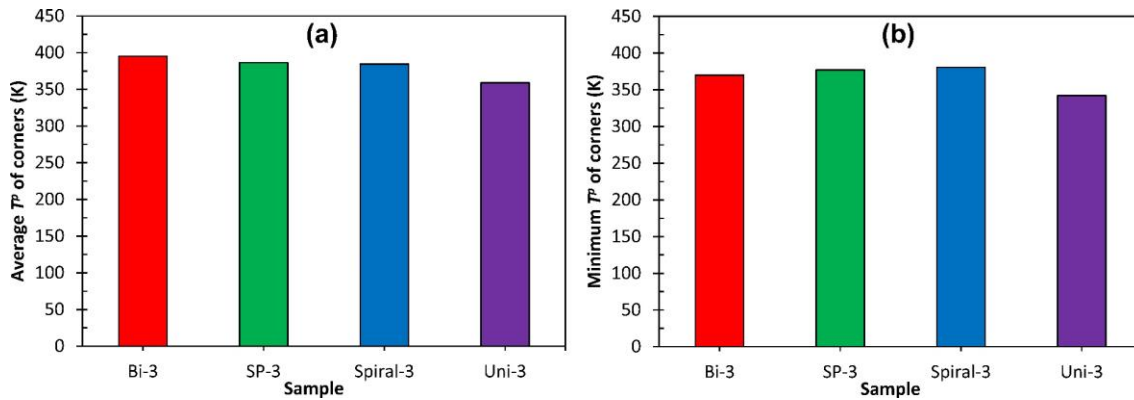
Figure 5-7. (a) Average and (b) minimum peak temperatures of the corners under the same processing parameter set (P=600 W, F=6 g/min, v_i=5 mm/s and h_s=1 mm) and different scanning strategies.

To better understand the thermal histories under different scanning strategies, the thermal cycles that the top surface of each track experiences and the resulting heating/cooling rates are investigated. Figure 5-8 represents the transient temperature for the points located along the transverse centerline at the half-length of the top surface of tracks. Figure 5-9 represents the heating/cooling rates caused by the thermal cycles at those points. The computational time of these simulations was recorded as 33-74 sec (depending on scanning strategy) with an integration time interval of 0.01 sec. The pattern of thermal cycles is similar in the case of the unidirectional and bidirectional strategies. The scan of all tracks happens side-by-side and the distance between two subsequent scans is equal to one step-over distance. At the time that the laser heat source scans each track, the temperature of that track reaches its peak and the adjacent tracks show the second-highest temperature peak. The peak temperatures decrease to ambient as the laser heat source gets farther away from the track. The only difference is the value of peak temperature in the cycles. Since the bidirectional is a continuous strategy, the effect of heat accumulation in increasing the peak temperature is more evident. The unidirectional strategy has a

delay time between subsequent scans when the laser heat source is off and the material has time for cooling down. In the inward spiral strategy, the cycles are at a distance from each other since the scan of the adjacent tracks happens at every four tracks. As the laser heat source becomes closer to the center, the distance between the cycles becomes smaller and the peak temperature increases. The thermal cycles become more complex close to the center and the heat accumulation is at the highest level which causes the heating/cooling rates to decrease. The S-pattern strategy causes the cycles to have a unique pattern. The scan of tracks happens in a sequence such that the distance between the locations of two subsequent scans changes from 1 step-over to 5 step-overs. The cycles are sometimes at a close distance and sometimes at a far distance from each other. The peak temperature of the cycles shows an increase at the beginning but shows a small fluctuation as the scan continues.
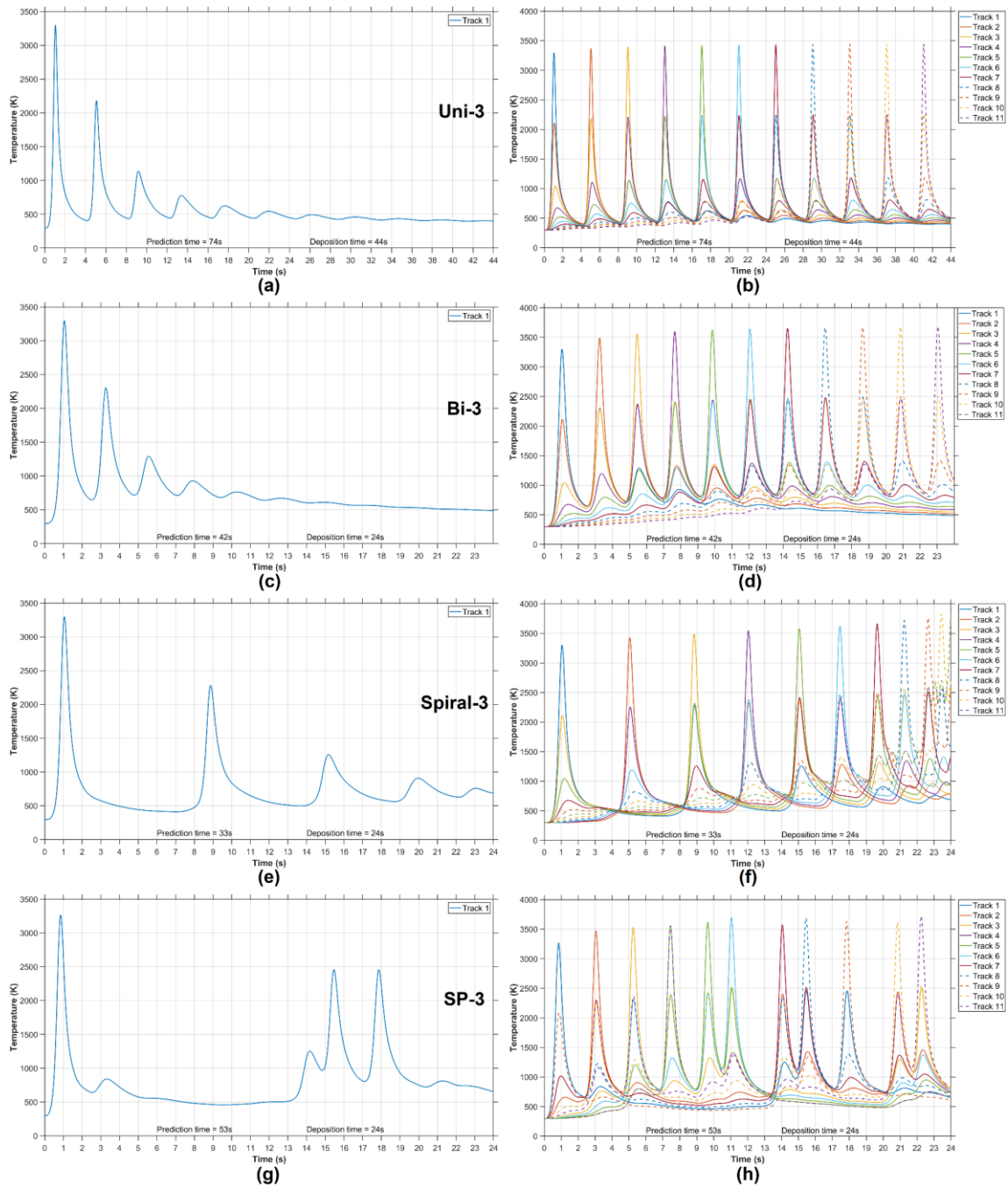
Figure 5-8. Thermal cycles of the tracks under the same processing parameter set (P=600 W, F=6 g/min, v_i=5 mm/s and h_s=1 mm) and different scanning strategies. The calculations were performed at (a), (c), (e), (g) the point located at the half-length of the first track, and (b), (d), (f), (h) the points located vertically at the half-length of all tracks; (a), (b) unidirectional, (c), (d) bidirectional, (e), (f) inward spiral, and (g), (h) S-pattern strategy.
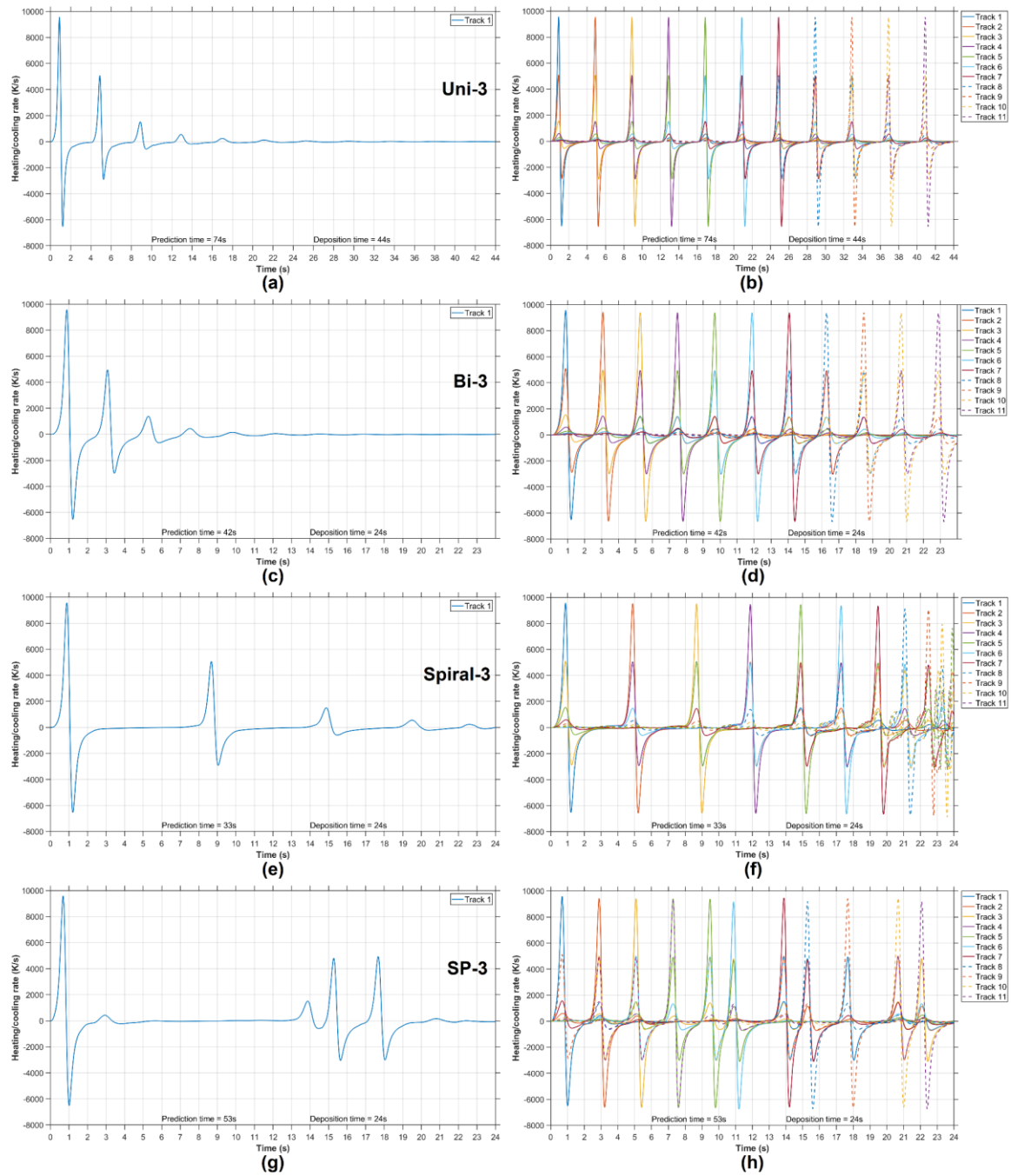
Figure 5-9. Hating/cooling rates of the tracks under the same processing parameter set (P=600 W, F=6 g/min, v_i=5 mm/s and h_s=1 mm) and different scanning strategies. The calculations were performed at (a), (c), (e), (g) the point located at the half-length of the first track, and (b), (d), (f), (h) the points located vertically at the half-length of all track; (a), (b) unidirectional, (c), (d) bidirectional, (e), (f) inward spiral, and (g), (h) S-pattern strategy.

81

5.4.2 Geometrical Profile of Overlapping Beads

To predict the geometrical profile of the overlapping beads under different scanning strategies, the transient temperature was simulated, for all the strategies at different processing parameter sets, along the transverse centerline of the deposition which is at the half-length of the tracks. Based on the developed universal algorithm for overlapping beads, Figure 5-10, Figure 5-11, Figure 5-12, and Figure 5-13 show the measured and simulated results of transverse cross-section profiles for the unidirectional, bidirectional, inward spiral, and S-pattern strategies, respectively. The computational time of these simulations was recorded as 5-133 sec (depending on scan strategy) with the y increment of 0.05 mm, and the integration time interval of 0.01 sec.
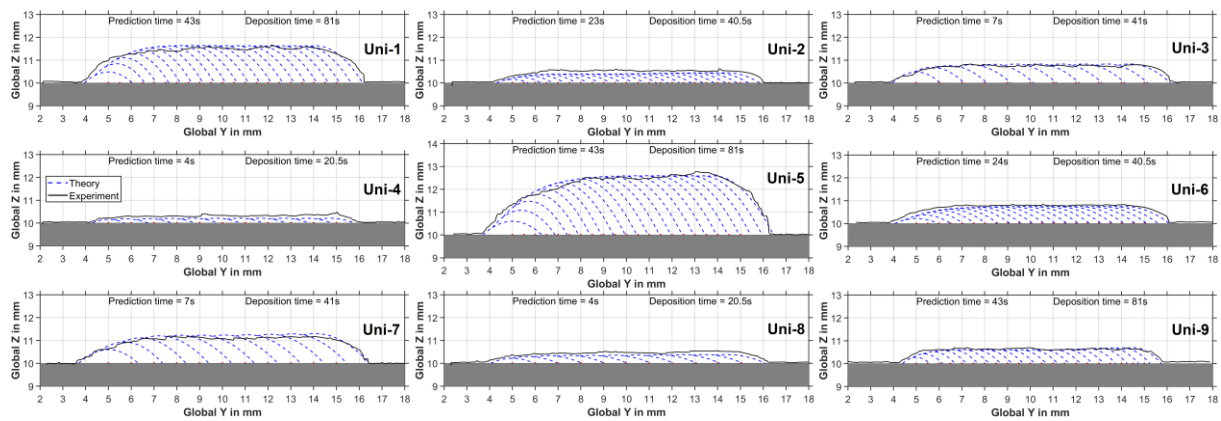
Figure 5-10. Measured and simulated results of transverse cross-section profiles for unidirectional scanning strategy under different processing parameter sets.
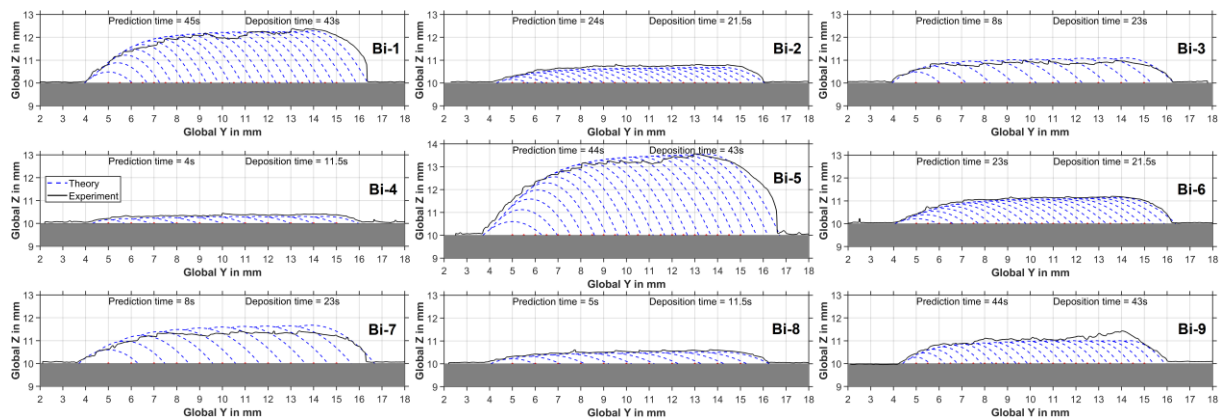
Figure 5-11. Measured and simulated results of transverse cross-section profiles for bidirectional scanning strategy under different processing parameter sets.
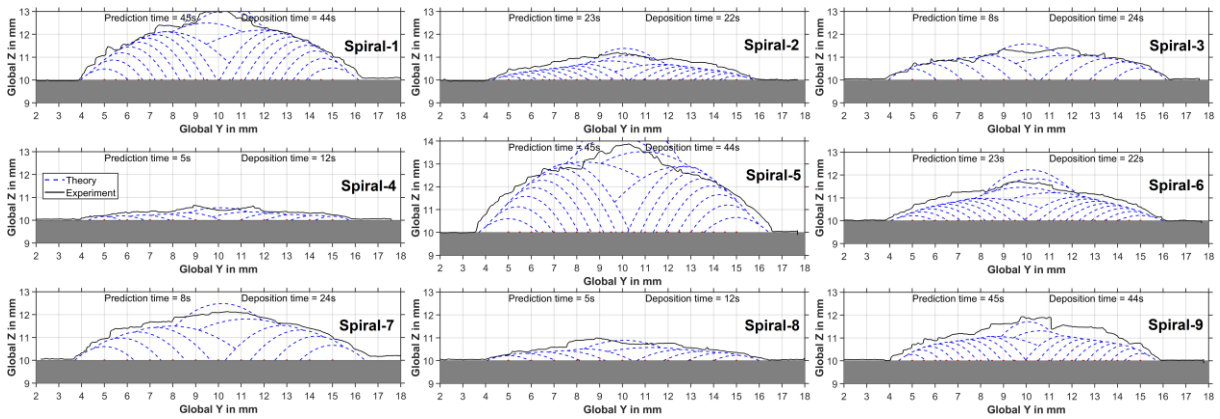
Figure 5-12. Measured and simulated results of transverse cross-section profiles for inward spiral scanning strategy under different processing parameter sets.
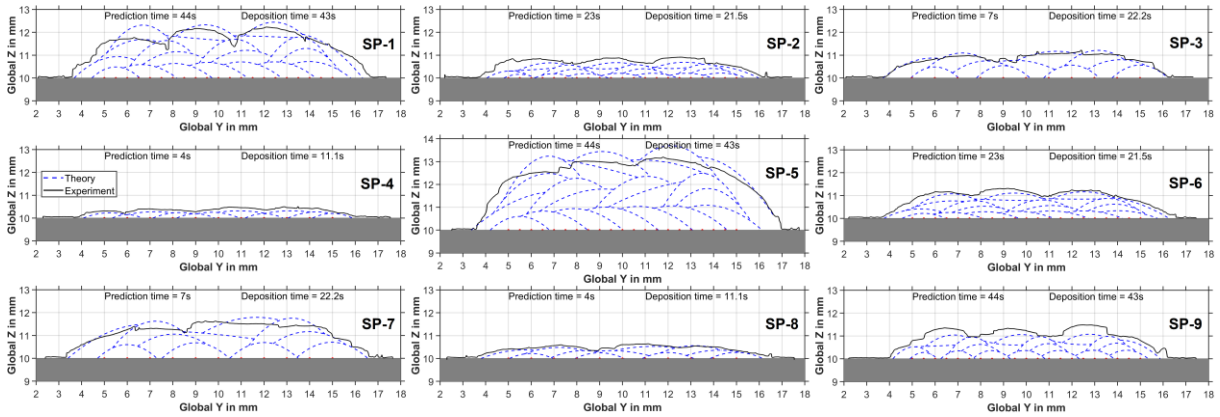
Figure 5-13. Measured and simulated results of transverse cross-section profiles for S-pattern scanning strategy under different processing parameter sets.

The solid black lines in the figures are the results of experimental measurements and the dashed blue lines are the simulated results for the overlapping beads. The experimental measurements were done by 3D imaging and analysis in optical microscopy. Figure 5-14 shows an example of the 3D imaging and analysis at the transverse cross-section. In the case of the four scanning strategies and the nine processing parameter sets, the simulated profiles are in close agreement with the measured profiles. The small mismatch between the simulated and measured data can be attributed to the fact that the heat convection and radiation are ignored in the model. The effects of heat accumulation and overlapping beads are evident in the figures. The processing parameters define the initial height/width while the step-over significantly influences the final height/width of the overlapping beads. The developed

83

universal algorithm for predicting the geometrical profile of overlapping beads is an efficient approach that can work for any scanning strategies/processing parameters and any number of layers/intersecting beads. As for the dimensional accuracy of the depositions, having a tool-path of square geometry (10 × 10 mm), the unidirectional and bidirectional strategies led to the depositions with a more or less constant height. However, the inward spiral and S-pattern led to depositions with a fluctuating height. The dynamic change in the deposition rate of the material is responsible for these observations. As the temperature distribution changes with the scanning strategy, the deposition rate dynamically changes in each track. In the scanning strategies that the side-by-side deposition happens in a specific direction, the deposition rate and height of the tracks gradually increase in that direction until they reach a peak level. However, in the scanning strategies that the side-by-side deposition changes direction, the deposition rate and height of the tracks fluctuate.
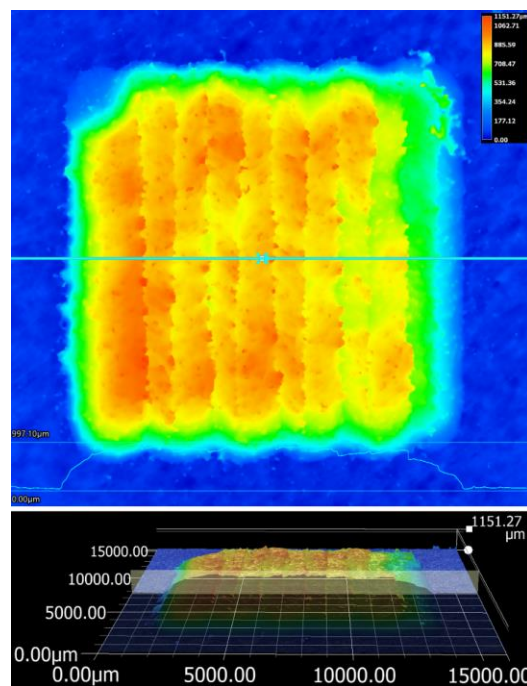
Figure 5-14. 3D imaging and analysis in the optical microscopy used to measure the transverse cross-section profile under bidirectional scanning strategy and the given processing parameter set (P=600 W, F=6 g/min, v_i=5 mm/s and h_s=1 mm).

5.4.3 Temperature Simulation in y-z and x-z Planes

The predictions of the final height of the tracks can be used for temperature simulation in the x-z and y-z planes as the location of the heat source in the z-axis can be defined based on those predictions. The transient temperature fields were simulated at the transverse center-plane of the deposition (y-z plane) for all the scanning strategies at different processing parameter sets. For these simulations, the model was the transverse cross-sectional area of the deposition from the previous simulation of the geometrical profile and a rectangular substrate (20×2 mm). The temperature fields of the last tracks in the y-z plane for different scanning strategies at one processing parameter set are shown in Figure 5-15 as an example of these simulations. The computational time of these simulations was recorded as 371-483 sec with the y/z increment of 0.05 mm, and the integration time interval of 0.01 sec.

Figure 5-15. The transient temperature fields of the last tracks at the transverse center-plane of the depositions for the same processing parameter set (P=600 W, F=6 g/min, v_i=5 mm/s and h_s=1 mm) and different scanning strategies; (a) unidirectional, (b) bidirectional, (c) inward spiral, and (d) S-pattern strategy.

To test the accuracy of these predictions, the transverse cross-section of the depositions under different scanning strategies was experimentally investigated. Figure 5-16 represents the optical microscopic images of the transverse cross-sections. The melt pool boundaries are highlighted by solid black lines. Comparing Figure 5-15 and Figure 5-16, the capability and accuracy of the model in the prediction of the melt pool geometry are evident.
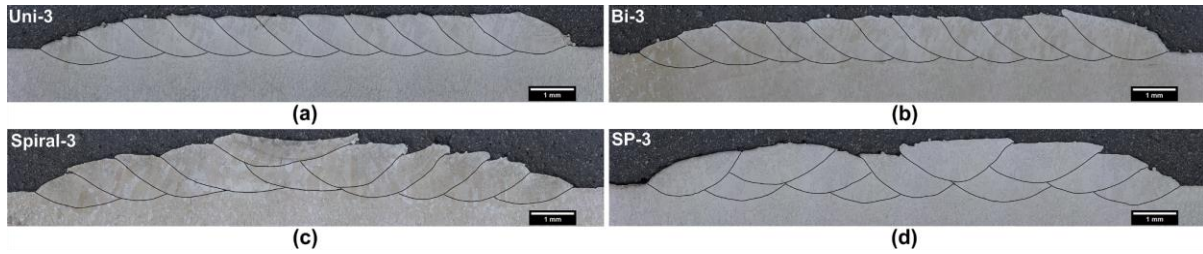
Figure 5-16. OM images of the transverse cross-section of the depositions under the same processing parameter set (P=600 W, F=6 g/min, v_i=5 mm/s and h_s=1 mm) and different scanning strategies; (a) unidirectional, (b) bidirectional, (c) inward spiral, and (d) S-pattern strategy.

The transient temperature fields along the heat-source direction of motion at the half-length of the tracks were also simulated at the longitudinal center plane of the tracks (x-z plane) for all the scanning strategies at different processing parameter sets. For these simulations, the model was the longitudinal cross-sectional area of the track at the half-length and a rectangular substrate (20×2 mm). Since the simulations at the longitudinal center plane of the tracks are similar in appearance, the temperature field of the last track in the x-z plane for bidirectional scanning strategy at the given processing parameter set is shown in Figure 5-17 as an example of these simulations. The computational time of this simulation was recorded as 401 sec with the x/z increment of 0.05 mm, and the integration time interval of 0.01 sec. The melt pool boundary which is taken as the solidification front is shown by the dashed black line.
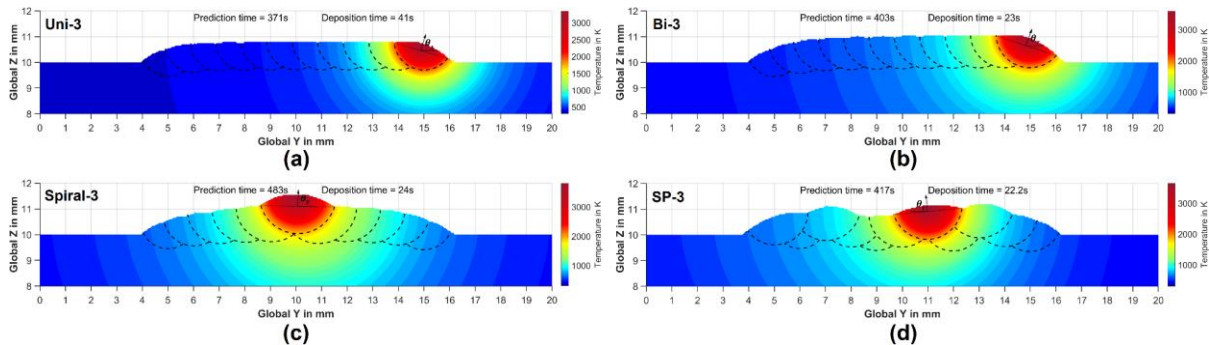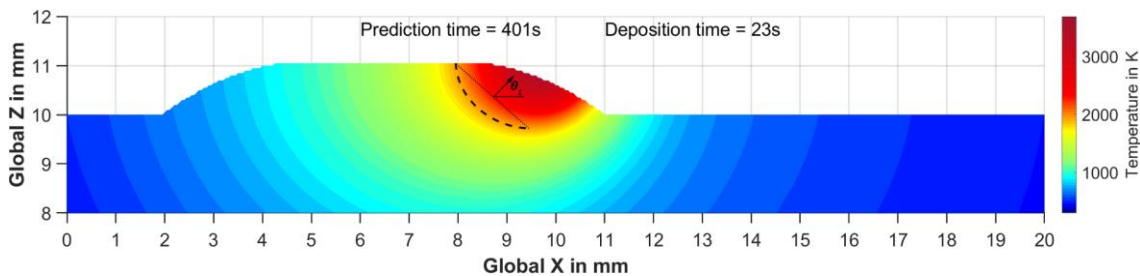

Figure 5-17. The transient temperature field of the last track at the longitudinal center-plane of the track for the given processing parameter set (P=600 W, F=6 g/min, v_i=5 mm/s and h_s=1 mm) and bidirectional scanning strategy.

86

5.4.4 Solidification Characteristics

5.4.4.1 Solidification Parameters

The solidification parameters i.e. the thermal gradient (G) and solidification rate (R) along the solidification front are the main factors to define the solidification microstructure. However, *in-situ* experimental measurement of these parameters is still challenging due to the highly spatially dependent nature of heating/cooling during LDED-PF. The mathematical model developed in this work is an effective approach to calculate the solidification parameters based on temperature predictions. For these calculations, the temperature predictions in the x-z plane at the longitudinal center plane of the tracks and two extra planes on the left and right of the center-plane with 0.05 offset were first used to get the values of G and R along the solidification front at the half-length of the tracks. Second, the temperature predictions in the y-z plane at the transverse center-plane were used to take out the values of G and R for the re-melted portion of each track.
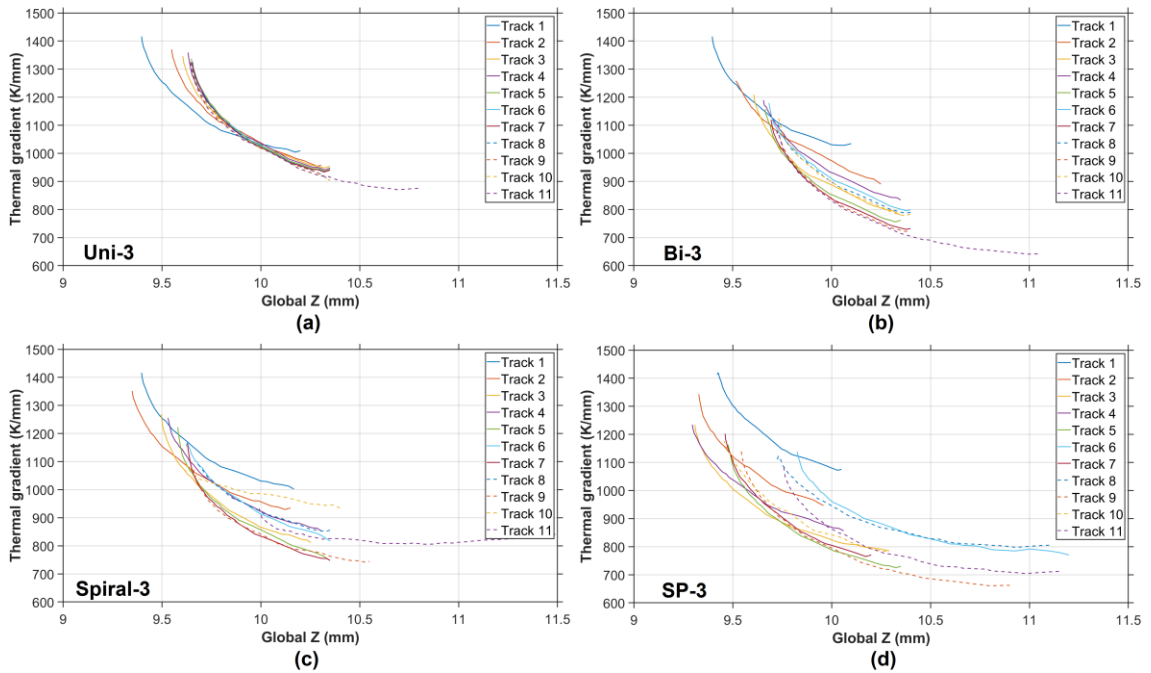
Figure 5-18. Thermal gradients at the center-plane of the tracks along the solidification fronts under the same processing parameter set (P=600 W, F=6 g/min, v_i=5 mm/s and h_s=1 mm) and different scanning strategies; (a) unidirectional, (b) bidirectional, (c) inward spiral, and (d) S-pattern strategy.

The thermal gradients and solidification rates of the tracks along the solidification fronts are plotted in Figure 5-18 and Figure 5-19, respectively. The thermal gradient is generally highest at the bottom of the melt pool and it decreases towards the top of the melt pool. The maximum thermal gradient for the given processing parameter set, which is around 1400 K/mm, is achieved at the bottom of the first track regardless of the scanning strategy. This is because the deposition of the first track happens on the substrate at room temperature when the temperature difference between the melt pool and substrate is considerably high. As the deposition continues and heat accumulation takes place, the thermal gradients of other tracks decrease. The heat accumulation makes the heat transfer slower (as a result of a weaker heat sink), therefore, a more uniform temperature distribution forms within the melt pool with a lower thermal gradient value. The thermal gradients of different tracks in the unidirectional strategy are similar. The delay time between two subsequent tracks allows the material to cool down and the effect of the heat accumulation is neutralized. In the bidirectional strategy, the thermal gradients keep decreasing for different tracks since the effect of the heat accumulation becomes stronger as the deposition continues. The thermal gradients of different tracks in the inward spiral and S-pattern strategies first decrease for the first few tracks and then fluctuate up and down because of the more complex heating/cooling cycles during the deposition. The S-pattern strategy has a more randomized pattern in terms of the thermal gradients. The minimum thermal gradient for the given processing parameter set is around 650 K/mm.

As for the solidification rate along the solidification front, it reaches its minimum value at the bottom melt pool and approaches its maximum value (close to the scanning speed) at the top of the melt pool. The changing pattern of the solidification rates in different tracks is similar. The major difference is in their location in the z-axis which is defined by the geometry of the deposition. Considering the total change in G and R, the simulated solidification cooling rates for the given processing parameter set are in the range of 0-7000 K/s for Ti-5553 depositions.
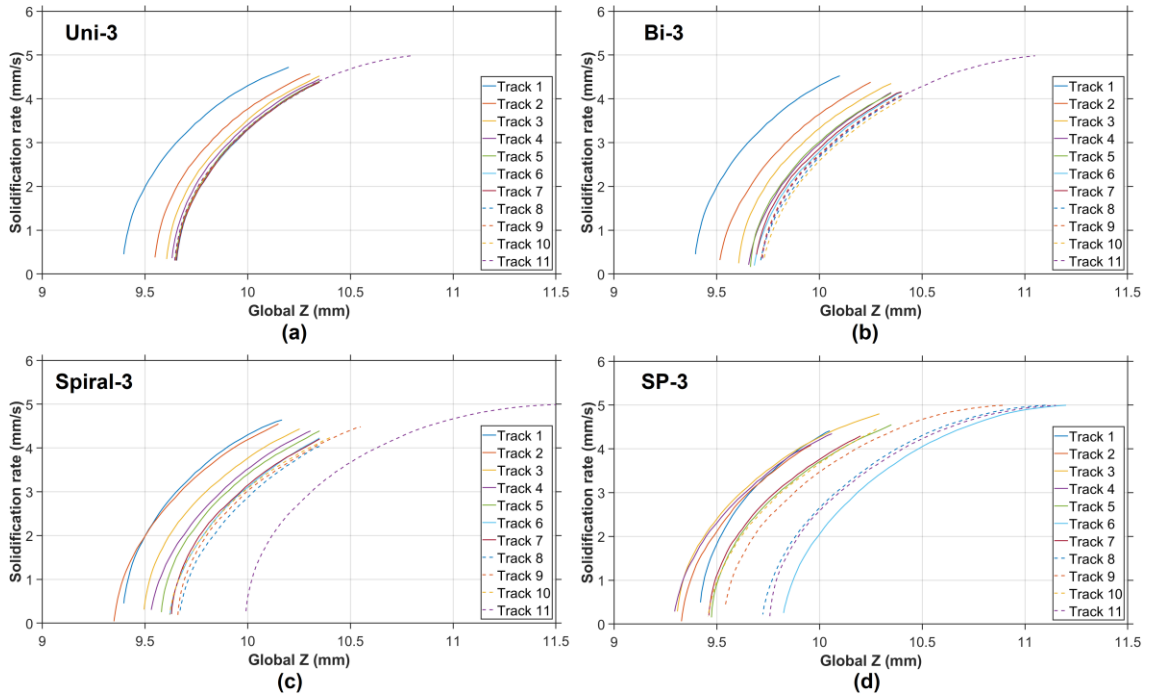
Figure 5-19. Solidification rates at the center-plane of the tracks along the solidification fronts under the same processing parameter set (P=600 W, F=6 g/min, v_i=5 mm/s and h_s=1 mm) and different scanning strategies; (a) unidirectional, (b) bidirectional, (c) inward spiral, and (d) S-pattern strategy.

5.4.4.2 Microstructural Observations

Figure 5-20 shows the morphology and orientation of grains throughout the multi-track depositions under the given processing parameter set and different scanning strategies. The microstructure mainly consists of different-sized β-Ti grains and the microstructural analysis is focused on the BCC structure of β grains. Both columnar and equiaxed grains are observable while their portion/distribution is different, depending on the scanning strategy. The columnar β grains grew at different angles with respect to the horizontal line and the angles change in different tracks depending on the scanning strategy.

During the solidification, the majority of grains obey the epitaxial growth mechanism due to rapid solidification and directional heat flow. However, new grains may be introduced to the melt pool and change the solidified grain structure. For AM processes, four nucleation mechanisms have been identified namely heterogeneous/homogenous nucleation, grain detachment, dendritic fragmentation, and surface nucleation [121]. Depending on the solidification condition, the nucleation rate may vary

and influence the grain structure. For instance, increasing laser scanning speed increases the probability of surviving partially melted particles, which introduce a higher nucleation rate through grain detachment and heterogeneous nucleation mechanisms [122]. Considering that the powder feed rate can be assumed constant during LDED-PF, it is the matter of solidification conditions (such as temperature distribution) to indicate the rate of unmelted or partially melted powder particles and enforce the existence of new grains in the microstructure. Therefore, it is essential to understand the correlation between the solidification parameters and microstructure when process conditions vary.
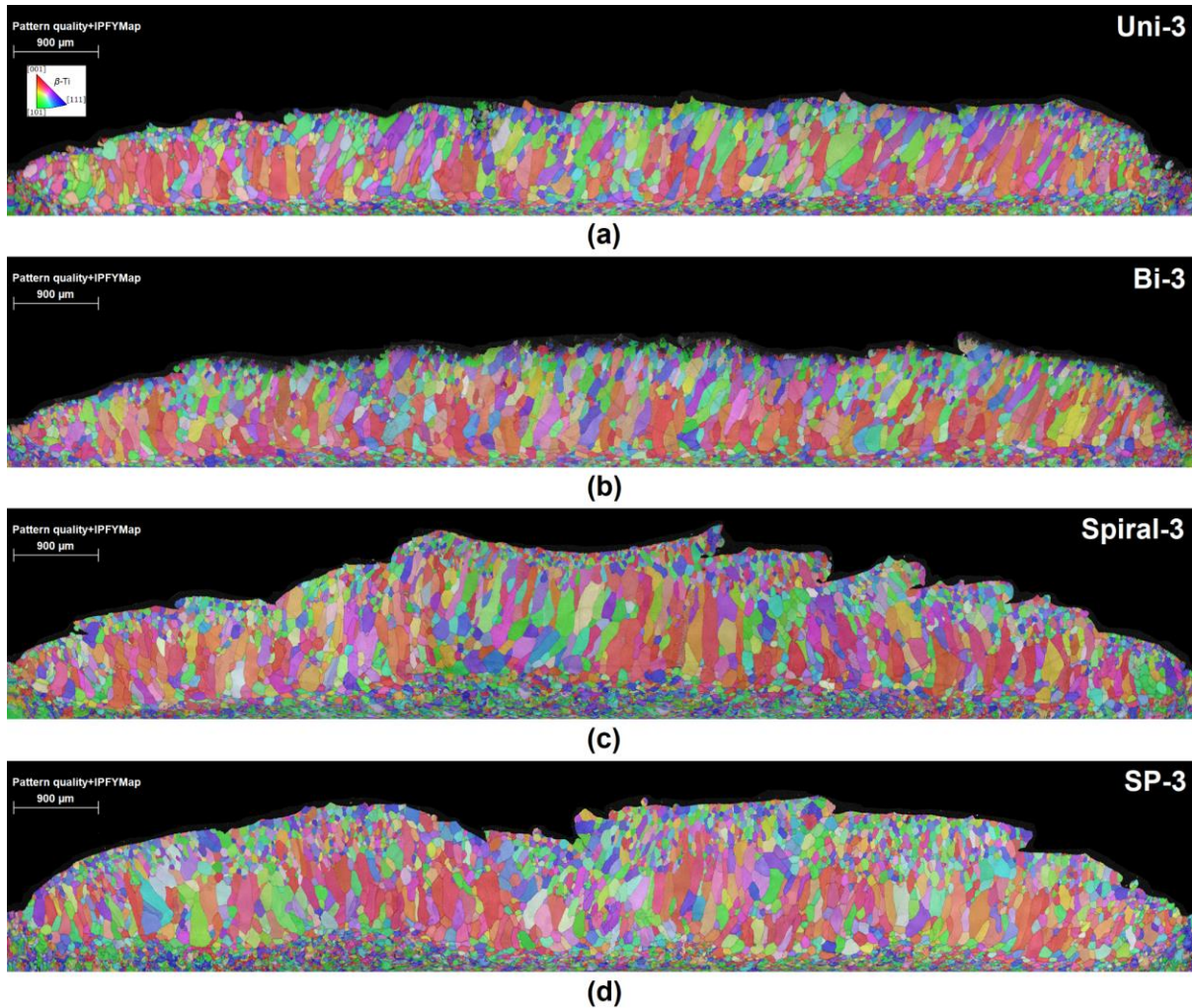

Figure 5-20. EBSD images showing the grain structure of the multi-tracks under the same processing parameter set (P=600 W, F=6 g/min, v_i=5 mm/s and h_s=1 mm) and different scanning strategies; (a) unidirectional, (b) bidirectional, (c) inward spiral, and (d) S-pattern strategy.

The sub-grain structure of the depositions shows a dendritic substructure which is typical in the LDED-PF process. Figure 5-21 represents the substructure of track 16 in sample SP-2 as an example of the dendritic solidification substructure. All four solidification modes are observable in the figure (the planar growth close to the melt pool boundary, the cellular growth, and then the columnar dendritic and equiaxed structure close to the melt pool top). Primary and secondary dendrites are also evident in the figure as the main characteristics of the solidification substructure. The size of dendrites can be different depending on the solidification conditions. The processing parameters and scanning strategy can induce specific solidification conditions in each track which lead to a different dendritic size. Based on the observations, some important microstructural features need to be justified, including the columnar grain growth orientation, columnar to equiaxed transition, dendritic size, and grain size. In the next sections, these microstructural features are linked to the process through the temperature modeling results, and a systematic model is developed for their predictions.

Figure 5-21. OM image showing the subgrain structure of track 16 (SP-2 sample) under the given processing parameter set (P=600 W, F=6 g/min, v_i=10 mm/s and h_s=0.5 mm) and S-pattern scanning strategy.

5.4.4.3 Columnar Grain Growth Orientation

The EBSD images showed that the growth direction of the columnar grains in different tracks happens at different angles with respect to the horizontal line. The maximum heat flow direction at the solidification front of each track can be different depending on the geometrical inclination of the melt pool. It should be noted that grains of different tracks may grow with a range of orientations. However,

91

the major competitive columnar growth happens along the maximum heat flow direction of the track. As the deposition of tracks happens, depending on the scanning strategy, the tracks become inclined at an angle. As discussed in the previous section, the geometrical profile of the melt pool in transverse and longitudinal cross-sections under different scanning strategies and processing parameter sets can be completely different. These geometrical differences of the melt pool orientation affect the heat flow direction at the solidification front.

Figure 5-22. Predicted maximum heat flow directions based on the geometrical inclination of the melt pools in the longitudinal cross-section under the same processing parameter set (P=600 W, F=6 g/min, v_i=5 mm/s and h_s=1 mm) and different scanning strategies; (a) unidirectional, (b) bidirectional, (c) inward spiral, and (d) S-pattern strategy.

In this work, we use the geometrical inclination of the melt pools to estimate the maximum heat flow direction in the transverse and longitudinal cross-sections. The examples of the derivation of the angle between the maximum heat flow direction and the horizontal line are graphically shown in Figure 5-15 and Figure 5-17 for the transverse (θ_T) and longitudinal (θ_L) cross-sections, respectively. Figure 5-22 shows the predicted maximum heat flow angle with respect to the horizontal line in the longitudinal cross-sections under the given processing parameter set and different scanning strategies. The average angle of the maximum heat flow direction with respect to the horizontal line for the given processing

92

parameter set is about 45° in the longitudinal cross-sections along the heat source moving direction regardless of the scanning strategy. The negative values of the angle show the change in the heat source's moving direction. For the unidirectional strategy, the laser heat source always moves in one direction which causes the longitudinal melt pool angle to be oriented towards one side for all the tracks. In the continuous scanning strategies, including the bidirectional, inward spiral, and S-pattern strategies, the laser heat source moves back and forth in opposite directions which causes the longitudinal melt pool angle to switch its orientation in every other track. The change in the melt pool angle orientation with respect to the horizontal line is shown by positive and negative values. The maximum heat flow direction in the longitudinal cross-section majorly depends on the scanning speed. If the laser heat source moves with a higher speed, the melt pool is elongated in the moving direction (so-called melt pool tail) and the longitudinal melt pool angle with respect to the horizontal line is increased. For the same scanning speed, the longitudinal melt pool angle stays within the same range and only changes orientation depending on the scanning strategy.

Figure 5-23 shows the predicted maximum heat flow angle with respect to the horizontal line in the transverse cross-section under the given processing parameter set and different scanning strategies. For direction-parallel scanning strategies such as the unidirectional and bidirectional, the transverse melt pool angle and maximum heat flow direction are always oriented to one side as the side-by-side overlapping happens only in one direction. For the scanning strategies such as the inward spiral and S-pattern, the transverse melt pool angle changes depending on the overlapping of the tracks and these strategies show different melt pool orientations in the transverse cross-section. The change in the orientation of the melt pool towards different sides is shown by negative and positive angle values in the figure. In general, if the melt pool keeps its symmetric hemispherical shape in the transverse cross-section, the maximum heat flow direction with respect to the horizontal line is about 90°. As the melt pool becomes inclined towards one side because of the overlapping beads and loses its asymmetric geometry, the maximum heat flow angle with respect to the horizontal line starts to change from 90° to 70°. The transverse melt pool angle mostly depends on the overlapping ratio of the overlapping beads and the scanning strategy. The predicted results for the maximum heat flow direction are in harmony with the microstructural observations in Figure 5-20. For example, the angle of columnar grain growth in the last track of the unidirectional and bidirectional is measured as about 50-90° (average 70°) in the different locations of the track. The predicted maximum heat flow direction value is also 70° which is

the same as the average measured angle of columnar grain growth. It should be noted that the prediction of the maximum heat flow direction and the columnar grain growth will help in the understanding of the solidification textures and it can also serve as a basis to customize the solidification textures.
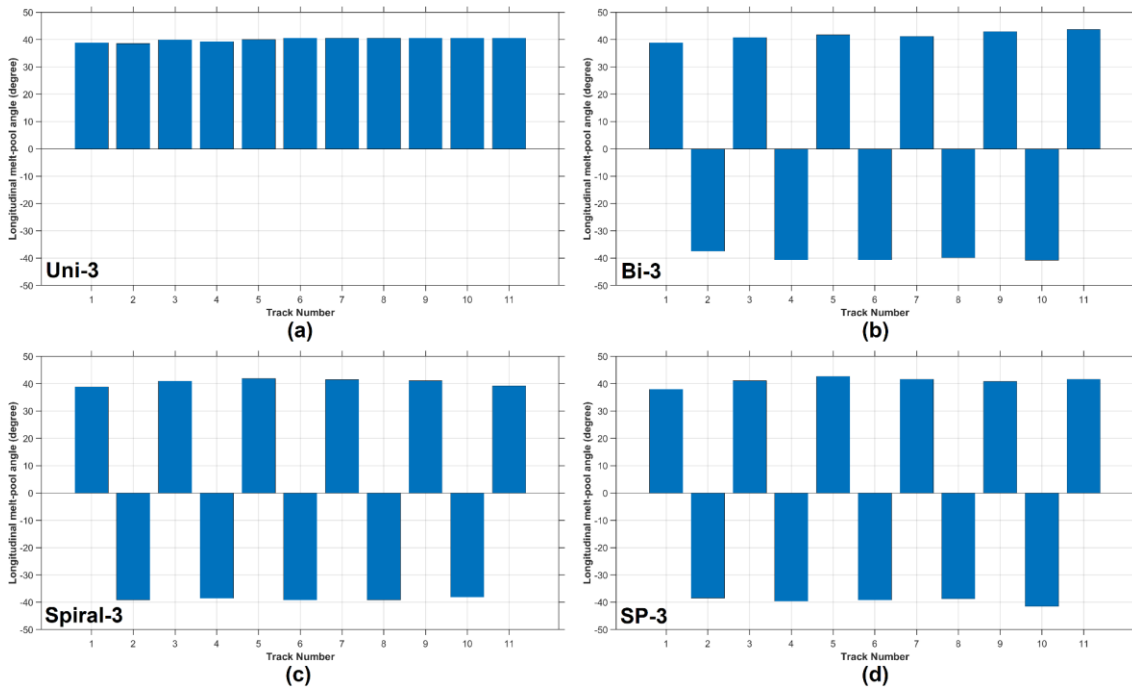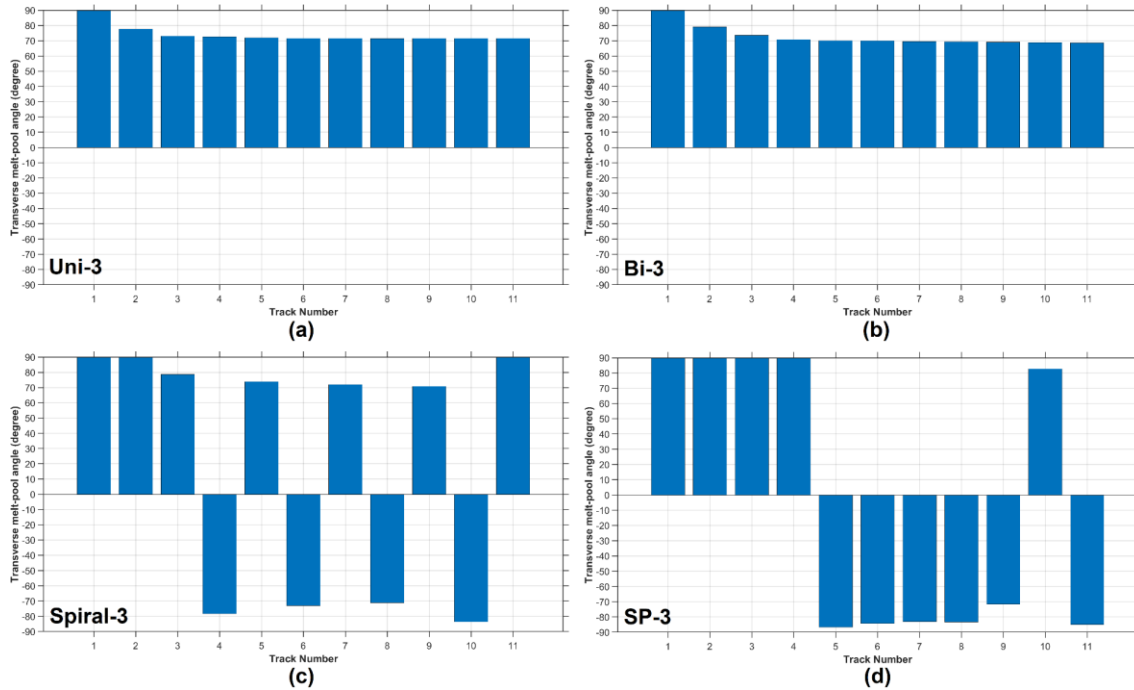

Figure 5-23. Predicted maximum heat flow directions based on the geometrical inclination of the melt pools in the transverse cross-section under the same processing parameter set (P=600 W, F=6 g/min, v_i=5 mm/s and h_s=1 mm) and different scanning strategies; (a) unidirectional, (b) bidirectional, (c) inward spiral, and (d) S-pattern strategy.

5.4.4.4 Solidification Map

The solidification mode is of a critical role in the performance of the additively manufactured components. Sometimes, having a fully columnar microstructure can be favorable, although it causes anisotropic properties. Sometimes, having a fully equiaxed microstructure is favorable since it provides isotropic properties. The investigation of columnar to equiaxed transition (CET) behavior is important because it helps to tailor the microstructure to favorable properties. The solidification mode can be evaluated through the development of a solidification map. During the deposition of each track, the solidification starts at the bottom of the melt pool, where the G/R ratio is highest. There is a very low constitutional supercooling at the early stage of solidification near the original melt pool boundary, resulting in metastable planar structures. The planar growth becomes unstable afterward, and columnar

94

growth happens where the G/R ratio is still high but lower than that of the planar zone. The decrease in the G/R ratio increases constitutional supercooling, inducing the columnar growth [47]. The direction of heat transfer is perpendicular to the solidification front, which leads to the epitaxial growth of columnar grains. Since the feedstock powder is being continuously fed into the melt pool, the major energy of the heat source is consumed for the melting of the material, resulting in a decrease in G/R ratio. Moreover, the powder particles impinging into the liquid may act as heterogeneous nucleation sites. As a result, the constitutional supercooling increases, and the epitaxial growth of columnar grains is interrupted. This promotes the nucleation of equiaxed grains, indicating the columnar to equiaxed transition (CET), and finally, fully equiaxed growth happens.

To develop a solidification map, the density of nucleation sites (N_0) must be estimated. Gäumann et al. [45] proposed a method of rough approximation in which N_0 can be determined by the correlation between the experimentally measured volume fractions of equiaxed grains ($\emptyset$) and the theory-calculated values in Equation 5-10 as a function of the mean $G^{n'}/R$ ratios for the different depositions. In this work, we assumed the same values for the constants of $n' = 3.4$ and $a' = 1.25 \times 10^3$ ($K^{3.4}mm^{-1}s$) as the work by Gäumann et al. [45]. The $\emptyset$ value can be experimentally measured by the EBSD technique. The measured $\emptyset$ from EBSD analysis are plotted as a function of the calculated mean $G^{3.4}/R$ ratios from the temperature model in Figure 5-24. The solid black line is the theory-predicted values of $\emptyset$ according to Equation 5-10 and the colorful points are the measured values of $\emptyset$ as a function of the mean $G^{3.4}/R$ ratios for different tracks under different processing conditions. A correlation between the experimental measurements and theoretically predicted values can be obtained when $N_0 = 4 \times 10^6$ (mm^{-3}). It should be noted that this method only provides an approximation for the density of nucleation sites and it should not be taken as the real density of nucleation sites for the material.
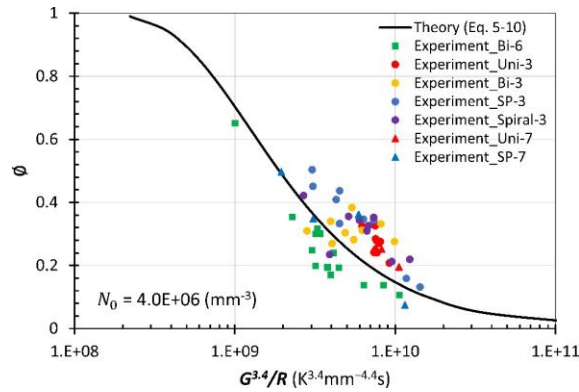
Figure 5-24. Correlation between the experimental measurements and the theory-predicted values as a function of mean $G^{3.4}/R$ ratios.

As proposed by Hunt [115], fully equiaxed/columnar behavior would occur when $\emptyset$ has critical values. Fully columnar grains are formed when $\emptyset < 0.0066$, while fully equiaxed grains are formed when $\emptyset > 0.66$. By setting these lower and higher critical values in Equation 5-10, the criteria of columnar to equiaxed transition (CET) in the form of a solidification map can be established. The solidification maps (thermal gradients vs. solidification rates) of different scanning strategies under different processing parameter sets are plotted in Figure 5-25. The blue and red solid lines represent the upper and lower criteria distinguishing the fully columnar and fully equiaxed regions, respectively. The tracks with higher mean G/R ratio than the blue line form fully columnar grains while the tracks with lower mean G/R ratio than the red line form fully equiaxed grains. The region between the blue and red lines is the mixed columnar-equiaxed region where the tracks encompass both columnar and equiaxed grains. In this region, the grains are in transition from the columnar to the equiaxed structure. The closer to the blue line, the more columnar grains form. The closer to the red line, the more equiaxed grains form. Comparing the solidification maps of different scanning strategies, all the multi-tracks under two scanning strategies of unidirectional and inward spiral fall into the mixed columnar-equiaxed region. However, some of the tracks in the bidirectional and S-pattern strategies fall outside the mixed region in the fully equiaxed region.
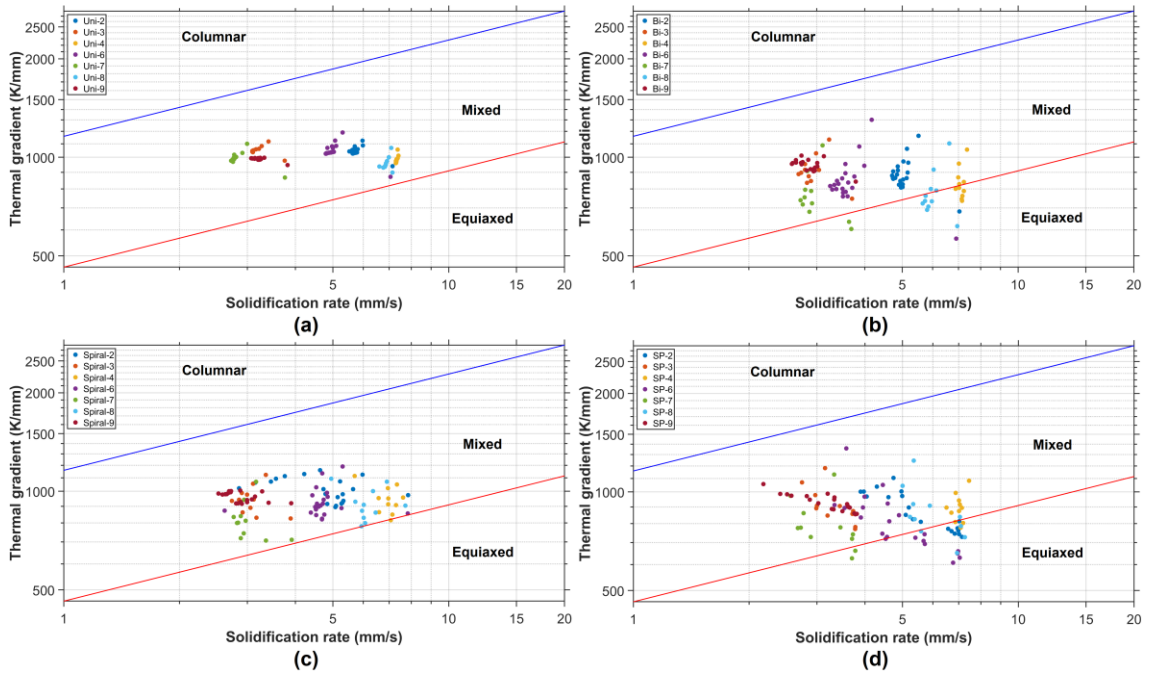
Figure 5-25. Solidification maps under different processing parameter sets and different scanning strategies; (a) unidirectional, (b) bidirectional, (c) inward spiral, and (d) S-pattern strategy. The points of the same color represent different tracks of one multi-track.

Having a close look at one of those tracks, which is predicted to fall into the fully equiaxed region, shows that the prediction of the solidification map is correct. Figure 5-26 represents the EBSD image of track 18 in sample SP-6 as an example of a fully equiaxed structure. The volume fraction of equiaxed grains in this track was measured to be more than 60%.
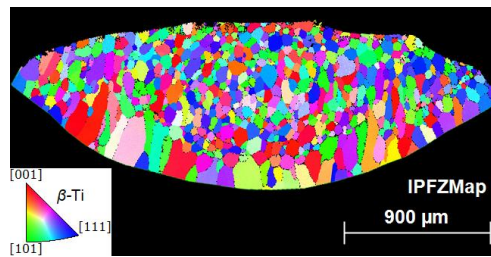
Figure 5-26. EBSD image showing the grain structure of track 18 (SP-6 sample) under the given processing parameter set (P=800 W, F=6 g/min, v_i=10 mm/s and h_s=0.5 mm) and S-pattern scanning strategy.

97

5.4.4.5 Dendritic Size

Based on the predicted solidification parameters, the PDAS can be predicted using Equation 5-12 and Equation 5-13, as summarized in Figure 5-27. The average PDAS was also experimentally measured from the OM images of the tracks. The triangular points show the predicted average PDAS according to Hunt's model [116], while the circular points show the predicted average PDAS according to Kurz and Fisher's model [117] for different tracks of the multi-tracks under different processing parameter sets and scanning strategies. The square points show the experimental measurements of average PDAS. According to the two classic models, the PDAS and cooling rate ($G^{-0.5}R^{-0.25}$ ratio) have a linear relationship. The PDAS generally increases by decreasing in the cooling rate or increasing in the mean $G^{-0.5}R^{-0.25}$ ratio. The Kurz and Fisher's model predicts larger average PDAS compared to the Hunt's model. The difference between these two models is that the Hunt's model was developed based on the geometry of dendrite tip while the Kurz and Fisher's model was developed based on the entire geometry of dendrite, including the tip and trunk. In this work, these two models act as upper and lower levels for the PDAS predictions. All the experimental measurements fall in between these two models' predictions and they have the same trend as the models. However, the experimental measurements are closer to the predictions of Hunt's model. The differences between the experimental results and theoretical predictions may be because both models assume a simple geometry for their initial conditions, while random perturbations may change initial conditions in the solidification [120]. Comparing these predictions for different scanning strategies under different processing parameter sets reveal that the unidirectional strategy leads to a finer dendritic substructure. The PDAS predictions for the rest of the scanning strategies are about the same range and the processing parameters are the main factor in defining the dendritic substructure size.

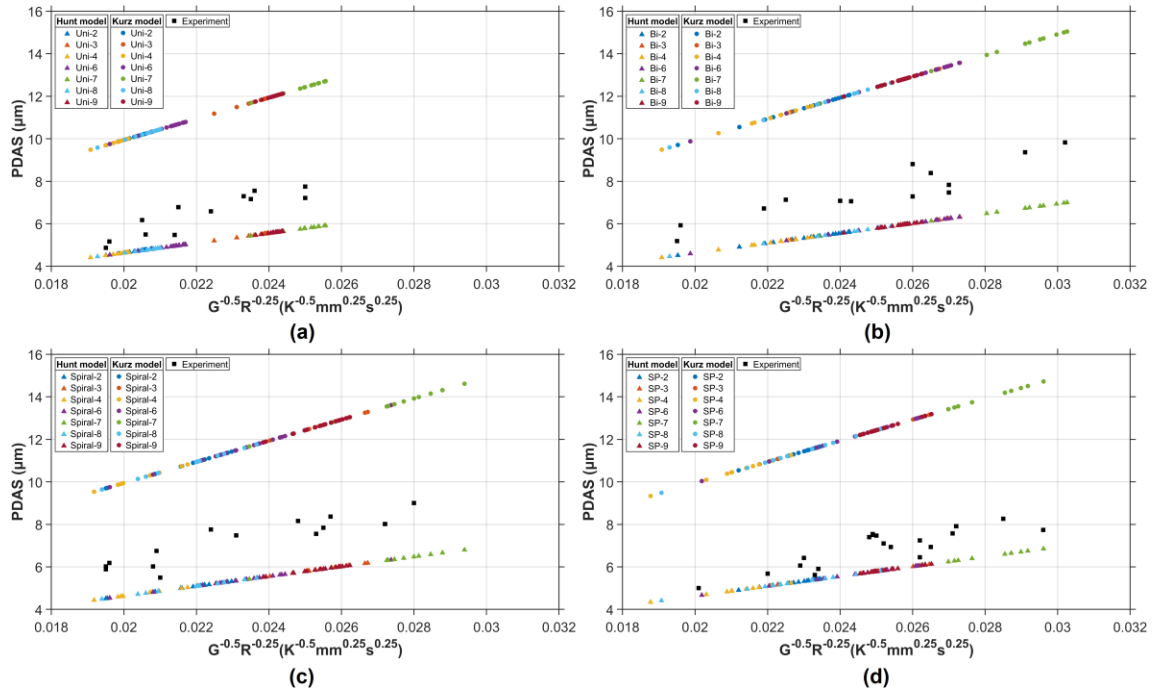**Figure 5-27. Predicted average PDAS based on two theories and experimental average measurements for the multi-tracks under different processing parameter sets and different scanning strategies; (a) unidirectional, (b) bidirectional, (c) inward spiral, and (d) S-pattern strategy. The points of the same color represent different tracks of one multi-track.**

5.4.4.6 Grain Size

One important factor to quantify the microstructure is the grain size. The measured average grain size of multi-tracks under different processing parameter sets and scanning strategies (Uni-2, Uni-3, Uni-6, Uni-7, Bi-2, Bi-3, Bi-6, Bi-7, Spiral-2, Spiral-3, Spiral-6, Spiral-7, SP-2, SP-3, SP-6, SP-7) is correlated to the calculated mean solidification cooling rate based on the classical theory by Boswell and Chadwick [118] (Equation 5-14). The material-dependent parameters of A and m in the equation are determined by the linear least-squares method. The correlation can be obtained when $A = 28801$ and $m = -0.638$. The fitted solution for the measured grain size of the multi-tracks are shown in Figure 5-28. The effect of mean solidification cooling rate, as the result of variations in processing parameter sets and scanning strategies, on the average grain size is significant. The average grain size ranged from 110 to 230 μm. The average grain size decreases with increasing the mean solidification cooling rate. The relationship provides a practical approach to establish the effect of solidification conditions on the

grain size and it can be used to correlate solidification conditions to tensile properties through the Hall–Petch relation [123].
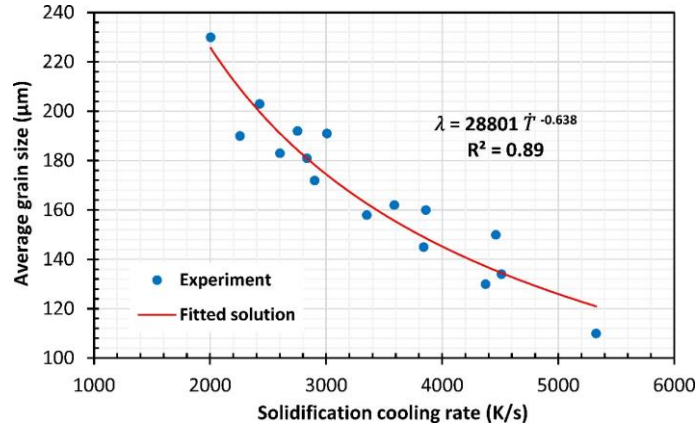

Figure 5-28. Correlation between the measured grain size and calculated mean solidification cooling rate.

5.5 Summary

In this study, a comprehensive physics-based model was developed and used to predict the temperature fields of multi-tracks under different scanning strategies. The thermal cycles and heating/cooling rates were compared for different scanning strategies. A new universal algorithm, based on parabolic functions, was derived to predict the geometrical profiles of the overlapping beads. Although the prediction of the geometrical profiles of the overlapping beads is complex, and the fact that they are highly dependent on scanning strategies and processing parameters, the developed universal algorithm to predict track geometries successfully predicted the profile of the overlapping beads under all four scanning strategies and nine processing parameter sets. The solidification parameters were then extracted from the temperature model to link the process to the solidification microstructure. The developed model was validated by depositing cuboidal geometries (10×10 mm) made of near-β titanium (Ti-5Al-5V-5Mo-3Cr) alloy at different laser powers, scanning speeds, and step-over distances under different scanning strategies of the bidirectional, unidirectional, inward spiral, and S-pattern. The solidification maps of Ti-5553 alloy manufactured by LDED-PF were developed to reveal the columnar to equiaxed transformation mechanism and validated using EBSD observations. The developed correlations among the temperature model and solidification characteristics provide an effective tool for process optimization and microstructural engineering through process-microstructure linkages.

100

Chapter 6: Adaptive Process Optimization using Physics-based Modeling of LDED-PF

6.1 Introduction

Thermal-based complexities and overlapping tracks happening during LDED-PF complicate the control of deposition rate and dimensions. On the other hand, the change in deposition rate and varied deposition heights changes the standoff distance and may risk the constancy of the nozzle standoff distance and process stability. In this chapter, an adaptive prediction protocol based on the physics-based modeling of the LDED-PF is developed for improved dimensional accuracy and flatness of the deposited layers. The standoff distance is kept constant during the build-up process the process stability is maintained.

6.2 Modeling Methodology

The adaptive modeling algorithm works on the basis of Equation 5-1, Equation 5-2, Equation 5-3, and Equation 5-5 for the simulation of temperature contribution and geometrical profile of overlapping tracks. This method takes a track-wise approach in which the model individually considers the temperature contribution and geometry of each track at a specific time. All model calculation is performed in a transverse cross-section at the time instant that the laser heat-source is at mid-length of the tracks. The method is adopted for direction-parallel scanning strategies such as bidirectional and unidirectional. The overall workflow used to implement the algorithm of adaptive physics-based modeling is described in Figure 6-1. The algorithm starts with initial conditions that can be different for each track. Let i denotes the track index. For the first track ($i = 1$), the initial conditions include the temperate of the build-plate (room temperature T_0) and the starting laser power (P_1). For the rest of tracks ($i > 1$), the initial conditions include the temperature contribution of previous tracks (T_{i-1}) and the predicted laser power of current track (P_i^*). The next step takes the initial conditions into account to simulate the temperature field (T_i) and geometry (f_i) of track i through process modeling developed in the previous chapter. The geometry of the current track is fed into the geometry-finder algorithm to find the desired geometry of the next track (f_{i+1}^*) based on the mathematical profile modeling developed in the previous chapter. Depending on the deposition scenario, the geometry-finder algorithm searches for the best-fit geometry close to the desired one. After finding the best-fit geometry, the laser power required to form that geometry is found using the power-finder algorithm. The melt pool/deposit

geometry can be estimated based on the liquid-solid isotherm defined by the transient temperature field (Equation 5-1). The power-finder algorithm converts the geometry to the laser power through reverse calculation. The desired coordinate of liquid-solid isotherm is predicted in the previous step by the geometry-finder algorithm. The temperature of the liquid-solid isotherm is also known (melting temperature of the material). Knowing the position, and temperature of the desired liquid-solid isotherm, the analytical solution to the transient temperature field (Equation 5-1) suffices to calculate the laser power of the next track (P_{i+1}^*). The next step simulates the temperature field (T_{i+1}) and geometry (f_{i+1}) of track $i+1$ through process modeling. The predicted laser power and its resultant temperature contribution are stored as the initial conditions of the next track and the workflow is repeated for all the tracks. It should be mentioned that the scanning strategy, step-over, and other processing parameters such as scanning speed and powder feed rate stay constant throughout the algorithm for adaptive physics-based modeling.
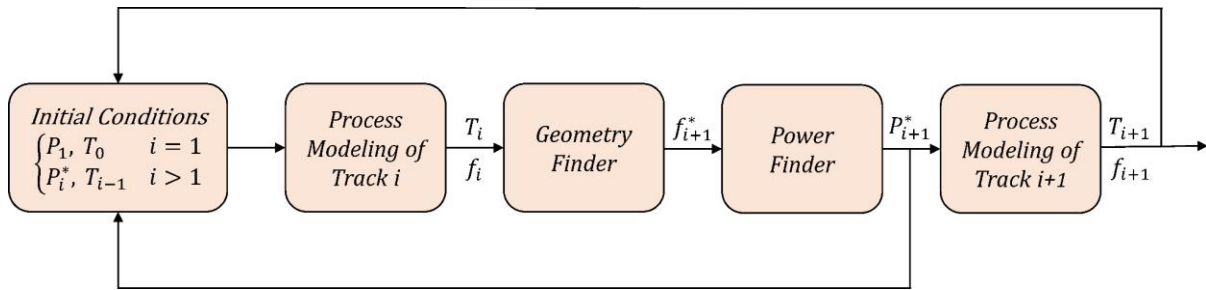

Figure 6-1. Flowchart of the adaptive physics-based modeling, showing the steps in the algorithm.

6.3 Experimental Procedures

Experiments were carried out using an LDED-PF system (IC106, DM3D Technology) in an atmosphere-controlled chamber with an oxygen level below 10 ppm. The system is equipped with an ABB robotic, a disk laser (TruDisk 2000, TRUMPF), and a dual powder feeder to feed powder through a coaxial nozzle. The nozzle standoff distance was set to 10 mm. The laser beam spot size was 1.4 mm at the standoff distance. The powder carrier gas (Argon) flow rate was set to 4 L/min. The powder hopper cover gas (Argon) flow rate was set to 8 L/min. The Nozzle gas flow rate was set to 6 L/min Argon and 4 L/min Helium. The nozzle shaping gas (Argon) flow rate was set to 6 L/min. In order to avoid the change in the chemical composition of the depositions as a result of mixing with the substrate, the feedstock powder and substrate of the same Ti-5Al-5V-5Mo-3Cr (Ti-5553) alloy were used. The

feedstock powder was spherical plasma-atomized Ti-5553 powder (AP&C, GE Additive) with particle size ranged from 45 to 106 μm and plates of the same alloy were printed with powder bed fusion technique (EOS M290) as substrate material. To test the adaptive model, multi-track LDED-PF of square-geometry tool-paths (10×10 mm) were performed under three scenarios. In the first scenario, the first track is deposited using the starting processing parameters and then the laser power of the rest of the tracks is modulated according to the adaptive model prediction to keep the height constant within a layer. In the second scenario, the laser power of the rest of the tracks is modulated according to the adaptive model prediction to keep the width constant within a layer. In the third scenario, the laser power of the rest of the tracks is modulated according to the adaptive model prediction to keep the width constant within four layers. A code is assigned to each sample that shows the scenario and processing parameters (Table 6-1). Three samples are coded as MT-ACH, MT-ACW, and ML-ACW for the multi-track adaptive model for constant height, the multi-track adaptive model for constant width, and the multi-layer adaptive model for constant width, respectively.

Table 6-1. Starting processing parameters of adaptive LDED-PF

Laser power (W)	Scanning speed (mm/s)	Powder feed rate (g/min)	Step-over (mm)
600	10	6	0.5

After the LDED-PF of the samples were finished, the profile of samples was examined by 3D imaging in optical microscopy (OM) (VHX-7000, KEYENCE). The model programming was performed in Matlab® R2019a using a DELL® computer with Intel® Core™ i7-7700 CPU @ 3.60 GHz RAM 16.0 GB. The thermophysical properties of Ti-5553 alloy are assumed to be temperature-independent. The average value of the thermophysical properties in the range from room temperature to melting temperature was used for model calculation. The thermophysical properties of the material are presented in Table 6-2.

Table 6-2. Thermophysical properties of Ti-5553 alloy

Properties	Value	Ref.
Melting Temperature [K]	1923	[108]
Density [g/cm^3]	4.65 (@298 K)-4.2 (@1923 K)	[108]
Thermal conductivity [W/m·K]	5 (@298 K)-29 (@1923 K)	[108]

Specific heat [J/(g·K)]	0.51 (@298 K)-0.8 (@1923 K)	[108]
Laser absorptivity	0.5	[108]
Coefficient of enhanced thermal diffusivity	1.4	[108]
Effective radius of the heat source [mm]	1	[108]

6.4 Results and Discussion

6.4.1 Adaptive Model for Constant Height

The sensitivity analysis in the previous chapter showed that laser power is the most influential factor in the prediction of the deposition width. In this study, we use a protocol of adaptive power prediction for controlling the temperature and geometry of the depositions. The scanning strategy of bidirectional is used as the most common strategy in LDED-PF. The laser power is predicted and modulated while the rest of the processing parameters are kept constant. The laser power defines the melt pool size. At given processing parameters, the change in the laser power changes the catchment efficiency and deposition geometry. Starting from the initial conditions, the algorithm successfully predicts the laser power to keep the height at a constant value of the first track. Figure 6-2 shows the results of adaptive modeling in the case of the MT-ACH sample. The laser power varies sharply in the few first tracks and converges to a value as the side-by-side deposition continues. The algorithm tries to keep the height of all tracks equal to the height of the first track. The reason for the variation in the laser power in different tracks is that the width of the tracks changes to provide the target height. Figure 6-2(c) and Figure 6-2(d) show the predicted width and height of the tracks as the result of the changing laser power. The height shows a small change while the width varies to minimize the height change. The solid black line in Figure 6-2(a) is the geometrical profile of tracks in the transverse cross-section from experimental measurement and the dashed blue lines are the simulated results. The predicted profile is in close agreement with the measured profile. Figure 6-2(e) shows the 3D imaging and analysis in the case of the MT-ACH sample. Comparing the results, the performance of the adaptive modeling is evident. The flatness of the deposition is noticeably improved. However, the uniformity of the deposition is more or less unstable. The model is forced to minimize the height change by changing the width, which caused sudden variations in the laser power. Having constant height is beneficial since it improves the flatness ratio and minimizes the change in the nozzle standoff distance during the deposition. However, the

sudden variations in the laser power might cause abrupt changes in the physics of the process, especially fluid dynamics. This adverse effect can lead to increased surface roughness and non-uniformity.
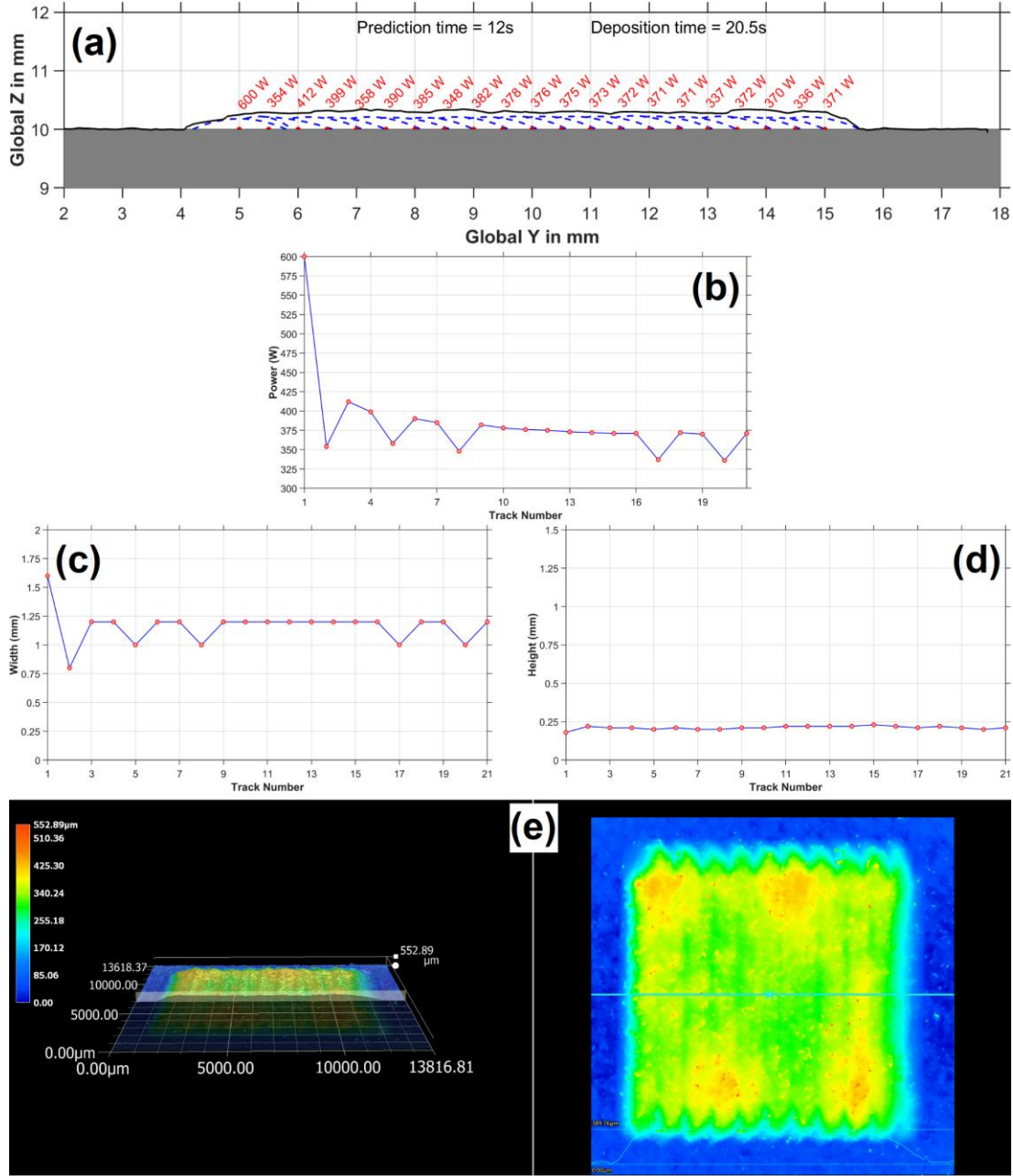

Figure 6-2. Adaptive modeling of constant height in the case of MT-ACH sample; (a) predicted geometrical profile of transverse cross-section, (b) predicted laser power, (c) predicted width, and (d) predicted height of different tracks. (e) 3D imaging and analysis used for experimental measurement.

6.4.2 Adaptive Model for Constant Width

In this section, another case of adaptive modeling is investigated. In the previous case, the algorithm was implemented to achieve a constant height for all the tracks within a layer. In this case, adaptive modeling is used to keep the width at a constant value of the first track. Starting from the initial conditions, the algorithm can predict the laser power to achieve a constant width for all the tracks. Figure 6-3 shows the results of adaptive modeling in the case of the MT-ACW sample. The laser power varies smoothly in the few first tracks and converges to a value as the deposition continues. Figure 6-3(c) and Figure 6-3(d) show the predicted width and height of the tracks as the result of the changing laser power. Although the algorithm could keep the width of all tracks equal to the width of the first track, the height of the first tracks increased until it reaches a peak value. The increased height happens because of the mass conservation in overlapping tracks. In other words, the model neutralizes the increased temperature and increased deposition rate as the result of heat accumulation. However, the effect of overlapping tracks still exists and increases the final height until it reaches a peak level. The performance of the adaptive modeling protocol is examined and validated. The solid black line in Figure 6-3(a) is the geometrical profile of tracks in the transverse cross-section from experimental measurement and the dashed blue lines are the simulated results. The predicted profile is in close agreement with the measured profile. Figure 6-3(e) shows the 3D imaging and analysis in the case of the MT-ACW sample. The flatness of the deposition is noticeably improved and the deposited layer is more or less uniform.
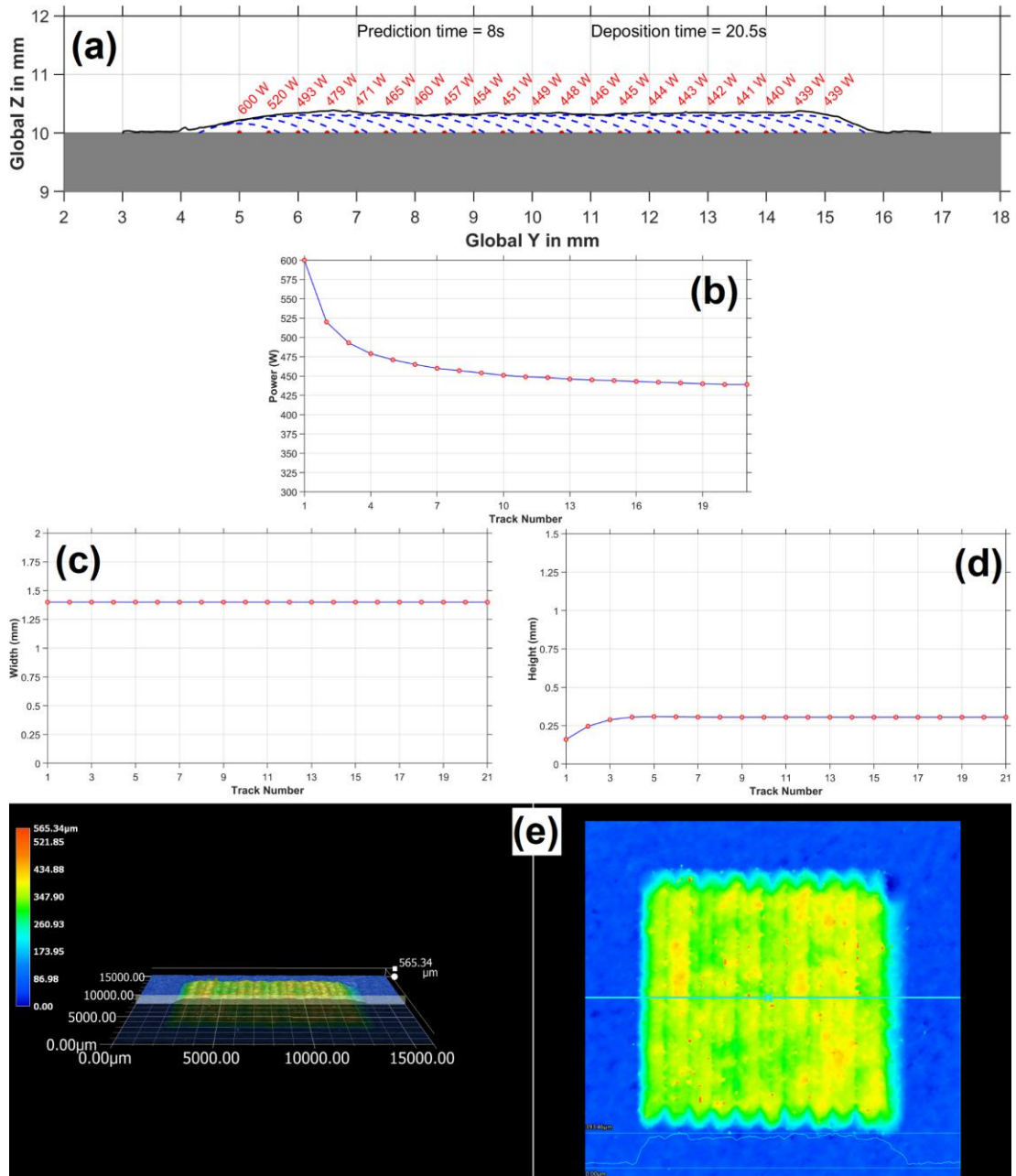
Figure 6-3. Adaptive modeling of constant width in the case of MT-ACW sample; (a) predicted geometrical profile of transverse cross-section, (b) predicted laser power, (c) predicted width, and (d) predicted height of different tracks. (e) 3D imaging and analysis used for experimental measurement.

6.4.3 Adaptive Model for Multi-layer Deposition

As the last case, the capability of the adaptive modeling in the multi-layer deposition is assessed. If we assume that the final part in the AM process is manufactured by depositing subsequent layers, then flattening each layer using adaptive modeling is beneficial to improve the final dimensional accuracy. Layers with non-uniform height might jeopardize the build-up process since the nozzle standoff distance changes in different layers and over/under deposition makes the process unstable. Using adaptive modeling, the power is predicted to control the overheating and flatten the layers. Once a layer is deposited, the nozzle moves equal to the height of that layer to apply the next layer. The layer-by-layer build-up process can continue, the nozzle standoff distance remains constant, and process stability is maintained. Starting from the initial conditions, the algorithm can predict the laser power to achieve a constant width for all the tracks in the multi-layer deposition. Figure 6-4 shows the results of adaptive modeling in the case of the ML-ACW sample. Figure 6-4(c) and Figure 6-4(d) show the predicted width and height of the tracks as the result of the changing laser power. The algorithm could keep the width of all tracks equal to the width of the first track. The layer height increases in each layer while the track height is more or less uniform within each layer. Figure 6-4(b) shows the predicted laser power. In the first layer, the laser power decreases smoothly. After the first layer, the change in the laser power becomes less and less. There is a small fluctuation in the laser power of different layers. The deposition of the first layer happens at high laser powers and there is overheating in the first layer. The second layer is applied right after the first layer and it has to deal with the overheating from the first layer. Therefore, the laser power should be decreased to overcome the overheating and maintain the temperature consistency and constant width. In the third layer, there is a small increase in the laser power. The overheating effect of the first layer is already neutralized in the second layer and heat from the first layer is dissipated. Now, the heat generated in the second layer has a major effect on the third layer. Since the second layer happened at low laser powers, the generated heat is low compared to the first layer. Thus, the third layer needs a little more energy input to maintain the temperature and the width. This small fluctuation of laser power continues to happen in layers until it converges. The performance of the adaptive modeling protocol for multi-layer deposition is validated. Figure 6-3(e) shows the 3D imaging and analysis in the case of the ML-ACW sample. The validation test proves the capability of adaptive modeling protocol to control the thermal complexities and geometry of the depositions.
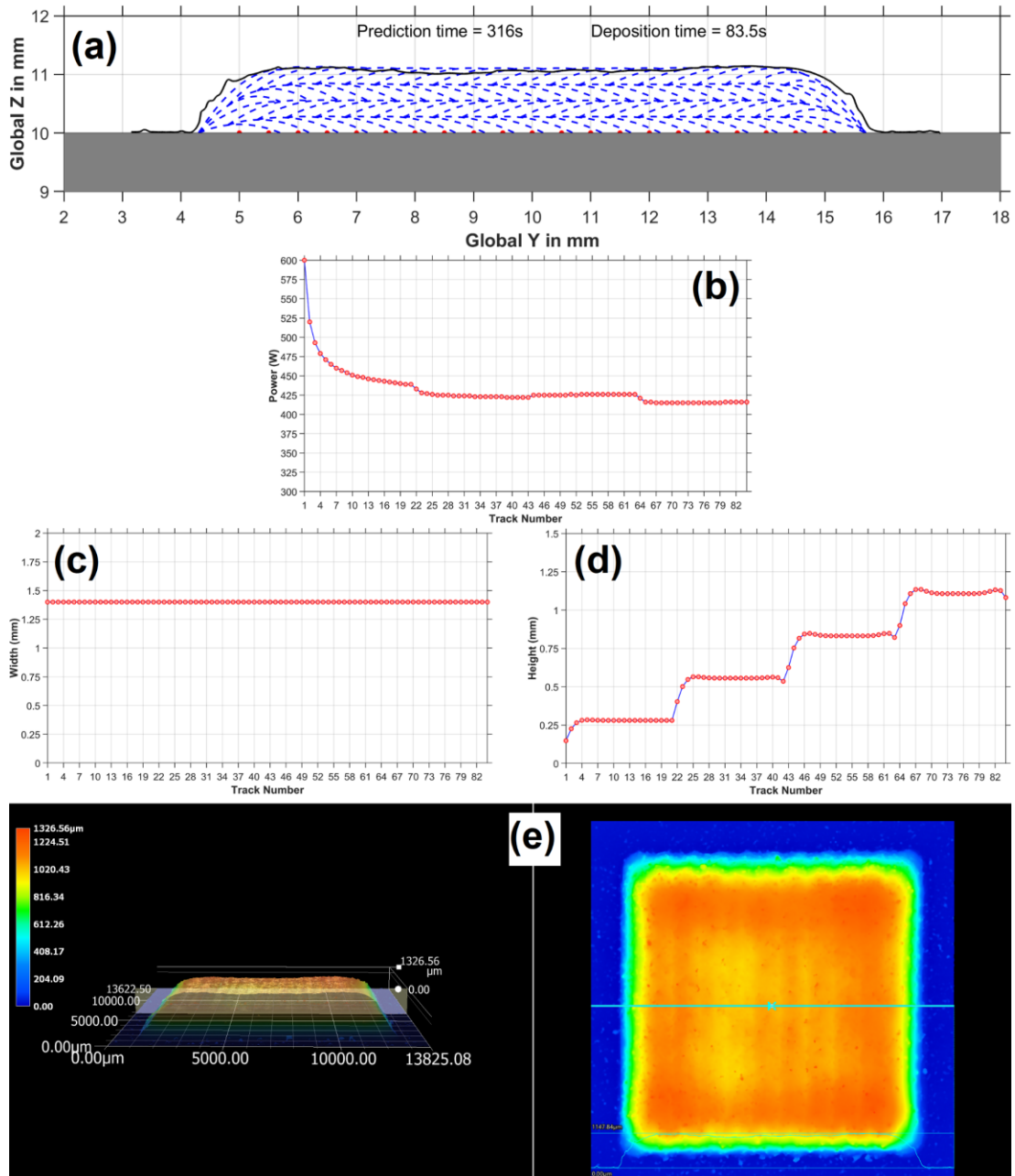
Figure 6-4. Adaptive modeling of constant width in the case of ML-ACW sample; (a) predicted geometrical profile of transverse cross-section, (b) predicted laser power, (c) predicted width, and (d) predicted height of different tracks. (e) 3D imaging and analysis used for experimental measurement.

109

6.5 Summary

In this chapter, an adaptive physics-based protocol is developed to control the overheating and dimensions of the depositions through the predicted laser powers. Mathematical models of temperature and geometry predictions are implemented in a unique algorithm to achieve the desired dimensions of different cases. The laser power prediction of adaptive modeling for constant height improved the flatness of the layer significantly. Nevertheless, overcompensation was sometimes observed that rendered the surface roughness worse. Adaptive modeling for constant width offers a smoother change in laser power while the track height might show a small increase in few first tracks. The adaptive modeling is also able to predict the laser power in the multi-layer deposition for better thermal and dimensional control. The success of this modeling approach is demonstrated through the discovery of an adaptive prediction protocol to improve layer height uniformity. The adaptive prediction of laser power is discovered to neutralize the adverse effect of heat accumulation and overheating. Moreover, the likelihood of achieving the desired dimensional accuracy is enhanced.

Chapter 7: Conclusions and Future Work

The main objective of this research was to develop time-efficient, and reasonably accurate process models for LDED-PF to save the time, money, and material required for experimental optimization/control. The model was expected to include the major physics of the process, be time-efficient, and effectively improve the process stability. With the benefits of high prediction accuracy and time efficiency, the developed model can be effectively used for purposes such as predicting and controlling the deposition dimensions and microstructure in LDED-PF. Another goal was to explore and understand the correlations between the process and final characteristics of Ti-5553 depositions. To this end, a comprehensive analytical model was built and validated. This chapter summarizes the overall conclusions and findings of the thesis and possible future works are proposed accordingly.

7.1 Thesis Overall Conclusions

As the first step in LDED-PF, a mathematical model was developed for parameter selection and process mapping of single-track deposition. As for the second step in the modeling, two major sources of energy, i.e. the laser beam and heated powder flux, were analytically described and coupled. The heated powder flux was described as a circular (2D) heat source. The laser-beam heat source was described by three different models known as a point (1D) heat source, circular (2D) heat source, and semi-spherical (3D) heat source. The performance of these three heat source models for the simulation of transient temperature fields was assessed and compared. To address the practical relevance and intricacy of the cyclic thermal behavior in LDED-PF, the model was fully implemented for multi-track deposition of different scanning strategies namely bidirectional, unidirectional, inward spiral, and S-pattern. The comprehensive process model was used to extract the solidification characteristics from the temperature model in order to link the process to the solidification microstructure. Lastly, the comprehensive process model was used as an adaptive modeling protocol for thermal and dimensional control. A unique algorithm was developed to adaptively predict the required laser power such that each track arrives at the desired dimensions. The following conclusions were drawn.

- The results showed the accuracy of prediction for the model, which works based on the Rosenthal solution to the heat conduction, depends on the processing parameters. In some cases, the model was predictive with 5-20 % accuracy error whereas the prediction was less than 50% accurate in some cases.

- Additional physical phenomena were added to the model for the process mapping. The problematic processing parameters, which led to either the vaporization or lack of fusion and consequently less accurate model prediction, were identified and the developed process map was designed to avoid them.

- The circular (2D) and semi-spherical (3D) laser-beam heat source models led to the more accurate temperature distribution. The maximum temperature was predicted to be about 3500-4000 K, which is acceptable for the titanium material with a boiling point of around 3500 K. The point heat source model predicted maximum temperatures of 6500-7000 K and unrealistic thermal gradients within the melt pool.

- For the melt pool length/width and deposit height, all the predicted results, based on the three laser-beam heat source models, fall within the experimental variation range. For the range of processing parameters used in the validation tests, the prediction error for the width, length, and height was 7, 4, and 4%, respectively. However, for the melt pool penetration in the substrate (dilution), only the predicted result from the 2D heat source model was within the experimental range, and both the 1D and 3D heat source models were out of the range with 35% error.

- According to the sensitivity analysis, the laser power was identified as the most influential parameter in the prediction of the melt pool width. A ±50% variation in the laser power changed the prediction of the melt pool width by more than 60 %.

- The universal mathematical system successfully predicted the geometrical profile of the overlapping beads under all four scanning strategies and nine processing parameter sets. For the given processing parameter sets, the prediction accuracy error for the total width and average height was less than 10 %.

- The process model for the geometry prediction showed high efficiency in terms of computational time. The model programming was performed in Matlab® R2019a using a DELL® computer with Intel® Core™ i7-7700 CPU @ 3.60 GHz RAM 16.0 GB. For the range of processing parameter sets, the computational time was recorded as 5-133 sec with the y increment of 0.05 mm, and the integration time interval of 0.01 sec.

- The solidification maps of Ti-5553 alloy manufactured by LDED-PF were developed to reveal the columnar to equiaxed transformation mechanism and validated using EBSD observations. It was

predicted and observed that the bidirectional and S-pattern strategies were able to encourage the formation of fully equiaxed structures under specific conditions while the unidirectional and inward spiral strategies were less likely to form fully equiaxed structures.

- The dendritic substructure size was predicted using two main theoretical models and compared with the experimental measurements. The unidirectional strategy produced the finest substructures. The experimental results were in harmony with theory-predicted results. The two main theoretical models acted as upper and lower limits for the dendritic substructure size. The prediction accuracy error, based on Hunt's model, was about 10-20 % while it was 25-40 % for the predictions based on Kurz and Fisher's model.

- The size of β grains was correlated to the solidification cooling rate. The semi-empirical relation developed for the size prediction of β grains as $\lambda \, (\mu m) = 28801 \, \dot{T}^{-0.638}$.

- The adaptive modeling was used to predict the laser power in different scenarios. The success of this modeling approach was demonstrated for improved uniformity and consistency of the deposited layers.

7.2 Future Work

The model developed in this study is applicable to all LDED-PF technologies and can be easily adapted for any material. However, to improve the developed model and its performance in predicting the final characteristics of the deposition, a few suggestions are provided as future work to advance this research.
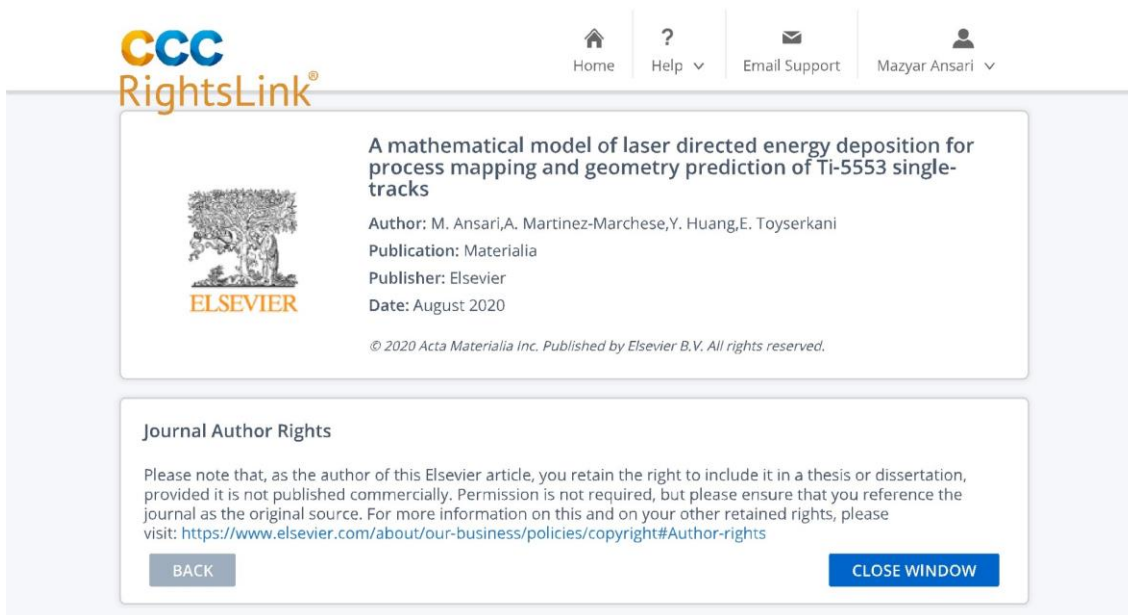
- Some assumptions such as temperature-independent thermophysical properties of materials, and ignorance of convection and radiation heat losses are the major sources of error in the analytical process modeling of LDED-PF. Although fully analytical solutions for the mentioned problems without the need for discretization methods and boundary conditions might be difficult or impossible, there should be some ways for the mathematical representation of them to consider their effects on the temperature field.

- In analytical solutions to the governing diffusion equation of heat conduction, the material/media on which the heat source moves is assumed semi-infinite. This assumption may not be satisfied in practice depending on the geometry of the part. Some adiabatic boundary conditions need to be

113

analytically introduced at the surface of the part to compensate for the change in heat conduction condition especially in the case of parts with thin sections and more complex structures.

- Although the developed process model in this thesis is extended to multi-track/multi-layer deposition of different scanning strategies, it is limited to orthogonal scanning strategies. The extension of this work to arbitrary scanning strategies of round and irregular geometries can unleash the full potential of the model in the enhancement of LDED-PF.

- Although the developed model was experimentally validated for Ti-5553 alloy and the DM3D machine, the implementation of the model on other machines of the same technology and different materials can be done for further model verification and universality.

- The model can be integrated into CAD/CAM software for simulation and optimization of the path before moving on to real deposition.

- The developed model can be used for sample fabrication of mechanical testing. The microstructural change and phase transformation can be better understood through a simulation-informed process. The temperature model developed in this work can act as the main engine of a mechanistic model for process-structure-property correlations.

- The adaptive modeling protocol could be potentially used for the development of model-based feedback control systems. The computation time can be accelerated by the use of Rosenthal's solution for the quasi-steady-state temperature field and a more advanced programming language such that the model fulfills the response requirement of the controller.

Letter of Copyright Permission

Permissions for the reuse of published chapters and figures:

Working distance passive stability in laser directed energy deposition additive manufacturing

Author:
James C. Haley,Baolong Zheng,Umberto Scipioni Bertoli,Alexander D. Dupuy,Julie M. Schoenung,Enrique J. Lavernia

Publication: Materials & Design

Publisher: Elsevier

Date: 5 January 2019

© 2018 Elsevier Ltd.

Creative Commons Attribution-NonCommercial-No Derivatives License (CC BY NC ND)

BACK   CLOSE WINDOW

Rapid prediction of real-time thermal characteristics, solidification parameters and microstructure in laser directed energy deposition (powder-fed additive manufacturing)

Author:
Yuze Huang,Mohammad Ansari,Hamed Asgari,Mohammad Hossein Farshidianfar,Dyuti Sarker,Mir Behrad Khamesee,Ehsan Toyserkani

Publication: Journal of Materials Processing Technology

Publisher: Elsevier

Date: December 2019

© 2019 Elsevier B.V. All rights reserved.

Journal Author Rights

BACK   CLOSE WINDOW

On the role of the powder stream on the heat and fluid flow conditions during Directed Energy Deposition of maraging steel —Multiphysics modeling and experimental validation

Author:
Mohamad Bayat,Venkata K. Nadimpalli,Francesco G. Biondani,Sina Jafarzadeh,Jesper Thorborg,Niels S. Tiedje,Giuliano Bissacco,David B. Pedersen,Jesper H. Hattel

Publication: Additive Manufacturing

Publisher: Elsevier

Date: July 2021

Order Completed

Your confirmation email will contain your order number for future reference.

License Number	5125101272759	🖨 Printable Details
License date	Aug 09, 2021	

Multiscale and multiphysics explorations of the transient deposition processes and additive characteristics during laser 3D printing

Author: H.L. Wei,F.Q. Liu,L. Wei,T.T. Liu,W.H. Liao

Publication: Journal of Material Science & Technology

Publisher: Elsevier

Date: 30 June 2021

Order Completed

Your confirmation email will contain your order number for future reference.

License Number	5125101373664	🖨 Printable Details
License date	Aug 09, 2021	

A digital twin for rapid qualification of 3D printed metallic components

Author: T. Mukherjee, T. DebRoy
Publication: Applied Materials Today
Publisher: Elsevier
Date: March 2019

Published by Elsevier Ltd.

Order Completed

Thank you for your order.

This Agreement between Dr. Mazyar Ansari ("You") and Elsevier ("Elsevier") consists of your license details and the terms and conditions provided by Elsevier and Copyright Clearance Center.

Your confirmation email will contain your order number for future reference.

License Number	5125110444397	🖶 Printable Details
License date	Aug 09, 2021	

References

[1]   T. DebRoy, H.L. Wei, J.S. Zuback, T. Mukherjee, J.W. Elmer, J.O. Milewski, A.M. Beese, A. Wilson-Heid, A. De, W. Zhang, Additive manufacturing of metallic components – Process, structure and properties, Prog. Mater. Sci. 92 (2018) 112–224. doi:10.1016/j.pmatsci.2017.10.001.

[2]   ASTM F2792-12a, Standard Terminology for Additive Manufacturing Technologies, (2012). doi:10.1520/F2792-12A.

[3]   W.J. Sames, F.A. List, S. Pannala, R.R. Dehoff, S.S. Babu, The metallurgy and processing science of metal additive manufacturing, Int. Mater. Rev. 61 (2016) 315–360. doi:10.1080/09506608.2015.1116649.

[4]   M. Alimardani, E. Toyserkani, J.P. Huissoon, C.P. Paul, On the delamination and crack formation in a thin wall fabricated using laser solid freeform fabrication process: An experimental–numerical investigation, Opt. Lasers Eng. 47 (2009) 1160–1168. doi:10.1016/J.OPTLASENG.2009.06.010.

[5]   K. Vartanian, L. Brewer, K. Manley, T. Cobbs, Powder bed fusion vs. directed energy deposition benchmark study: mid-size part with simple geometry, Optomec Corp. (2018). https://www.optomec.com/wp-content/uploads/2018/06/PBF-vs-DED-STUDY_Final_PDF.pdf.

[6]   M. Ansari, E. Jabari, E. Toyserkani, Opportunities and challenges in additive manufacturing of functionally graded metallic materials via powder-fed laser directed energy deposition: A review, J. Mater. Process. Technol. 294 (2021) 117117. doi:10.1016/j.jmatprotec.2021.117117.

[7]   LENS Core & Emerging Applications, (n.d.). https://www.optomec.com/3d-printed-metals/lens-emerging-applications/.

[8]   E. Toyserkani, A. Khajepour, S. Corbin, Laser Cladding, CRC Press, Boca Raton, 2004.

[9]   L. Costa, I. Felde, T. Réti, Z. Kálazi, R. Colaço, R. Vilar, B. Verő, A simplified semi-empirical method to select the processing parameters for laser clad coatings, Mater. Sci. Forum. 414–415 (2003) 385–394. doi:10.4028/www.scientific.net/MSF.414-415.385.

[10]   S. Liu, R. Kovacevic, Statistical analysis and optimization of processing parameters in high-

power direct diode laser cladding, Int. J. Adv. Manuf. Technol. 74 (2014) 867–878. doi:10.1007/s00170-014-6041-y.

[11]   M. Barekat, R. Shoja Razavi, A. Ghasemi, Nd:YAG laser cladding of Co–Cr–Mo alloy on γ-TiAl substrate, Opt. Laser Technol. 80 (2016) 145–152. doi:10.1016/j.optlastec.2016.01.003.

[12]   M. Ansari, R. Shoja Razavi, M. Barekat, An empirical-statistical model for coaxial laser cladding of NiCrAlY powder on Inconel 738 superalloy, Opt. Laser Technol. 86 (2016) 136–144. doi:10.1016/j.optlastec.2016.06.014.

[13]   B. Bax, R. Rajput, R. Kellet, M. Reisacher, Systematic evaluation of process parameter maps for laser cladding and direct energy deposition, Addit. Manuf. 21 (2018) 487–494. doi:10.1016/j.addma.2018.04.002.

[14]   M. Ansari, A. Mohamadizadeh, Y. Huang, V. Paserin, E. Toyserkani, Laser directed energy deposition of water-atomized iron powder: Process optimization and microstructure of single-tracks, Opt. Laser Technol. 112 (2019) 485–493. doi:10.1016/j.optlastec.2018.11.054.

[15]   A. Dass, A. Moridi, State of the Art in Directed Energy Deposition: From Additive Manufacturing to Materials Design, Coatings. 9 (2019) 418. doi:10.3390/coatings9070418.

[16]   A.J. Pinkerton, Advances in the modeling of laser direct metal deposition, J. Laser Appl. 27 (2015) S15001. doi:10.2351/1.4815992.

[17]   Z. Zhang, Y. Huang, A. Rani Kasinathan, S. Imani Shahabad, U. Ali, Y. Mahmoodkhani, E. Toyserkani, 3-Dimensional heat transfer modeling for laser powder-bed fusion additive manufacturing with volumetric heat sources based on varied thermal conductivity and absorptivity, Opt. Laser Technol. 109 (2019) 297–312. doi:10.1016/j.optlastec.2018.08.012.

[18]   Y. Huang, M.B. Khamesee, E. Toyserkani, A comprehensive analytical model for laser powder-fed additive manufacturing, Addit. Manuf. 12 (2016) 90–99. doi:10.1016/j.addma.2016.07.001.

[19]   Y. Huang, M.B. Khamesee, E. Toyserkani, A new physics-based model for laser directed energy deposition (powder-fed additive manufacturing): From single-track to multi-track and multi-layer, Opt. Laser Technol. 109 (2019) 584–599. doi:10.1016/j.optlastec.2018.08.015.

[20]   J. Goldak, A. Chakravarti, M. Bibby, A new finite element model for welding heat sources, Metall. Trans. B. 15 (1984) 299–305. doi:10.1007/BF02667333.

[21] S. Zhu, W. Chen, L. Ding, X. Zhan, Q. Chen, A mathematical model of laser cladding repair, Int. J. Adv. Manuf. Technol. 103 (2019) 3265–3278. doi:10.1007/s00170-019-03588-3.

[22] I. Tabernero, A. Lamikiz, E. Ukar, L.N. López de Lacalle, C. Angulo, G. Urbikain, Numerical simulation and experimental validation of powder flux distribution in coaxial laser cladding, J. Mater. Process. Technol. 210 (2010) 2125–2134. doi:10.1016/j.jmatprotec.2010.07.036.

[23] O.B. Kovalev, D.V. Bedenko, A.V. Zaitsev, Development and application of laser cladding modeling technique: From coaxial powder feeding to surface deposition and bead formation, Appl. Math. Model. 57 (2018) 339–359. doi:10.1016/j.apm.2017.09.043.

[24] S.Y. Wen, Y.C. Shin, J.Y. Murthy, P.E. Sojka, Modeling of coaxial powder flow for the laser direct deposition process, Int. J. Heat Mass Transf. 52 (2009) 5867–5877. doi:10.1016/j.ijheatmasstransfer.2009.07.018.

[25] E. Toyserkani, A. Khajepour, S. Corbin, Three-dimensional finite element modeling of laser cladding by powder injection: Effects of powder feedrate and travel speed on the process, J. Laser Appl. 15 (2003) 153–160. doi:10.2351/1.1585087.

[26] E. Toyserkani, A. Khajepour, S. Corbin, 3-D finite element modeling of laser cladding by powder injection: effects of laser pulse shaping on the process, Opt. Lasers Eng. 41 (2004) 849–867. doi:10.1016/S0143-8166(03)00063-0.

[27] J.T. Hofman, D.F. de Lange, B. Pathiraj, J. Meijer, FEM modeling and experimental verification for dilution control in laser cladding, J. Mater. Process. Technol. 211 (2011) 187–196. doi:10.1016/j.jmatprotec.2010.09.007.

[28] S. Safdar, A.J. Pinkerton, L. Li, M.A. Sheikh, P.J. Withers, An anisotropic enhanced thermal conductivity approach for modelling laser melt pools for Ni-base super alloys, Appl. Math. Model. 37 (2013) 1187–1195. doi:10.1016/j.apm.2012.03.028.

[29] X. He, J. Mazumder, Transport phenomena during direct metal deposition, J. Appl. Phys. 101 (2007) 053113. doi:10.1063/1.2710780.

[30] H. Qi, J. Mazumder, H. Ki, Numerical simulation of heat transfer and fluid flow in coaxial laser cladding process for direct metal deposition, J. Appl. Phys. 100 (2006) 024903. doi:10.1063/1.2209807.

[31] J.C. Haley, B. Zheng, U.S. Bertoli, A.D. Dupuy, J.M. Schoenung, E.J. Lavernia, Working distance passive stability in laser directed energy deposition additive manufacturing, Mater. Des. 161 (2019) 86–94. doi:10.1016/j.matdes.2018.11.021.

[32] M. Bayat, V.K. Nadimpalli, F.G. Biondani, S. Jafarzadeh, J. Thorborg, N.S. Tiedje, G. Bissacco, D.B. Pedersen, J.H. Hattel, On the role of the powder stream on the heat and fluid flow conditions during Directed Energy Deposition of maraging steel—Multiphysics modeling and experimental validation, Addit. Manuf. 43 (2021) 102021. doi:10.1016/j.addma.2021.102021.

[33] H.L. Wei, F.Q. Liu, L. Wei, T.T. Liu, W.H. Liao, Multiscale and multiphysics explorations of the transient deposition processes and additive characteristics during laser 3D printing, J. Mater. Sci. Technol. 77 (2021) 196–208. doi:10.1016/j.jmst.2020.11.032.

[34] M. Picasso, C.F. Marsden, J.D. Wagniere, A. Frenk, M. Rappaz, A simple but realistic model for laser cladding, Metall. Mater. Trans. B. 25 (1994) 281–291. doi:10.1007/BF02665211.

[35] A. Frenk, M. Vandyoussefi, J.-D. Wagnière, W. Kurz, A. Zryd, Analysis of the laser-cladding process for stellite on steel, Metall. Mater. Trans. B. 28 (1997) 501–508. doi:10.1007/s11663-997-0117-0.

[36] C. Lalas, K. Tsirbas, K. Salonitis, G. Chryssolouris, An analytical model of the laser clad geometry, Int. J. Adv. Manuf. Technol. 32 (2006) 34–41. doi:10.1007/s00170-005-0318-0.

[37] A.J. Pinkerton, R. Moat, K. Shah, L. Li, M. Preuss, P.J. Withers, A verified model of laser direct metal deposition using an analytical enthalpy balance method, Int. Congr. Appl. Lasers Electro-Optics 2007. 1806 (2007). doi:10.2351/1.5061038.

[38] J.M. Jouvard, D.F. Grevey, F. Lemoine, A.B. Vannes, Continuous wave Nd:YAG laser cladding modeling: A physical study of track creation during low power processing, J. Laser Appl. 9 (1997) 43–50. doi:10.2351/1.4745444.

[39] U. de Oliveira, V. Ocelík, J.T.M. De Hosson, Analysis of coaxial laser cladding processing conditions, Surf. Coatings Technol. 197 (2005) 127–136. doi:10.1016/j.surfcoat.2004.06.029.

[40] J. Li, Q. Wang, P. (Pan) Michaleris, E.W. Reutzel, A.R. Nassar, An Extended Lumped-Parameter Model of Melt–Pool Geometry to Predict Part Height for Directed Energy Deposition, J. Manuf. Sci. Eng. 139 (2017) 1–14. doi:10.1115/1.4037235.

[41] J. Li, Q. Wang, P. (Pan) Michaleris, An Analytical Computation of Temperature Field Evolved in Directed Energy Deposition, J. Manuf. Sci. Eng. 140 (2018). doi:10.1115/1.4040621.

[42] Y. Chew, J.H.L. Pang, G. Bi, B. Song, Thermo-mechanical model for simulating laser cladding induced residual stresses with single and multiple clad beads, J. Mater. Process. Technol. 224 (2015) 89–101. doi:10.1016/j.jmatprotec.2015.04.031.

[43] H.L. Wei, T. Mukherjee, W. Zhang, J.S. Zuback, G.L. Knapp, A. De, T. DebRoy, Mechanistic models for additive manufacturing of metallic components, Prog. Mater. Sci. (2020) 100703. doi:10.1016/j.pmatsci.2020.100703.

[44] T. Mukherjee, T. DebRoy, A digital twin for rapid qualification of 3D printed metallic components, Appl. Mater. Today. 14 (2019) 59–65. doi:10.1016/j.apmt.2018.11.003.

[45] M. Gäumann, C. Bezençon, P. Canalis, W. Kurz, Single-crystal laser deposition of superalloys: processing–microstructure maps, Acta Mater. 49 (2001) 1051–1062. doi:10.1016/S1359-6454(00)00367-0.

[46] P.C. Collins, D.A. Brice, P. Samimi, I. Ghamarian, H.L. Fraser, Microstructural Control of Additively Manufactured Metallic Materials, Annu. Rev. Mater. Res. 46 (2016) 63–91. doi:10.1146/annurev-matsci-070115-031816.

[47] S. Kou, Welding Metallurgy, Second Edi, John Wiley & Sons, Inc., Hoboken, NJ, USA, 2002. doi:10.1002/0471434027.

[48] Z. Tang, W. Liu, Y. Wang, K.M. Saleheen, Z. Liu, S. Peng, Z. Zhang, H. Zhang, A review on in situ monitoring technology for directed energy deposition of metals, Int. J. Adv. Manuf. Technol. 108 (2020) 3437–3463. doi:10.1007/s00170-020-05569-3.

[49] H. Wang, W. Liu, Z. Tang, Y. Wang, X. Mei, K.M. Saleheen, Z. Wang, H. Zhang, Review on adaptive control of laser-directed energy deposition, Opt. Eng. 59 (2020) 1. doi:10.1117/1.OE.59.7.070901.

[50] M. Akbari, R. Kovacevic, An investigation on mechanical and microstructural properties of 316LSi parts fabricated by a robotized laser/wire direct metal deposition system, Addit. Manuf. 23 (2018) 487–497. doi:10.1016/J.ADDMA.2018.08.031.

[51] M.H. Farshidianfar, A. Khajepour, A.P. Gerlich, Effect of real-time cooling rate on

microstructure in Laser Additive Manufacturing, J. Mater. Process. Technol. 231 (2016) 468–478. doi:10.1016/j.jmatprotec.2016.01.017.

[52]   M.H. Farshidianfar, F. Khodabakhshi, A. Khajepour, A.P. Gerlich, Closed-loop control of microstructure and mechanical properties in additive manufacturing by directed energy deposition, Mater. Sci. Eng. A. 803 (2021) 140483. doi:10.1016/j.msea.2020.140483.

[53]   F. Lia, J.Z. Park, J.S. Keist, S. Joshi, R.P. Martukanitz, Thermal and microstructural analysis of laser-based directed energy deposition for Ti-6Al-4V and Inconel 625 deposits, Mater. Sci. Eng. A. 717 (2018) 1–10. doi:10.1016/j.msea.2018.01.060.

[54]   Y. Huang, M. Ansari, H. Asgari, M.H. Farshidianfar, D. Sarker, M.B. Khamesee, E. Toyserkani, Rapid prediction of real-time thermal characteristics, solidification parameters and microstructure in laser directed energy deposition (powder-fed additive manufacturing), J. Mater. Process. Technol. 274 (2019) 116286. doi:10.1016/j.jmatprotec.2019.116286.

[55]   J. Strickland, B. Nenchev, H. Dong, On Directional Dendritic Growth and Primary Spacing—A Review, Crystals. 10 (2020) 627. doi:10.3390/cryst10070627.

[56]   G.L. Knapp, T. Mukherjee, J.S. Zuback, H.L. Wei, T.A. Palmer, A. De, T. DebRoy, Building blocks for a digital twin of additive manufacturing, Acta Mater. 135 (2017) 390–399. doi:10.1016/j.actamat.2017.06.039.

[57]   Z. Sun, W. Guo, L. Li, Numerical modelling of heat transfer, mass transport and microstructure formation in a high deposition rate laser directed energy deposition process, Addit. Manuf. 33 (2020) 101175. doi:10.1016/j.addma.2020.101175.

[58]   N. Clément, A. Lenain, P.J. Jacques, Mechanical property optimization via microstructural control of new metastable beta titanium alloys, JOM. 59 (2007) 50–53. doi:10.1007/s11837-007-0010-y.

[59]   R.R. Boyer, Attributes, characteristics, and applications of titanium and its alloys, JOM. 62 (2010) 21–24. doi:10.1007/s11837-010-0071-1.

[60]   J.C. Colombo-Pulgarín, C.A. Biffi, M. Vedani, D. Celentano, A. Sánchez-Egea, A.D. Boccardo, J.P. Ponthot, Beta Titanium Alloys Processed By Laser Powder Bed Fusion: A Review, J. Mater. Eng. Perform. (2021). doi:10.1007/s11665-021-05800-6.

125

[61]   G. Tomchik, Overview of Titanium Applications on Advanced Commercial Transports, in: 17th AeroMat Conf., Seattle, Washington, 2006.

[62]   J. Fan, Microstructural study of the β → α phase transformation induced by thermo-mechanical treatments in metastable β Ti-5553 alloy, Université de Lorraine, 2016. doi:<NNT:2016LORR0144> <tel-01466759>.

[63]   R. Evans, Selection and testing of metalworking fluids, in: Metalwork. Fluids Cut. Grind., Elsevier, 2012: pp. 23–78. doi:10.1533/9780857095305.23.

[64]   L.C. Zhang, D. Klemm, J. Eckert, Y.L. Hao, T.B. Sercombe, Manufacture by selective laser melting and mechanical behavior of a biomedical Ti–24Nb–4Zr–8Sn alloy, Scr. Mater. 65 (2011) 21–24. doi:10.1016/j.scriptamat.2011.03.024.

[65]   J. Hernandez, S.J. Li, E. Martinez, L.E. Murr, X.M. Pan, K.N. Amato, X.Y. Cheng, F. Yang, C.A. Terrazas, S.M. Gaytan, Y.L. Hao, R. Yang, F. Medina, R.B. Wicker, Microstructures and Hardness Properties for β-Phase Ti–24Nb–4Zr–7.9Sn Alloy Fabricated by Electron Beam Melting, J. Mater. Sci. Technol. 29 (2013) 1011–1017. doi:10.1016/j.jmst.2013.08.023.

[66]   Y. Liu, S. Li, W. Hou, S. Wang, Y. Hao, R. Yang, T.B. Sercombe, L.-C. Zhang, Electron Beam Melted Beta-type Ti–24Nb–4Zr–8Sn Porous Structures With High Strength-to-Modulus Ratio, J. Mater. Sci. Technol. 32 (2016) 505–508. doi:10.1016/j.jmst.2016.03.020.

[67]   Y.J. Liu, S.J. Li, H.L. Wang, W.T. Hou, Y.L. Hao, R. Yang, T.B. Sercombe, L.C. Zhang, Microstructure, defects and mechanical behavior of beta-type titanium porous structures manufactured by electron beam melting and selective laser melting, Acta Mater. 113 (2016) 56–67. doi:10.1016/j.actamat.2016.04.029.

[68]   Y.J. Liu, H.L. Wang, S.J. Li, S.G. Wang, W.J. Wang, W.T. Hou, Y.L. Hao, R. Yang, L.C. Zhang, Compressive and fatigue behavior of beta-type titanium porous structures fabricated by electron beam melting, Acta Mater. 126 (2017) 58–66. doi:10.1016/j.actamat.2016.12.052.

[69]   Y.J. Liu, X.P. Li, L.C. Zhang, T.B. Sercombe, Processing and properties of topologically optimised biomedical Ti–24Nb–4Zr–8Sn scaffolds manufactured by selective laser melting, Mater. Sci. Eng. A. 642 (2015) 268–278. doi:10.1016/j.msea.2015.06.088.

[70]   Q. Wang, C. Han, T. Choma, Q. Wei, C. Yan, B. Song, Y. Shi, Effect of Nb content on

microstructure, property and in vitro apatite-forming capability of Ti-Nb alloys fabricated via selective laser melting, Mater. Des. 126 (2017) 268–277. doi:10.1016/j.matdes.2017.04.026.

[71]   T. Ishimoto, K. Hagihara, K. Hisamoto, S.-H. Sun, T. Nakano, Crystallographic texture control of beta-type Ti–15Mo–5Zr–3Al alloy by selective laser melting for the development of novel implants with a biocompatible low Young's modulus, Scr. Mater. 132 (2017) 34–38. doi:10.1016/j.scriptamat.2016.12.038.

[72]   Y. Wang, S. Zhang, X. Tian, H. Wang, High-cycle fatigue crack initiation and propagation in laser melting deposited TC18 titanium alloy, Int. J. Miner. Metall. Mater. 20 (2013) 665–670. doi:10.1007/s12613-013-0781-9.

[73]   Z. LI, X. TIAN, H. TANG, H. WANG, Low cycle fatigue behavior of laser melting deposited TC18 titanium alloy, Trans. Nonferrous Met. Soc. China. 23 (2013) 2591–2597. doi:10.1016/S1003-6326(13)62772-7.

[74]   C.M. Liu, X.J. Tian, H.B. Tang, H.M. Wang, Microstructural characterization of laser melting deposited Ti–5Al-5Mo–5V–1Cr–1Fe near β titanium alloy, J. Alloys Compd. 572 (2013) 17–24. doi:10.1016/j.jallcom.2013.03.243.

[75]   H. Schwab, F. Palm, U. Kühn, J. Eckert, Microstructure and mechanical properties of the near-beta titanium alloy Ti-5553 processed by selective laser melting, Mater. Des. 105 (2016) 75–80. doi:10.1016/j.matdes.2016.04.103.

[76]   H. Schwab, M. Bönisch, L. Giebeler, T. Gustmann, J. Eckert, U. Kühn, Processing of Ti-5553 with improved mechanical properties via an in-situ heat treatment combining selective laser melting and substrate plate heating, Mater. Des. 130 (2017) 83–89. doi:10.1016/j.matdes.2017.05.010.

[77]   C. Zopp, S. Blümer, F. Schubert, A. Marquardt, A. Seidel, L. Kroll, C. Leyens, Processing and mechanical properties of a metastable titanium alloy (Ti-5Al-5V-5Mo-3Cr) by selective laser melting, in: 2nd Conf. Exhib. Light Mater., Bremen, Germany, 2017. https://lightmat2017.dgm.de/program/?tx_dgmprogram_fullprogram%5Bfile%5D=761&tx_dgmprogram_fullprogram%5Bsession%5D=2429&tx_dgmprogram_fullprogram%5Baction%5D=downloadFile&tx_dgmprogram_fullprogram%5Bcontroller%5D=Session&cHash=6e85f4ad8d8bf43d17b72b2d072.

[78] C. Zopp, S. Blümer, F. Schubert, L. Kroll, Processing of a metastable titanium alloy (Ti-5553) by selective laser melting, Ain Shams Eng. J. 8 (2017) 475–479. doi:10.1016/j.asej.2016.11.004.

[79] H.D. Carlton, K.D. Klein, J.W. Elmer, Evolution of microstructure and mechanical properties of selective laser melted Ti-5Al-5V-5Mo-3Cr after heat treatments, Sci. Technol. Weld. Join. 24 (2019) 465–473. doi:10.1080/13621718.2019.1594589.

[80] S. Bakhshivash, H. Asgari, P. Russo, C.F. Dibia, M. Ansari, A.P. Gerlich, E. Toyserkani, Printability and microstructural evolution of Ti-5553 alloy fabricated by modulated laser powder bed fusion, Int. J. Adv. Manuf. Technol. 103 (2019) 4399–4409. doi:10.1007/s00170-019-03847-3.

[81] C. Qiu, G.A. Ravi, M.M. Attallah, Microstructural control during direct laser deposition of a β-titanium alloy, Mater. Des. 81 (2015) 21–30. doi:10.1016/j.matdes.2015.05.031.

[82] A. Hatefi, Direct Laser Fabrication of Ti-5553, University of Birmingham, 2013. http://etheses.bham.ac.uk/4667/2/Hatefi13MRes.pdf.

[83] L. Xie, H. Guo, Y. Song, C. Liu, Z. Wang, L. Hua, L. Wang, L.-C. Zhang, Effects of electroshock treatment on microstructure evolution and texture distribution of near-β titanium alloy manufactured by directed energy deposition, Mater. Charact. 161 (2020) 110137. doi:10.1016/j.matchar.2020.110137.

[84] M. Kubiak, W. Piekarska, Z. Saternus, S. Stano, Numerical modelling of thermal and structural phenomena in Yb:YAG laser butt-welded steel elements, Arch. Metall. Mater. 60 (2015) 821–828. doi:10.1515/amm-2015-0213.

[85] N. Yang, Concentration model based on movement model of powder flow in coaxial laser cladding, Opt. Laser Technol. 41 (2009) 94–98. doi:10.1016/j.optlastec.2008.03.008.

[86] J. Lin, Concentration mode of the powder stream in coaxial laser cladding, Opt. Laser Technol. 31 (1999) 251–257. doi:10.1016/S0030-3992(99)00049-3.

[87] A.J. Pinkerton, L. Li, Modelling Powder Concentration Distribution From a Coaxial Deposition Nozzle for Laser-Based Rapid Tooling, J. Manuf. Sci. Eng. 126 (2004) 33. doi:10.1115/1.1643748.

[88]   C. Lampa, A.F.H. Kaplan, J. Powell, C. Magnusson, An analytical thermodynamic model of laser welding, J. Phys. D. Appl. Phys. 30 (1997) 1293–1299. doi:10.1088/0022-3727/30/9/004.

[89]   W. Zhang, C.-H. Kim, T. DebRoy, Heat and fluid flow in complex joints during gas metal arc welding—Part II: Application to fillet welding of mild steel, J. Appl. Phys. 95 (2004) 5220–5229. doi:10.1063/1.1699486.

[90]   T. Lienert, T. Siewert, S. Babu, V. Acoff, eds., ASM Handbook, Volume 6A: Welding Fundamentals and Processes, ASM International, Materials Park, Ohio, 2011.

[91]   W.M. Steen, J. Mazumder, Laser Material Processing, 4th Editio, Springer London, London, 2010. doi:10.1007/978-1-84996-062-5.

[92]   T. DebRoy, S.A. David, Physical processes in fusion welding, Rev. Mod. Phys. 67 (1995) 85–112. doi:10.1103/RevModPhys.67.85.

[93]   R. Rai, J.W. Elmer, T.A. Palmer, T. DebRoy, Heat transfer and fluid flow during keyhole mode laser welding of tantalum, Ti–6Al–4V, 304L stainless steel and vanadium, J. Phys. D. Appl. Phys. 40 (2007) 5753–5766. doi:10.1088/0022-3727/40/18/037.

[94]   D.B. Hann, J. Iammi, J. Folkes, A simple methodology for predicting laser-weld properties from material and laser parameters, J. Phys. D. Appl. Phys. 44 (2011) 445401. doi:10.1088/0022-3727/44/44/445401.

[95]   R. Fabbro, Scaling laws for the laser welding process in keyhole mode, J. Mater. Process. Technol. 264 (2019) 346–351. doi:10.1016/j.jmatprotec.2018.09.027.

[96]   W.E. King, H.D. Barth, V.M. Castillo, G.F. Gallegos, J.W. Gibbs, D.E. Hahn, C. Kamath, A.M. Rubenchik, Observation of keyhole-mode laser melting in laser powder-bed fusion additive manufacturing, J. Mater. Process. Technol. 214 (2014) 2915–2925. doi:10.1016/j.jmatprotec.2014.06.005.

[97]   A.M. Rubenchik, W.E. King, S.S. Wu, Scaling laws for the additive manufacturing, J. Mater. Process. Technol. 257 (2018) 234–243. doi:10.1016/j.jmatprotec.2018.02.034.

[98]   Z.Y. Wang, J.T. Liu, D.M. Hirak, D.C. Weckman, H.W. Kerr, Determining the Spot Size and Gaussian Distribution Coefficient of Pulsed Laser Beams Using KAPTON Films, J. Laser Appl. 5 (1993) 5–12. doi:10.2351/1.4745318.

[99] M. Ansari, A. Martinez-Marchese, Y. Huang, E. Toyserkani, A mathematical model of laser directed energy deposition for process mapping and geometry prediction of Ti-5553 single-tracks, Materialia. 12 (2020) 100710. doi:10.1016/j.mtla.2020.100710.

[100] H.S. Carslaw, J.C. Jaeger, Conduction of Heat in Solids, 2nd Editio, Oxford University Press, London, 1959.

[101] A.J. Pinkerton, L. Li, Modelling the geometry of a moving laser melt pool and deposition track via energy and mass balances, J. Phys. D. Appl. Phys. 37 (2004) 1885–1895. doi:10.1088/0022-3727/37/14/003.

[102] Z. Liu, H.-C. Zhang, S. Peng, H. Kim, D. Du, W. Cong, Analytical modeling and experimental validation of powder stream distribution during direct energy deposition, Addit. Manuf. 30 (2019) 100848. doi:10.1016/j.addma.2019.100848.

[103] V.A. Bykov, T. V. Kulikova, L.B. Vedmid', A.Y. Fishman, K.Y. Shunyaev, N.Y. Tarenkova, Thermophysical properties of Ti-5Al-5V-5Mo-3Cr-1Zr titanium alloy, Phys. Met. Metallogr. 115 (2014) 705–709. doi:10.1134/S0031918X14050020.

[104] J.J. Valencia, P.N. Quested, Thermophysical Properties, in: D.U. Furrer, S.L. Semiatin (Eds.), ASM Handb. Met. Process Simul., Vol. 22B, ASM International, 2010: pp. 18–32. doi:10.31399/asm.hb.v22b.a0005523.

[105] A. Vasinonta, J.L. Beuth, M. Griffith, Process Maps for Predicting Residual Stress and Melt Pool Size in the Laser-Based Fabrication of Thin-Walled Structures, J. Manuf. Sci. Eng. 129 (2007) 101–109. doi:10.1115/1.2335852.

[106] D. Ding, Z. Pan, D. Cuiuri, H. Li, A tool-path generation strategy for wire and arc additive manufacturing, Int. J. Adv. Manuf. Technol. 73 (2014) 173–183. doi:10.1007/s00170-014-5808-5.

[107] L. Sun, X. Ren, J. He, Z. Zhang, Numerical investigation of a novel pattern for reducing residual stress in metal additive manufacturing, J. Mater. Sci. Technol. 67 (2021) 11–22. doi:10.1016/j.jmst.2020.05.080.

[108] M. Ansari, M. Khamooshi, Y. Huang, E. Toyserkani, Analytical solutions for rapid prediction of transient temperature field in powder-fed laser directed energy deposition based on different

heat source models, Appl. Phys. A. 127 (2021) 445. doi:10.1007/s00339-021-04591-w.

[109] N.N. Rykalin, Calculation of Heat Processes in Welding, Moscow, Russia, 1960. https://repositories.lib.utexas.edu/handle/2152/14232.

[110] W. Perret, C. Schwenk, M. Rethmeier, Comparison of analytical and numerical welding temperature field calculation, Comput. Mater. Sci. 47 (2010) 1005–1015. doi:10.1016/j.commatsci.2009.11.032.

[111] V. Ocelík, O. Nenadl, A. Palavra, J.T.M. De Hosson, On the geometry of coating layers formed by overlap, Surf. Coatings Technol. 242 (2014) 54–61. doi:10.1016/j.surfcoat.2014.01.018.

[112] O. Nenadl, W. Kuipers, N. Koelewijn, V. Ocelík, J.T.M. De Hosson, A versatile model for the prediction of complex geometry in 3D direct laser deposition, Surf. Coatings Technol. 307 (2016) 292–300. doi:10.1016/j.surfcoat.2016.08.090.

[113] L.E. dos Santos Paes, H.S. Ferreira, M. Pereira, F.A. Xavier, W.L. Weingaertner, L.O. Vilarinho, Modeling layer geometry in Directed Energy Deposition with laser for additive manufacturing, Surf. Coatings Technol. 409 (2021) 126897. doi:10.1016/j.surfcoat.2021.126897.

[114] H.L. Wei, J. Mazumder, T. DebRoy, Evolution of solidification texture during additive manufacturing, Sci. Rep. 5 (2015) 16446. doi:10.1038/srep16446.

[115] J.D. Hunt, Steady state columnar and equiaxed growth of dendrites and eutectic, Mater. Sci. Eng. 65 (1984) 75–83. doi:10.1016/0025-5416(84)90201-5.

[116] J.D. Hunt, Solidification and Casting of Metals, The Metals Society, London, 1979.

[117] W. Kurz, D.J. Fisher, Dendrite growth at the limit of stability: tip radius and spacing, Acta Metall. 29 (1981) 11–20. doi:10.1016/0001-6160(81)90082-1.

[118] P.G. Boswell, G.A. Chadwick, The grain size of splat-quenched alloys, Scr. Metall. 11 (1977) 459–465. doi:10.1016/0036-9748(77)90157-0.

[119] V.B. Biscuola, M.A. Martorano, Mechanical Blocking Mechanism for the Columnar to Equiaxed Transition, Metall. Mater. Trans. A. 39 (2008) 2885–2895. doi:10.1007/s11661-008-9643-x.

[120] L. Wu, J. Zhang, Phase Field Simulation of Dendritic Solidification of Ti-6Al-4V During Additive Manufacturing Process, JOM. 70 (2018) 2392–2399. doi:10.1007/s11837-018-3057-z.

[121] A. Keshavarzkermani, E. Marzbanrad, R. Esmaeilizadeh, Y. Mahmoodkhani, U. Ali, P.D. Enrique, N.Y. Zhou, A. Bonakdar, E. Toyserkani, An investigation into the effect of process parameters on melt pool geometry, cell spacing, and grain refinement during laser powder bed fusion, Opt. Laser Technol. 116 (2019) 83–91. doi:10.1016/j.optlastec.2019.03.012.

[122] A. Keshavarzkermani, R. Esmaeilizadeh, P.D. Enrique, H. Asgari, N.Y. Zhou, A. Bonakdar, E. Toyserkani, Static recrystallization impact on grain structure and mechanical properties of heat-treated Hastelloy X produced via laser powder-bed fusion, Mater. Charact. 173 (2021) 110969. doi:10.1016/j.matchar.2021.110969.

[123] C.J. Todaro, M.A. Easton, D. Qiu, D. Zhang, M.J. Bermingham, E.W. Lui, M. Brandt, D.H. StJohn, M. Qian, Grain structure control during metal 3D printing by high-intensity ultrasound, Nat. Commun. 11 (2020) 142. doi:10.1038/s41467-019-13874-z.